# NOVEL DESIGNS AND PHOTOEMISSION PHYSICS TO ENHANCE BRIGHTNESS OF RF PHOTOINJECTORS

By

Benjamin Sims

A DISSERTATION

Submitted to
Michigan State University
in partial fulfillment of the requirements
for the degree of

Electrical and Computer Engineering —Doctor of Philosophy
Physics—Dual Major

2025

**ABSTRACT**

High-brightness injectors are key to improvements in UED, XFELs, and Laser Compton Back Scattering technologies as they increase their resolution, efficiency, and performance when used. Current advancements in cathode technologies and emittance compensation have provided substantial gains in brightness in recent years but additional approaches will be necessary to continue pushing to higher levels of brightness and resulting light source luminosity.

This dissertation discusses novel practical approaches and designs that can be implemented on various accelerators to improve their brightness. Chapter 2 focused on Space charge emittance and RF emittance management exampled using a canonical injector. Chapter 3 discusses implementing cathode retraction for in-situ intrinsic emittance measurement with the goal of decreasing emittance as well as ensuring desired cathode performance. Chapter 4 explores a novel multimode cavity design that focuses on bunch compression to increase the current of the bunch and thus the brightness.

To Alexandria Sims

**ACKNOWLEDGMENTS**

I would like to thank many people who helped me through my journey of completing my thesis at Michigan State University. Firstly, I would like to thank my advising professor, Prof. Sergey Baryshev for his continued support and guidance throughout this process. Prof. Baryshev has been an endless source of knowledge, and he has helped me grow as both a scientist and a professional. He has never let anyone slip a subpar answer past him and always knows when you need to do a better job grasping the subject matter, but he never makes you feel lesser for it. He inspires and challenges you to work harder and understand more to grow to meet any obstacle. He has always had my back throughout this process, and it is through his guidance that I feel I will be able to be successful wherever my professional studies take me.

I would also like to thank Dr. John Lewellen. I started working with Dr. Lewellen a couple of years into my Ph.D. program and his training and advice made much of this dissertation possible. Dr. Lewellen's ability to provide insightful, knowledgeable, and respectful answers to even my simplest questions has shown me the level of understanding I hope to one day achieve. John, your advice never goes unheeded and is always deeply appreciated.

Additionally, I would like to extend my appreciation to my committee at Michigan State University. My committee's feedback throughout this entire process aided me in putting together my best work. Their support and wealth of information gave me a strong foundation to continuously improve as a student and a professional.

I would also like to thank all of my lab mates who guided and encouraged me throughout this process, especially Dr. Mitchell Schneider, and Dr. Taha Posos. Dr. Mitchell Schneider offered guidance and support which helped immensely as I started as a graduate student. Dr. Taha Posos challenged me to better understand General Particle Tracer (GPT), a program we both used. Our discussions helped ensure accuracy and clarity in my results and for that, you have my respect and appreciation.

Not only was I blessed with professional support, but I was also fortunate to have family to support my endeavors as well. I would like to thank my beautiful wife, Alexandria Sims for her

endless support. She has been there for me at every step of this journey and her commitment and support has never wavered. Your smile has gotten me through some of my hardest days and inspired me to keep going. She has been an inspiration just as much as she has been a support system to me during my studies and I couldn't be more thankful for her.

I would also like to thank my parents, Jeff and Carrie Sims, for introducing me to the sciences at a young age and fostering a lifelong interest in my field of study. Their support throughout the years helped me get to where I am today, and I am so grateful for that. Additionally, I would like to thank my younger brother, David Sims, for his support. David not only supported me through my professional studies, but he also asked a lot of thoughtful questions which helped me learn to explain my thoughts and findings in a more accurate and concise manner. I would also like to extend my thanks to my wife's parents Frank Joo and Lauretta Scimone. When I first moved to Michigan to pursue my undergraduate studies and started dating their daughter, Frank and Lauretta welcomed me with open arms, great food, and endless support. They helped to make the transition to life in a new state much easier. Lastly, I would like to thank my cats. My late kitten Socks, and my cats Whiskey and Cora all were a joy and helped keep me positive throughout this process. Between their guest appearances during conference Zoom meetings and general goofiness, they always brought a smile to my face when I had long and tiring days. I cannot express how thankful I am for everyone's help during these years of study, I could not have done this without your help.

## TABLE OF CONTENTS

## LIST OF ABBREVIATIONS

**FEL** Free-electron laser

**XFEL** X-ray Free-electron laser

**UED** Ultra-Fast Electron Diffraction

**LCBS** Laser Compton Back Scattering

**RF** Radio-frequency

**SRF** Superconducting Radio-frequency

**SC** Space Charge

**MTE** Mean transverse energy

**RMS** Root mean square

**QE** Quantum Efficiency

**LEI** Low Emittance Injector

**LCLS** Linac Coherent Light Source

**LCLS-HE** Linac Coherent Light Source High Energy

**SLAC** Stanford Linear Accelerator Center

**MSU** Michigan State University

**FRIB** Facility for Rare Isotope Beams

**FRIB** Helmholtz-Zentrum Dresden-Rossendorf

**ACT** Argonne Cathode Teststand

**TM** Transverse Magnetic

**TE** Transverse Electric

**VNA** Virtual Network Analyzer

**6D** Six Dimensional

**5D** Five Dimensional

**4D** Four Dimensional

| | |
|---|---|
| **Q** | Quality |
| **GPT** | General Particle Tracer |
| **R&D** | Research and Development |
| **GaN** | Gallium Nitride |

# CHAPTER 1

# INTRODUCTION

This thesis focuses on achieving high brightness in electron beamlines by understanding and managing the emittances at play as well as implementing novel concepts related to cavity designs. High brightness has long been the goal of many-electron accelerators and with this goal, some solutions have been implemented to achieve 5D brightnesses in the 200 -1800 TA/m2 range [1]. To continue breaking records and providing high-brightness beams for applications like UED, FXELs, and Lase Compton Back Scattering, new solutions must be proposed, tested, and implemented to surpass 1800 TA/m2.

The Linac Coherent Light Source (LCLS) at SLAC National Accelerator Laboratory is one of the best examples of the improvements necessary to keep an XFEL relevant. The original LCLS accelerator was upgraded as the demand for high brightness beams grew in the community resulting in a 10,000x increase in brightness with the implementation of LCLS-II. Already another upgrade, LCLS-HE, is being designed and tested promising another 1,000x increase in brightness as the demand for ever increasingly bright beams grows. This desire for high-brightness beams within the accelerator community stems from the many benefits that they provide. High-brightness beams increase the resolution, efficiency, and performance of all experiments they are used in, broadening their usefulness to a larger number of users. Specifically for the case of the LCLS, increased brightness of the electron beam correlates to a tighter more intense x-ray bunch produced which increases the resolution on target as well as requiring less beam time to achieve results. Because of these benefits, the desire for brighter and brighter beams continues to grow. Current strategies to improve brightness mainly focus on cathode material and emittance compensation which have been able to keep up so far, but for the next generation of high-brightness accelerators novel designs and approaches, beyond what is common today, will be necessary.

More particularly, this work explores and identifies new promising approaches for achieving high brightness via emittance management techniques and multimode cavity implementation. Chapter 2 focuses on the interplay between space charge emittance and RF emittance. It was found that the operating parameters of the injector, laser spot size, laser pulse length, and accelerating gradient, can be used to identify the lowest emittance for a given bunch charge and mean transverse energy (MTE) from a cathode material. Chapter 3 discusses an in-situ approach for measuring the intrinsic emittance of a cathode using cathode retraction. The produced simulations illustrate the usefulness of cathode retraction as it was able to decrease the emittance of the bunch as well as manipulate the phase space of the bunch making it easier to measure. The in-situ nature of this measurement approach is also of some novelty as being able to characterize a cathode that has been in use can help to identify possible damage as well as ensure the cathode is still operating as desired over its lifetime. Chapter 4 focuses on the design and characterization of multi-mode cavities. Multimode cavities have been proposed numerous times over the years but have yet to be implemented in a variety of accelerator technologies. The design proposed focuses on creating a cavity that can bunch and accelerate, thereby increasing the current of a bunch and thus its brightness.

## 1.1 Photoemission Electron Injector

### 1.1.1 Photoemission

Photoemission is the result of the photoelectric effect which postulates that electrons can be emitted from materials once sufficient photon energy has been used, see Fig. 1.1. The minimum photon energy needed to excite the electrons and allow them to escape the surface is commonly referred to as the work function. This thesis will focus on the use of semiconductors as the source of electron beams as is the case with LCLS-II and LCLS-HE. Semiconductors, as an electron source, are used due to their work function being dependent on the material they were constructed from. This also for the work function to be manipulated to allow for operation at much lower photon energy than typical metal cathodes. Plus, the quantum efficiency of semiconductor cathodes is much higher than that of metal cathodes commonly attaining > 1

### 1.1.2 Injector Parameters

For photoemission electron injectors the laser parameters used on the cathode determine the final bunch shape. Pulse length refers to the length of the laser pulse experienced by the cathode and as a result the length of the bunch produced, as electrons will continue to be emitted while the

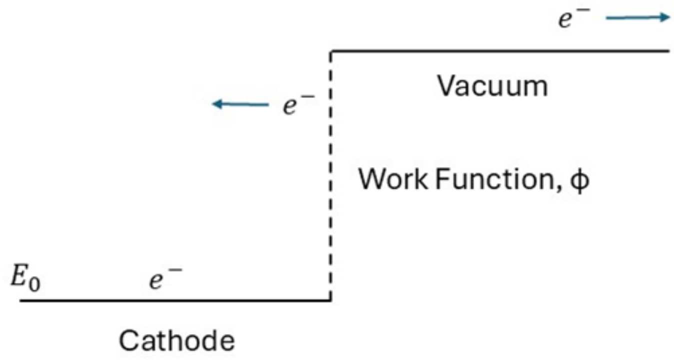


Figure 1.1 Simplified model of the photoelectric effect.

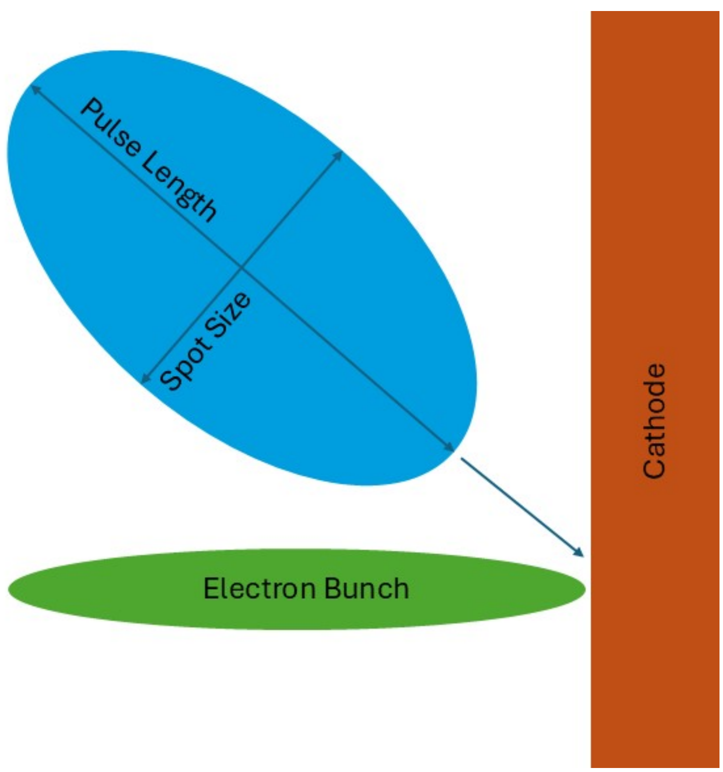


Figure 1.2 A simple model illustrating the transition from laser pulse parameters to an electron bunch.

cathode is exposed to the laser. Spot size refers to the diameter of the laser exposed to the cathode. This determines the area over which the electrons will be emitted. Figure 1.2 illustrates the relation of pulse length and spot size on a bunch. Large spot sizes allow for sourcing electrons for a larger area preventing a region of the cathode from being limited by how quickly it can replenish electrons. However large spot sizes also increase the intrinsic emittance as well as the energy spread. Quantum efficiency refers to the ratio of the resulting number of electrons emitted to the number of photons exposed to the cathode. This along with laser intensity which is the measure of the number of photos in the laser pulse directly affects the resulting charge of the produced bunch.

### 1.1.3 Emittance

Emittance is a measurement of the phase space area of a particle bunch. The phase space is the 6D distribution of the particles in x, y, or z and its accompanying momenta x', y', or z'. A 2D emittance measures the emittance in one direction, i.e. x and x', see Fig. 1.3. 4D emittance is commonly measured in both the x and y directions, but it will not be discussed further in this thesis as a general assumption that x and y are nearly identical when not using additional focusing elements such as solenoids or quadrupole magnets. The RMS emittance is commonly calculated as seen in Eq. 1.1 [2], which is the determinant of the emittance matrix of the bunch.

$$\varepsilon_x = \sqrt{\langle x^2 \rangle \langle x'^2 \rangle - \langle x^2 \cdot x'^2 \rangle} \tag{1.1}$$

The number of particles used is also an adaptation factor in emittance measurements. This thesis will only be using 100% emittance measurements as all emittance measurements were collected from simulated data which is generally uniform and lacks the discrepancies commonly seen with experimental data. It is quite common to see 90% or 95% emittance measurements when discussing experimental data where they are used to eliminate particles that deviate too strongly from the desired pathing throughout the machine.

### 1.1.4 Emittance Contributions

Three of the main contributors to emittance are space charge emittance, radio frequency emittance, and intrinsic emittance. Space charge emittance is due to the Coulombic interactions between

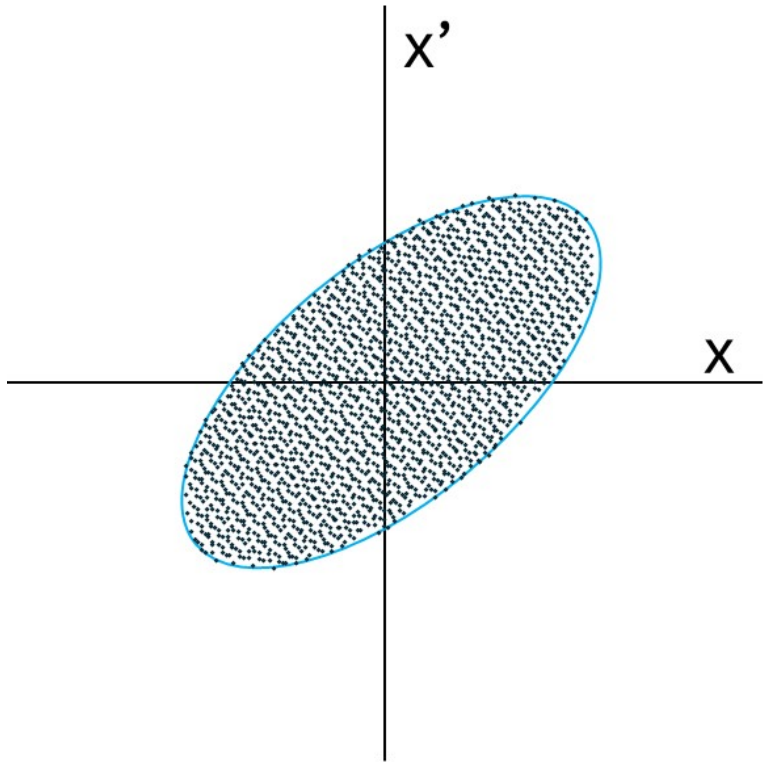


Figure 1.3 Example phase space diagram.

electrons which push the bunch apart over time as all of the particles are the same charge and repel each other. Space charge emittance can be modeled as seen in Eq. 1.2 [3]. Increasing the charge contained in a bunch increases the space charge emittance experienced while enlarging the bunch and increasing the electric field it experiences, equivalent to increasing bunch energy, decreases space charge.

$$\varepsilon_{sc} = \frac{\pi I}{4\alpha k I_A \sin\theta} \frac{1}{3\frac{\sigma_x}{\sigma_z} + 5} \tag{1.2}$$

$$\alpha = \frac{eE}{2mkc^2} \tag{1.3}$$

The RF emittance is due to the diverging field effects seen as the particles deviate from the on-axis field inside of an RF cavity. The equation for RF emittance is shown in Eq. 1.4 [3]. The stronger the RF field and the larger the bunch the worse the RF emittance contribution becomes. They create conflicting parameters between space charge which wants a large bunch and high field and RF emittance which is lowest with a small bunch and low field. This is discussed more in

Chapter 2.

$$\varepsilon_{rf} = \frac{\alpha k^3 \sigma_x^2 \sigma_z^2}{\sqrt{2}} \tag{1.4}$$

The intrinsic emittance is the result of the cathode and laser spot used to trigger photoemission into vacuum, as seen in Eq. 1.5. A high MTE material and large spot size increase the intrinsic emittance contribution. Space charge and RF emittance contributions are typically the dominant emittance contributions but as methods have improved to manage these contributions more focus has been placed on decreasing intrinsic emittance and ensuring cathodes are performing as expected, this is explored more in Chapter 3.

$$\varepsilon_{int} = \frac{\sigma_{xi}}{m_e c}\sqrt{2 \cdot m_e \cdot e \cdot MTE}, \tag{1.5}$$

### 1.1.5 Brightness

Brightness is a common figure of merit in the accelerator community [4]. It is defined in Eq. 1.6 where it depends on the current of the bunch and the bunch emittance. A large current and small emittance are needed for high brightness.

$$B = \frac{2I}{\varepsilon^2} \tag{1.6}$$

This corresponds to an electron-dense bunch with a small phase space footprint and a small diameter bunch with small differences in energy between electrons. Unfortunately, these attributes are non-cooperative due to things like space charge effects which increase with both charge per bunch and decreasing bunch size. Thus extra steps must be taken to analyze the emittance and current to maximize the brightness. This is explored in Chapters 2-4.

### 1.1.6 Beam Energy

Beam energy is a measure of the longitudinal kinetic energy of a bunch of particles. Typically, particles gain energy by undergoing acceleration due to an electric field inside an accelerating cavity. The higher the energy of a particle bunch the more energy is required to manipulate it,

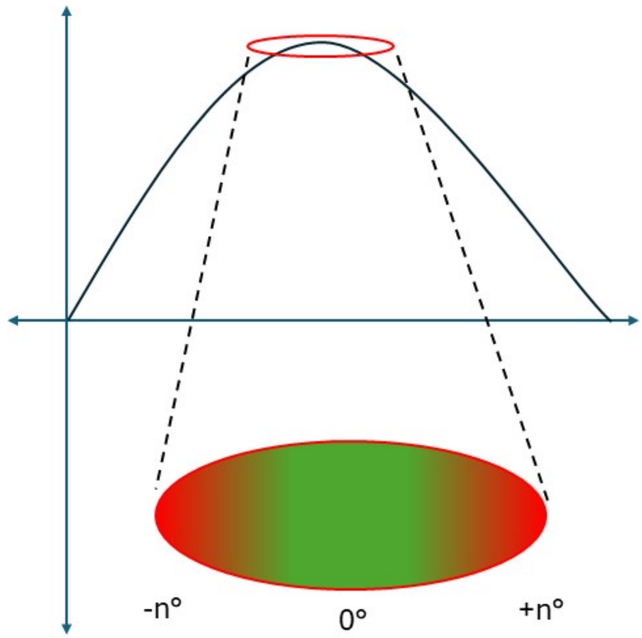


Figure 1.4 An example of the energy spread produced by RF acceleration.

leading to a higher energy beam being more difficult to manipulate overall. However high energy bunches are less susceptible to the effects of space charge interactions over their lifetime when compared to a lower energy beam.

### 1.1.7 Energy Spread

Energy spread is a measure of the variation in the energy of the particle in a bunch and has a variety of factors. In photoemission, the amount of energy that the particle escapes the surface with varies slightly in magnitude and direction leading to particles with varying longitudinal energy. Additionally, particularly for longer bunches, the electric field experienced in on crest RF accelerating cavity is not flat leading to energy spread, see Fig. 1.4.

Finally, particularly for wide-diameter bunches, the electric field of an RF accelerating cavity decreases radially leading to slower particles at the edge of a bunch which results in a larger energy spread. Energy spread can be minimized with low MTE cathode materials, as well as short, small-diameter bunches.

### 1.1.8 Free Electron Lasers

Free Electron Lasers (FELs) are a type of particle accelerator that uses high-energy electrons and undulators to produce photons with a variety of wavelengths. The light produced by an FEL is then exposed to a sample with which it interacts. The resulting light can then be analyzed and interpreted to image extremely fast and small events. FELs are commonly operated as user facilities where groups from a variety of scientific communities can perform experiments. Such experiments are useful in a variety of fields such as Material sciences, chemical sciences, and biological and medical sciences. All these fields work with materials/chemicals/samples where the exact structure and moment-to-moment changes provide critical information for the field. FELs provide a way to image these precise structures and the brighter the FEL the more detail can be obtained as the brightness of the bunch corresponds to the number of photons used as well as how tightly packed, they are. The more intense and focused the bunch of light is the better images can be produced and the more information gained in an experiment[5–7].

### 1.1.9 Ultra-Fast Electron Diffraction

Ultra-Fast Electron Diffraction (UED) is a process that uses electron beams to directly image a material. Electrons scattering off of a material produce diffraction patterns which can be observed and processed to provide detailed descriptions of the atomic structure of a material. Additionally, this the done at a high repetition rate allowing observations of changes in the material equal to the number of bunches used. Similarly to FELs, there are a wide variety of scientific fields that can benefit from this kind of understanding of a material or sample. Material, solid state, and biological sciences all regularly deal with these small length and time scales. The brightness of the bunches used directly affects the quality of the results produced as the number of electrons per second increases resolution, while low emittance ensures that the only effects experienced by the bunch are those related to the material being examined. Further improvements to brightness will only serve to increase the overall resolution of the images produced [8–10].

### 1.1.10 Laser Compton Back Scattering

Laser Compton Back Scattering (LCBS) is a process in which an electron bunch interacts with a photon bunch from a laser. This increases the photon's energy while also making then monoenergetic and polarized. The resulting photon beam is useful in the same applications as discussed in the FELs and UED sections. Increasing the brightness of the electron bunch has the benefit of increasing the photon yield and distribution from the election laser interaction which leads to improved resolution of the resulting photons making them more useful for precise applications[11, 12].

## 1.2 Electromagnetic Field for Accelerators

### 1.2.1 Modes

An electromagnetic field mode refers to the electric and magnetic field distribution inside a given volume terminated by conductive boundaries. More specifically a mode is defined by the number of zero crossings or nulls present in a given field distribution. These nulls are located either longitudinally, transversely, or axially from the origin of a given volume. Additionally, either the electric or magnetic field will lie in the transverse direction defining the type of mode, either transverse magnetic, TM, or transverse electric, TE. This results in a naming convention defined by first either TM(p,m,n) or TE(p,m,n) indicating the directions for the fields and then three numbers counting the number of nulls in the specified direction. The order of the numbers goes as axial nulls, longitudinal nulls, and finally transverse nulls. The number of nulls as well as the field directions are determined by the shape of the cavity. The volume of the cavity and more specifically the length and width of the space determine which modes can occur inside the cavity. Choosing the dimensions of a cavity carefully is of high importance when designing a cavity as there will likely be modes occurring that are undesirable to the end performance. Thus, designing a cavity that produces the desired mode while also dampening or spacing the undesired modes far enough away to not be excited is common practice.

### 1.2.2 Accelerator Cavities

Single-cell accelerating cavities work by using the TM 010 mode to produce an on-axis electric field which is used to accelerate the particles. Only half of the waveform can be used to accelerate the particles in the desired direction thus the phase of the electric field is critical to achieving the desired effect. Additionally, to maximize energy gain the particle needs to be injected near the crest of the wave. This limits the usable area of the wave if maximizing energy gain is the goal. The bunch length also plays a factor in this as the length of the bunch determines the number of degrees on the wave it is spread across. A large bunch will experience more energy spread when compared to a short bunch given the limited number of degrees with similar energy gain near the crest of the field.

### 1.2.3 Pillbox

A pillbox cavity is a simple cavity design shaped like a rectangular box, see Fig. 1.5. This allows for easy predictable modes to occur in a given volume. However, the sharp corners can limit high gradient operation as they make arcing and consequent quenching more common.

### 1.2.4 Reentrant

A reentrant cavity design is more complicated in design, having a rounded volume and nose cones, see Fig. 1.6. These features allow for operation at higher gradients as well as the decreased field in the beam pipes as the nose cones provide some shielding and limit a particle bunch's exposure to only the desired portion of the field. Their more complicated geometry can make acquiring the desired mode more complicated than a pillbox but the same theory applies. More details will be provided in Chapter 4.

### 1.2.5 Quality Factor

The quality factor is a common figure of merit for RF cavities. There are several different Q factors which all provide different information about the cavity and circuits used. The external Q factor measures the energy dissipated in the external circuits. The loaded Q factor measures the energy dissipated in the complete system, the circuits, and the cavity. Finally, the unloaded Q factor measures the energy dissipated in the cavity and is the preferred metric as it only takes into

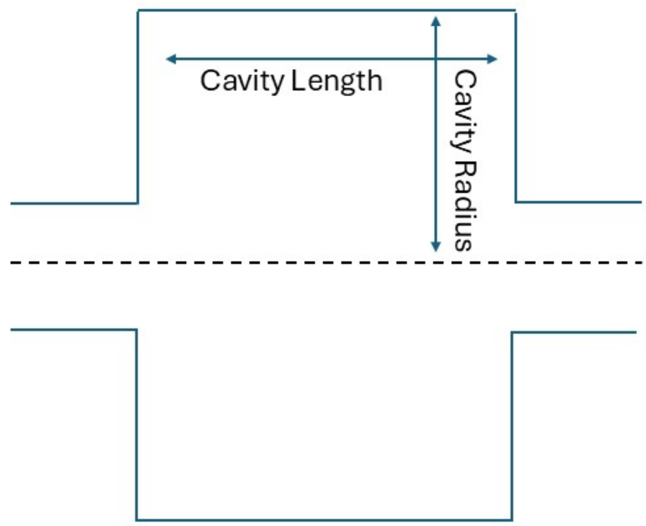


Figure 1.5 An example pillbox cavity.

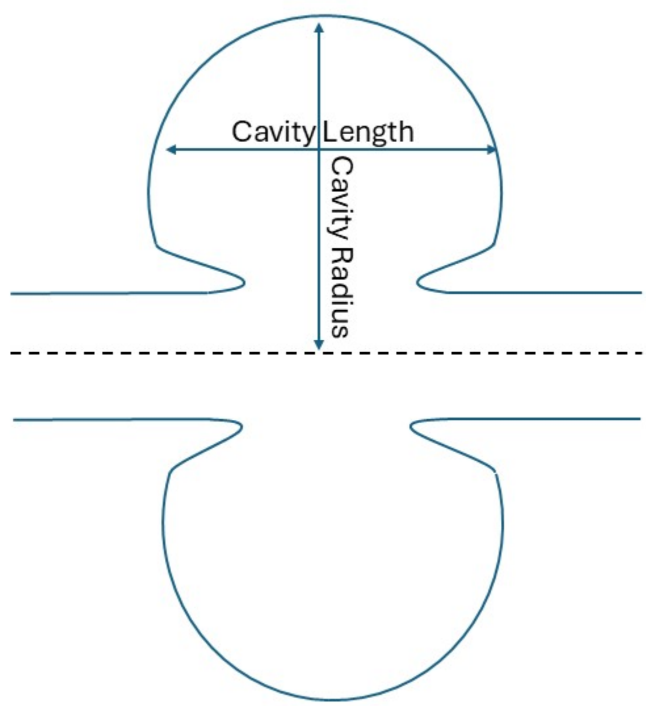


Figure 1.6 An example reentrant cavity.

account the cavity being measured. Unfortunately, the unloaded Q factor can't be simply measured and must be calculated based on measurements taken from the cavity. Measuring the unloaded Q factor is explained more in Chapter 4 but the general steps involve ensuring a critically coupled probe provides power, and a weakly coupled probe picks up the response from the cavity. This ensures that the cumulative coupling coefficient $\beta$ for the couplers is as close to 1 as possible, as can be seen in Eq. 1.7 [13], this allows the loaded Q factor measured on a VNA to be multiplied by 2 resulting in an approximation of the unloaded Q factor.

$$Q_0 = Q_L \cdot (1 + \beta_{11} + \beta_{21}) \tag{1.7}$$

$$Q_L = \frac{\omega_0}{\Delta\omega} \tag{1.8}$$

# CHAPTER 2

## EMITTANCE MAPPING IN RF GUNS

This chapter is based on the author's published paper: **B. Sims** and S. V. Baryshev, "Emittance mapping in rf guns", *Physical Review Accelerators and Beams* 26, 113402 (2023), https://journals.aps.org/prab/abstract/10.1103/PhysRevAccelBeams.26.113402

This chapter discusses the trends and trade-offs between transverse $\sigma_x$ and longitudinal $\sigma_z$ bunch dimensions, rf injector gradient, bunch charge, and intrinsic electron mean transverse energy (MTE), where all can be chosen to be independent, and the resulting effects on emittance and transverse brightness. Using a practical example of a quarter wave normal conducting photoinjector, it is computationally found that regardless of MTE and bunch charge, there is a universal relation between the gradient $E$ and the aspect ratio of the bunch $(\sigma_x/\sigma_z)$ leading to the highest brightness. This computational result is understood using an analytical formalism consisting of K-J Kim's emittance formulation and a two-dimensional space charge model. The results, obtained computationally and interpreted in a robust physical framework, could therefore provide the basis for an express mapping approach for emittance forecasting when used with practical injector system design requirements and limitations.

### 2.1 Introduction

High brightness and high current rf photo-injectors are instrumental in the progression of accelerator technology and are critical for many different applications in basic sciences, medicine, and industry [14–17]. As high brightness and high current are two counter-conflicting figures of merit [18], in order to achieve high brightness the emittance (spatiotemporal spread) needs to remain as low as possible, while maintaining a high charge. Hence, the route to achieving particular brightness/charge goals lacks universality: in each particular setting an iterative process is used to reduce the emittance [16, 18–23]. Additionally, optimization is carried out along with the use of additional beam line elements like bunchers, solenoids, or beam heaters which makes the optimization process intertwined, thereby raising complexity [16, 18–23]. Because the final emittance of a bunch down the linac machine can be strongly attributed to the initial beam quality,

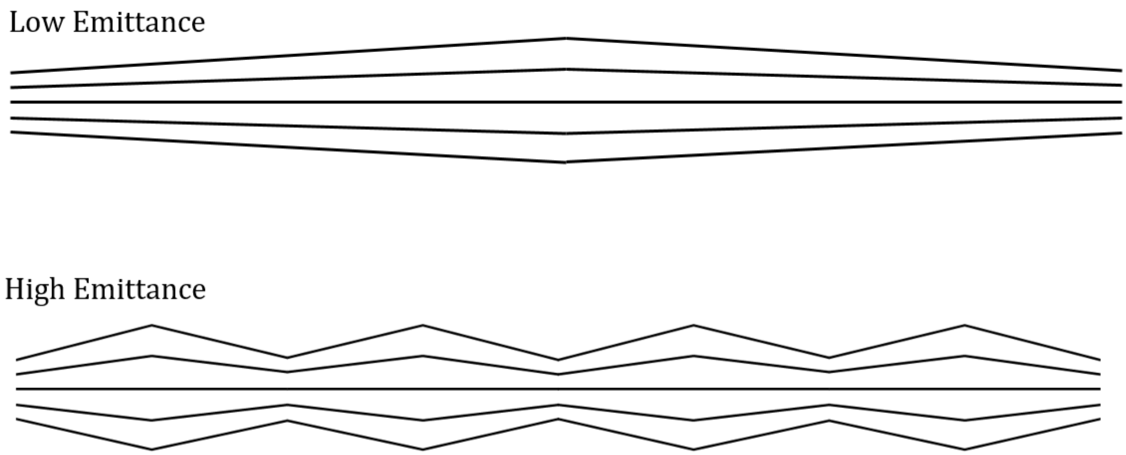


Figure 2.1 The concept of the low emittance gun and its effect on focusability as the beam moves down the optical lattice through focal points.

it highlights the need for an intricate understanding of initial conditions [17, 24]. Therefore, an alternative approach would be to reduce complexity or, in other words, to understand the interplay between primal parameters, namely, incident laser pulse length and spot size [25]. The laser parameters on the photocathode are used to engineer a desired bunch shape, thereby lowering the emittance early in the injector for a given charge, mean transverse energy, gradient and phase structure. The optimal bunch is then much simpler to maintain throughout due to a better beam focusability [26], as illustrated in Fig.2.1. Practically, another benefit of this approach is a reduced number of optical lattice components necessary to achieve the desired brightness [16], while informing optimal parameters for injector and laser design.

The described simplex approach has some interesting challenges to overcome as for the current to be high, the laser pulse dimensions need to be minimized while the charge per bunch is maximized [3], whilst the same parameters need to be optimized to achieve the highest brightness [27]. The low emittance required of the bunch necessitates minimizing the space charge emittance while also managing the rf and intrinsic emittance contributions [28]. The intrinsic emittance can easily be dominated by the space charge or rf emittance following emission from the cathode surface and thus low MTE cathodes are no longer a strong method of transverse emittance reduction [29]. In order to manipulate the peak current and brightness through emittance optimizations, the additional parameter of surface electric gradient has to be added. Once added, the injector design quickly becomes a multivariate optimization problem where mathematical minima for best performance are sought after using computational algorithms [30, 31]. Thanks to the simplicity of the injector emittance minimization approach, the optimization algorithm can be cross-verified analytically, thereby helping establish more universal relationships between laser and rf injector cavity subsystems, and the resulting bunch parametrization and emittance mapping.

### 2.2 Case study setup

To illustrate the described ideas, emittance of the Argonne Cathode Teststand (ACT) photo-injector was mapped and optimized. The ACT gun is a canonical quarter-wave normal conducting L-band (1.3 GHz) injector that was thoroughly described and verified computationally and experimentally [32, 33]. The laser spot was defined as a radially uniform circle while the pulse length was a Gaussian distribution clipped at $3\sigma$ (99.7-rule). The ACT has two solenoids: one, wrapped around the gun, is used for emittance compensation, and one, at the end of the injector, is used for focusing the bunch onto the target. Because the main idea of this work is to optimize for minimal emittance without the use of additional focusing apparatuses, both solenoids were disabled in the simulations to isolate the fundamental emittance effects (MTE, space charge and rf) on the bunch. The simplicity of the ACT injector allows for extensive analysis and effective demonstration of the emittances at play. Together, the gradient $E$ and its phase structure, $\sigma_x$ and $\sigma_z$, form a parameter space that needs to be analyzed to provide the best injector and drive laser beam settings to increase the brightness. The choice of metal (low QE, short response time) versus semiconductor (high QE, long response time) photocathodes and their MTE determine the limitations of the primary laser pulse length $\sigma_z$, and the spot/source size $\sigma_x$. This work explores emittance optimization at 10, 30, 50, 70, and 90 MV/m to cover the full operating range of the ACT [34] as well as illustrate the differences that each gradient requires. The contribution to the emittance from the cathode material also cannot be overlooked, and ~0 meV MTE material (at Boltzmann tail operation) and a 200 meV (common approximation) MTE were compared. These examples allow us to emphasize important nuances of minimizing emittance in modern low-gradient SRF guns [35] against high and ultrahigh-gradient copper guns operated at room and cryogenic temperatures [36].

### 2.3 Methods and Definitions

The simulations were performed using General Particle Tracer (GPT) [37], a robust simulation program of choice in photoinjector community that has emphasis on space charge dynamics. Emittance heatmaps were generated which mapped the topography of the pulse length and spot size environment. All particle simulations were done in GPT with space charge effects enabled. Each simulation consisted of either 10 pC or 100 pC per laser pulse. These two levels of charge are considered state-of-the-art for future systems and applications, e.g. these levels are considered as main operating conditions for the low emittance injector (LEI), a core upgrade step for the LCLS-II-HE project [14, 18]. Considered charge was spread over 1,000 macro-particles to reduce computational time when generating heatmaps. A field map of the ACT was used, and all simulations were performed until the end of the injector, 8 cm away from the cathode surface set as the origin [32, 34]. The two distinctly different MTE, 0 versus 200 meV were chosen. 0 meV was approximated as 1 meV in the simulations and represents copper cathode operated in cryogenic copper injectors [38]. While 200 meV represents the standard MTE expectation for most photocathodes at room temperature with emission above the threshold, i.e. outside Boltzmann tail regime; one example being $Cs_3Sb$ [39] which is being considered for the low emittance injector for LCLS-II HE.

The pulse length was scanned from a 1 ps gaussian pulse clipped at $3\sigma$ to a 20 ps gaussian pulse also clipped at $3\sigma$. The minimum pulse length was chosen as a cut-off to avoid space charge locking after observing the beam tracking, where not all of the particles were emitted from the surface. Space charge locking occurs when enough charge is present near the cathode surface, thereby negating the electric field on the cathode. Once this occurs, particles are still emitted from the cathode due to the photoelectric effect but are no longer accelerated by the field. This results in a reduced charge yield from the given laser pulse and a misshapen bunch dependent on when the charge locking occurred. There is an additional difficulty in GPT where the particles can't be reabsorbed by the cathode and instead are accelerated backwards in the simulation. In many cases this breaks the simulation and the space charge locking effect needs to be avoided in GPT simulations. The spot size radius was examined from 0.4 mm to 1 mm. The minimum size was chosen again using the same criterion to avoid space charge locking. These simulation parameters were then repeated at 10, 30, 50, 70, and 90 MV/m.

### 2.3.1 Normalized Transverse Emittance

The transverse emittance of a bunch is defined as the area of the ellipse in the momentum phase space that the bunch occupies. The emittance can be calculated using a statistical root mean square (RMS) approach. If the bunch is assumed radially uniform, the $\varepsilon_x$ and $\varepsilon_y$ emittances are identical, only the $\varepsilon_x$ needs to be calculated. The statistical definition of $\varepsilon_x$ is shown in Eq.2.1 and was used to calculate all emittances that follow.

$$\varepsilon_x = \sqrt{\langle x^2 \rangle \langle x'^2 \rangle - \langle x^2 \cdot x'^2 \rangle} \tag{2.1}$$

The particle locations, $x$, as well as the normalized transverse momentum, $x'$, are required to calculate the emittance. These values were computed in GPT and exported for calculation separately instead of using GPT's built-in emittance calculation routines. GPT calculates normalized transverse emittance in the velocity space using only $\beta_x$ [37]. Instead the normalized transverse emittance was calculated using Eqs.2.2-2.6. It was calculated as

$$\beta_x = \frac{v_x}{c} \tag{2.2}$$

$$p_x^N = \frac{p_x}{mc} = \gamma \beta_x = x' \tag{2.3}$$

$$\varepsilon_x = \sqrt{\langle x^2 \rangle \langle (\gamma \beta_x)^2 \rangle - \langle x^2 \cdot (\gamma \beta_x)^2 \rangle} \tag{2.4}$$

To normalize the $\varepsilon_x$ it was scaled by $\beta_z$ and $\gamma$ as shown in Eq.2.6. This was done to ensure equitable comparison regardless of the energy of the bunch resulting from other injectors or field strengths.

$$\beta_z = \frac{v_z}{c} \tag{2.5}$$

$$\varepsilon_n = \gamma\beta_z\varepsilon_x \tag{2.6}$$

### 2.3.2 Brightness

The brightness of a beam has two components, the current and the emittance. From Eq.2.7, the brightness is linearly proportional to current but inversely proportional to the square of the emittance:

$$B = \frac{2I}{\varepsilon^2} \tag{2.7}$$

## 2.4 Results

The arrays of the 100 cell by 100 cell heatmaps presented below examine emittance in the parameter space defined by beam form factors at gradients of 10, 30, 50, 70, 90 MV/m for the described ACT photoinjector. The number of macro-particles used in the GPT simulations was set to 1,000. This was necessary for achieving high resolution of the emittance heatmaps (within a reasonable computational time frame of approximately 24 hours per heatmap), and, in turn, allowing for identifying critical trends. The cost of reducing the number of macroparticles was decreased accuracy of the individual emittance values calculated. It was estimated that the emittance was within ±17% of low resolution heatmap simulations conducted with 1,000,000 particles. Hence the established value of decreased resolution does not affect the basic conclusions and findings deduced from the high resolution heatmap analyses.

### 2.4.1 10 pC, 0 MTE

Fig.2.2 illustrates that the optimal bunch configuration is extremely dependent on the gradient, and guides on how the charge needs to be distributed to mitigate the space charge effect. More specifically, the 10 MV/m heatmap suggests the pancake regime, thereby implicating that the best emittance is achieved through the shortest pulse (smallest $\sigma_z$) and largest spot size (largest $\sigma_x$).

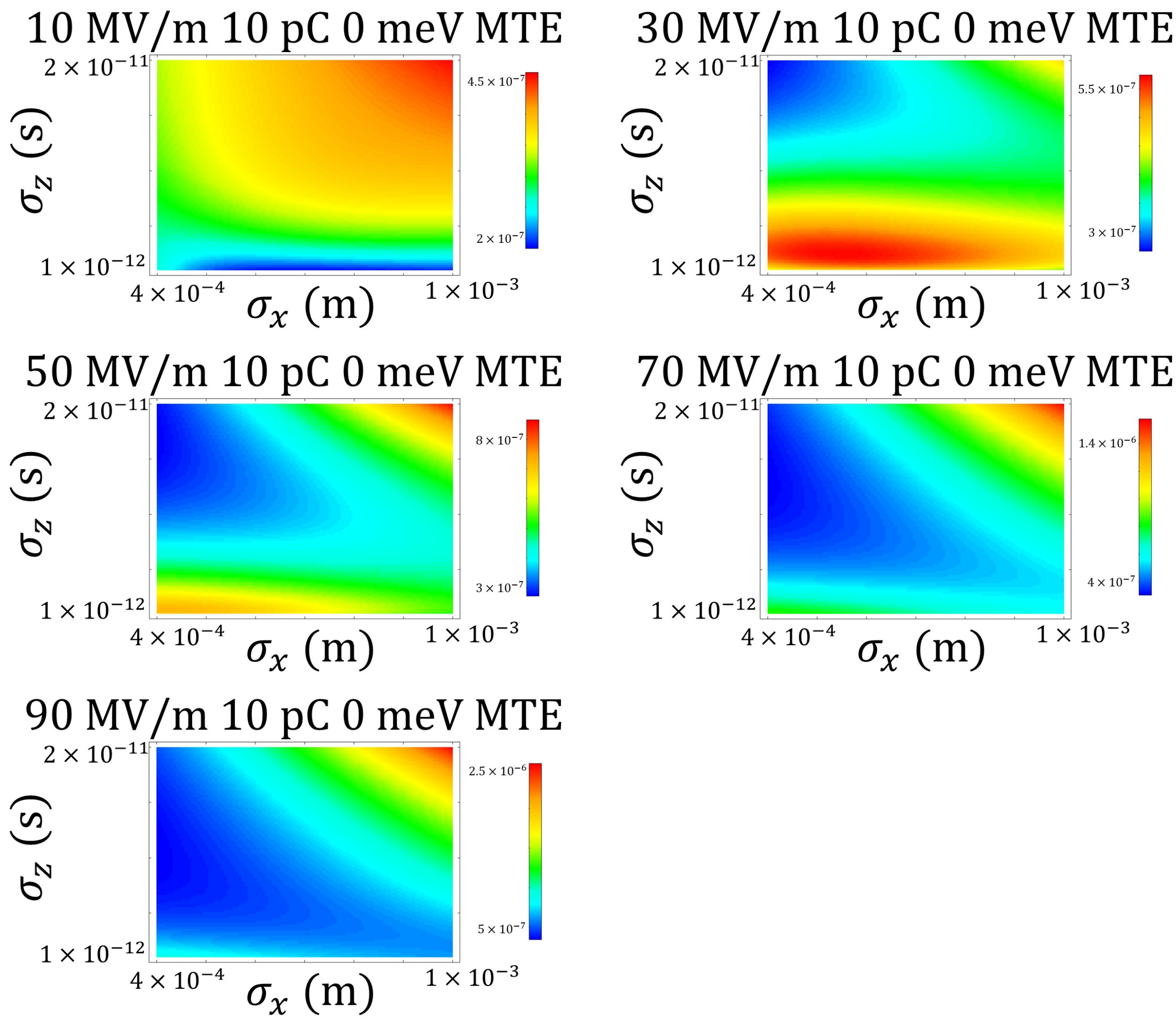


Figure 2.2 Series of heatmaps for 10 pC and 0 MTE case study demonstrating beam form factor evolution at different gradients. Slight increase of the emittance floor as the gradient is swept from 10 to 90 MV/m is because of the rf emittance contribution due to long bunch.

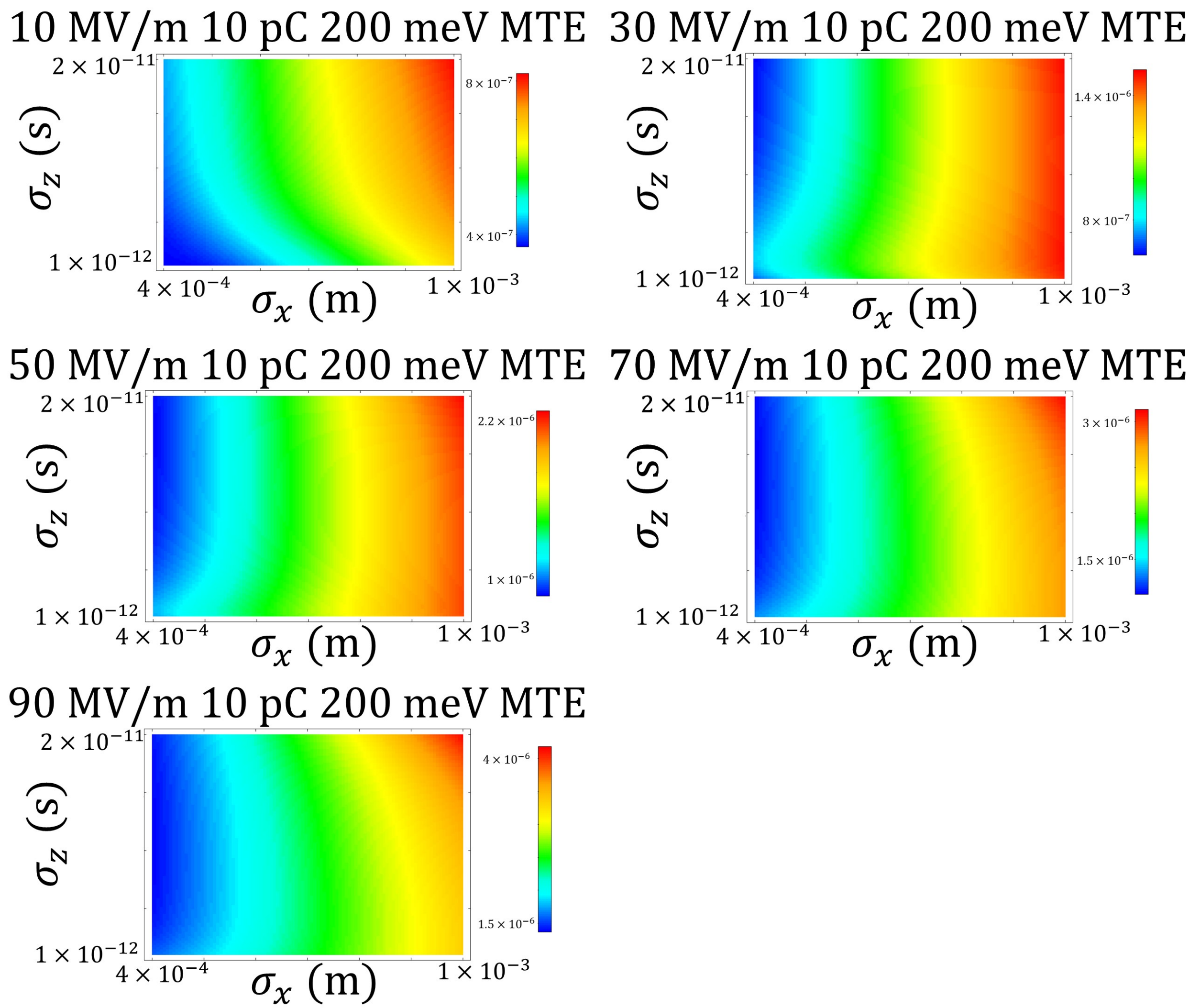


Figure 2.3 Series of heatmaps for 10 pC and 200 meV MTE case study demonstrating beam form factor evolution at different gradients. 10 MV/m minimal emittance location shifted to a short ellipse bunch shape. Higher gradients, again, indicate cigar beam as optimal.

Moving on to the 30 MV/m case study, the situation flips, and the cigar regime is implicated (blue upper left corner of the heatmap), thereby requiring much smaller $\sigma_x$ and much larger $\sigma_z$. When analyzed in the context of brightness, there are additional factors to consider. The brightness depends on current and the current increases as pulse length decreases. As a result, having a minimal pulse length and minimal emittance is important. The minimum emittance for each heatmap also increases with the gradient. This is due to the increasing effects of the rf emittance on the bunch as the gradient increases.

### 2.4.2 10 pC, 200 meV MTE

Moving from the previous, rather idealized, case to one where the intrinsic emittance is no longer effectively a zero, this produces a new set of data that differ from the previous case study. Here, the intrinsic emittance is calculated as

$$\varepsilon_{int} = \frac{\sigma_{xi}}{m_e c}\sqrt{2 \cdot m_e \cdot e \cdot MTE}, \tag{2.8}$$

where the intrinsic emittance now depends on the initial spot size of the bunch $\sigma_{xi}$. It should, again, be noted that the resulting emittances plotted in all of the heatmaps are calculated purely based on the statistics of the energy and position of the electrons, see Eq.2.4.

In the 10 MV/m simulation, the lowest emittance is attained when $\sigma_x$ and $\sigma_z$ are on par in terms of the size, thereby requiring that the beam is no longer a pancake form-factor but rather a short ellipse. This result is expected as emittance is proportional to $\sigma_x$ while being affected by an MTE that is now 200 times larger (1 versus 200 meV), thereby requiring $\sigma_x$ to reduce. Otherwise, heatmaps in Fig.2.3 corresponding to 30, 50, 70, and 90 MV/m demonstrate trends similar to those in Fig.2.2. The higher the gradient, the more the bunch is required to shape into a cigar form factor. However, with the increased effect of the intrinsic emittance, the area of minimal emittance is much more restricted as the bunch can no longer benefit from an increased spot size. Which results in the minimum emittance staying near the smallest spot size possible.

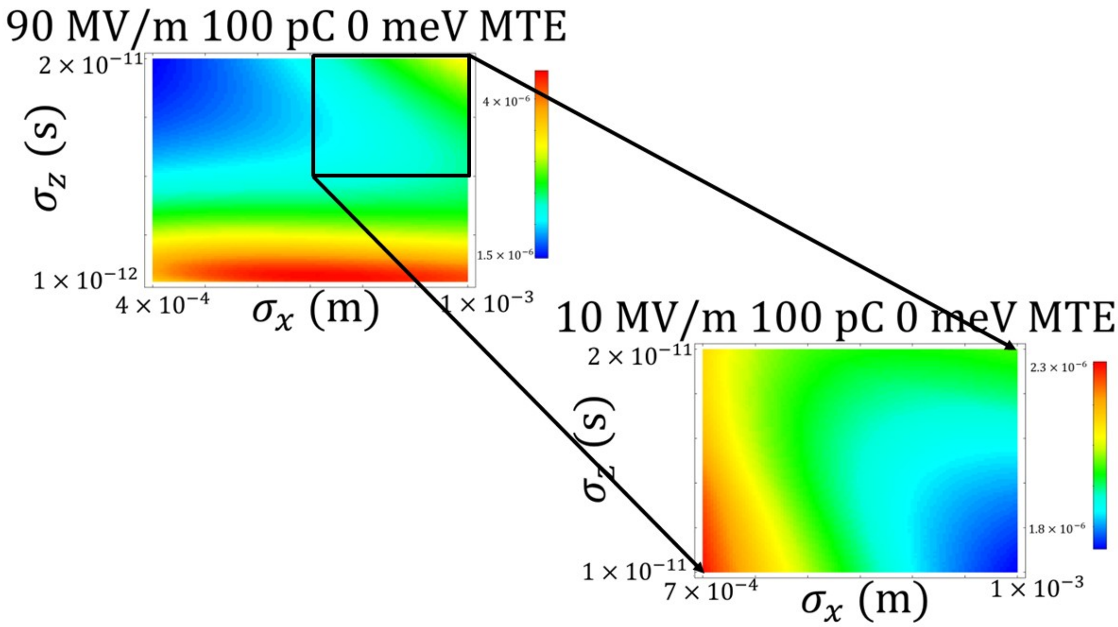


Figure 2.4 Demonstration of the parameter space cutout for 100 pC 0 MTE case study that had to be performed because of enhanced space charge screening effect at the cathode surface.

### 2.4.3 100 pC, 0 MTE

When working with the ambitiously high bunch charge of 100 pC, the $\sigma_x - \sigma_z$ range had to be adjusted for the 10 MV/m gradient case. Due to a ten-fold charge increase, it was found that no particles would leave the cathode surface due to space charge locking. The electrons would effectively create a wall of charge negating the field of the gun at the cathode, leading to electrons emitted later in the pulse returning to the cathode. The $\sigma_x - \sigma_z$ range where charge locking was not present is shown in Fig.2.4. As can be seen, the maximum pulse length was held constant while the minimum pulse length boundary was increased to $10^{-11}$ s, while $\sigma_x$ was only run from 0.7 to 1 mm. The main result was that the minimal emittance location is in the lower right corner, a perfect pancake bunch.

At 30 MV/m, it flips to opposite upper left corner, perfect cigar bunch. Expanding this result, an ideal high charge bunch at low gradients would be a perfect (infinitely thin) disk, whereas an ideal high charge bunch at high gradients would look like a line of charge. These bunch designs would be impossible with current technologies but do provide useful reference points

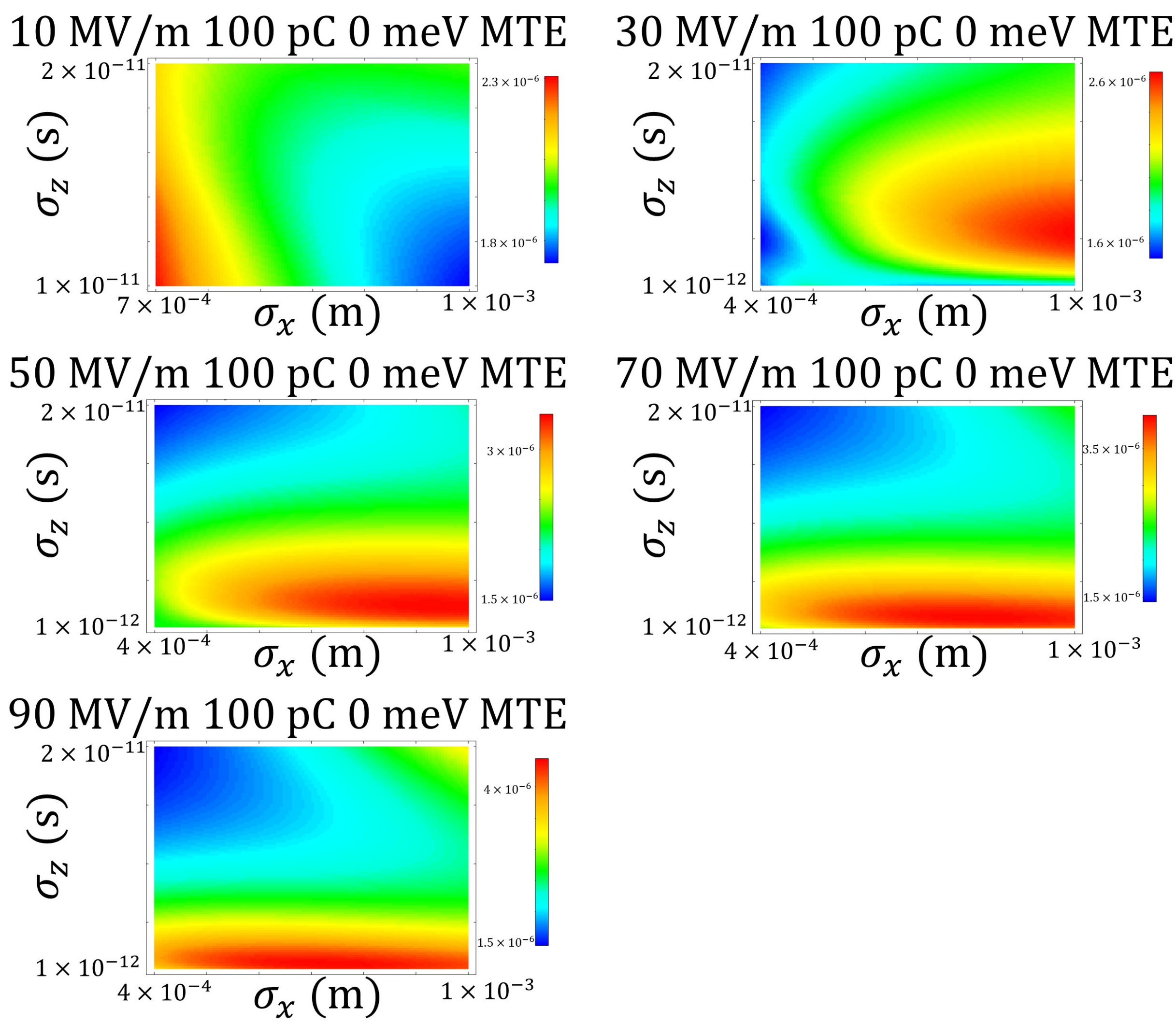


Figure 2.5 Series of heatmaps for 100 pC and 0 MTE case study demonstrating beam form factor evolution at different gradients. The optimal emittance minima locations are identified to be in the corners indicating a strong need for either pancake or cigar bunches.

when thinking about practical accelerators and their limitations, as well as for the designing bunch shape for a specific experiment. As the gradient grows from 30 to 90 MV/m, the range enabling minimal emittance extends, which is simply because higher gradients more strongly compensate the coulombic repulsion force. Otherwise, the emittance baseline increased because of the stronger space charge effect as compared to 10 pC bunch charge. All of these results are summarized in Fig.2.5.

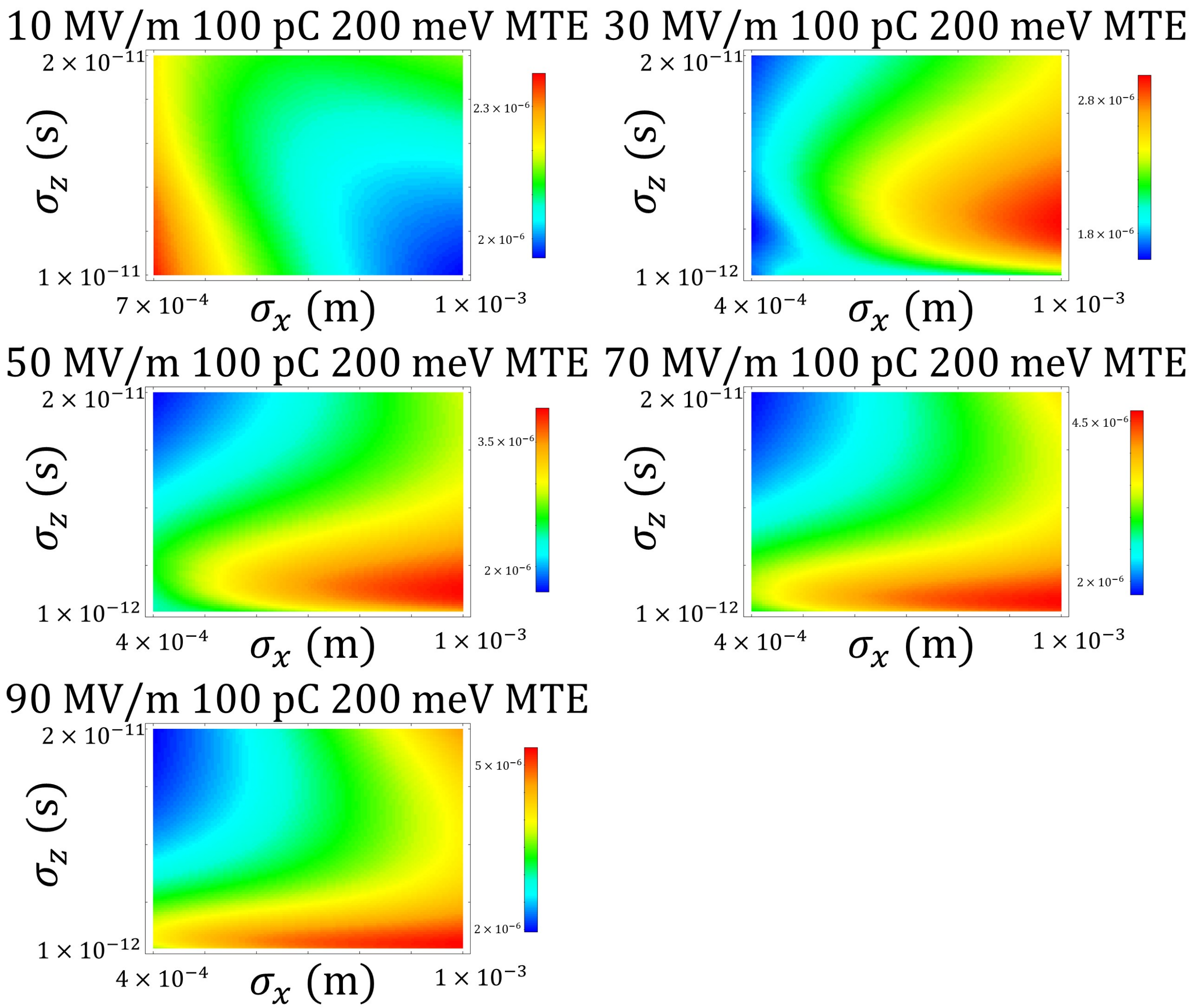


Figure 2.6 Series of heatmaps for 100 pC and 200 meV MTE case study demonstrating beam form factor evolution at different gradients. Inclusion of intrinsic emittance leads to minor increase in emittance across the board and a reduction in minimal emittance area as compared to Fig.2.5.

### 2.4.4 100 pC, 200 meV MTE

Compared to the 100 pC 0 MTE case study, the new set of the heatmaps remained nearly the same as can be seen in Fig.2.6. The space charge effect is exceptionally strong and therefore conceals the intrinsic emittance effect, despite the fact that $\sigma_x$ has to be the largest possible. The only effect the intrinsic emittance has is that it slightly increases the minimal emittance baseline from $1.5 \times 10^{-6}$ to $2 \times 10^{-6}$ m.

## 2.5 Discussion

There were two effects observed:

1) The interactions between the space charge and intrinsic emittance were immediately understood and discussed in Section 2.4. In short, minimizing space charge is best attained with a large cross section bunch while minimizing intrinsic emittance is best accomplished with a tight small cross section bunch. This results in two counter processes and an optimized solution should be found to minimize both emittances such that total emittance is minimal.

2) General trends suggesting that for best practices (lowest emittance and thus highest brightness) the bunch (regardless of the bunch charge and intrinsic emittance) has to be reshaped from the pancake aspect ratio, as under low gradient, to the cigar aspect ratio, as under high gradient. This result merits a separate discussion. To do that, the individual emittance components are analyzed, as the total emittance can then be calculated through the summation of the individual emittance components. The individual emittance components considered are the rf emittance, space charge emittance, and the intrinsic emittance, as defined in Eq.2.8, which is set to zero as it fundamentally does not affect the pancake to cigar switching.

The space charge and rf emittance components can be written as [3]

$$\varepsilon_{sc} = \frac{\pi I}{4\alpha k I_A \sin\theta} \frac{1}{3\frac{\sigma_x}{\sigma_z} + 5} \tag{2.9}$$

$$\varepsilon_{rf} = \frac{\alpha k^3 \sigma_x^2 \sigma_z^2}{\sqrt{2}} \tag{2.10}$$

where $\alpha = \frac{eE}{2mkc^2}$. It is important to note that the $\sigma_z$ and $\sigma_x$ described here are not the initial pulse length and spot sizes, but the $\sigma_z$ and $\sigma_x$ of the bunch as it travels through the beam line. As the space charge emittance is proportional to the emitted current, the current is required. The current is conventionally charge per time. However, the time component depends on the shape of the bunch. To resolve this convoluted situation, we analyzed two distinct cases. For a long bunch, where $\sigma_z$ is larger than $\sigma_x$, the time is defined by Eq.2.11 derived in Ref.[25]. The long pulse length, in this case, allows the electron ample time to escape the surface and is not a limiting factor.

$$\delta t_{Pulse} = \sqrt{\frac{2m\sigma_z}{eE}} \cong \sqrt{\frac{\sigma_z}{E}} \tag{2.11}$$

In the contrasting case, where $\sigma_x$ is larger than $\sigma_z$, the dynamics occurring at the surface require a different definition of the characteristic time scale. As the pulse length is short in this case, there is a characteristic minimum time for the electron to be emitted from the surface and can described as [25]

$$\tau_{Response} = \sqrt{\frac{2m\sigma_x}{eE}} \cong \sqrt{\frac{\sigma_x}{E}} \tag{2.12}$$

These two cases, when linked with the emittance equations above, allow for analysis of the relations between the gradient, $\sigma_x$ and $\sigma_z$. In the $\sigma_x < \sigma_z$ case, substitution of Eq.2.11 to Eq.2.9 yields Eq.2.13, which creates a situation where the only variables that can be changed to minimize emittance are the gradient and $\sigma_z$. Both values would need to be increased to minimize the space charge emittance. Thus, the case of $\sigma_x < \sigma_z$, or the cigar beam case, is equivalent to the high gradient case, as the electric field needs to be increased to decrease the emittance. The rf emittance as in Eq.2.14 derived from Eq.2.10 would then increase in this situation, which is why the spot size $\sigma_x$ needs to be reduced to compensate, thereby making the cigar aspect ratio more pronounced. Such analytical formalism therefore fully explains the consistency between the high gradient and the cigar beam regime as visualized by the obtained heatmaps.

$$\varepsilon_{sc} = \frac{Q}{\sqrt{E}} \frac{1}{\sqrt{\sigma_z}} \tag{2.13}$$

$$\varepsilon_{rf} \approx E\sigma_x^2\sigma_z^2 \tag{2.14}$$

For the $\sigma_x > \sigma_z$, or pancake aspect ratio, we define time as in Eq.2.12. In this case, the space charge emittance can be simplified as seen in Eq.2.15, while rf emittance as in Eq.2.14. It becomes clear that, in order to, first and foremost, minimize the space charge emittance, term $\sigma_z$ has to be decreased and $\sigma_x$ has to be increased. The growth of the rf emittance term associated with the $\sigma_x$ growth is countered by the drop in $\sigma_z$. Again, it fully explains the consistency between the low

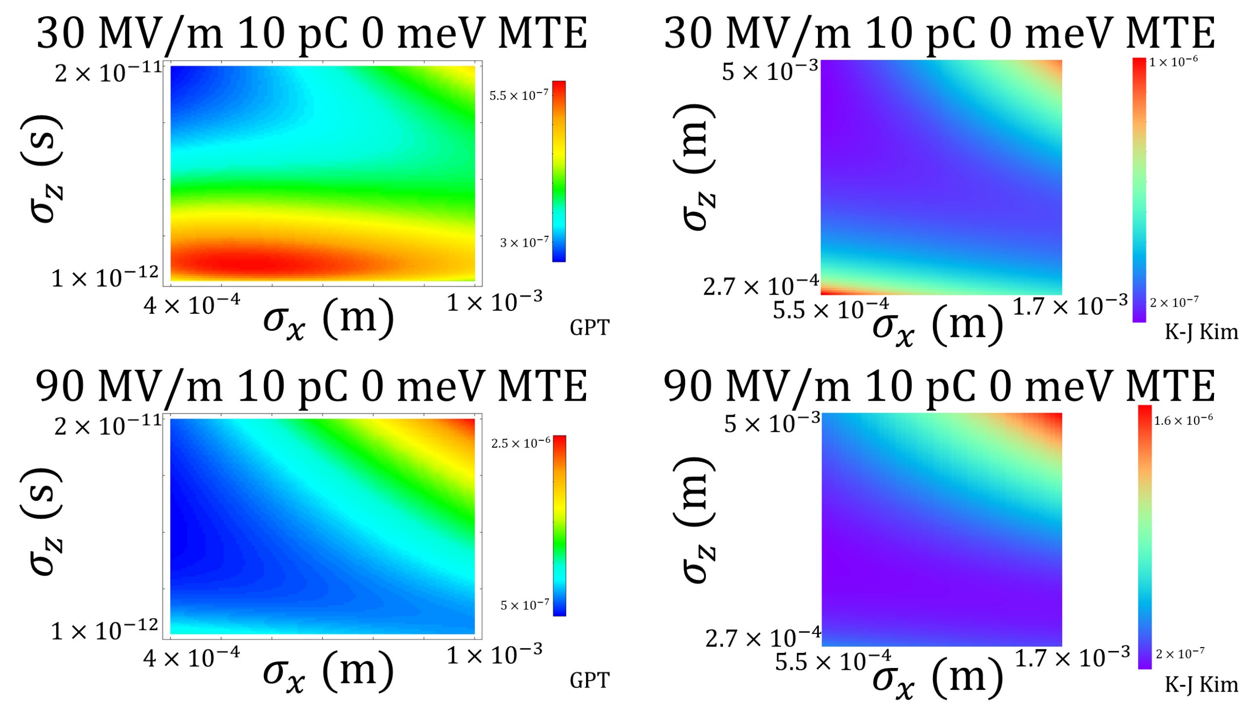


Figure 2.7 Back-to-back comparison of the emittance heatmaps for 30 and 90 MV/m obtained using multivariate optimizer and analytical computation using K-J Kim's emittance formulation. Bunch charge was 10 pC at 0 MTE.

gradient and the pancake beam regime as visualized by the obtained heatmaps.

$$\varepsilon_{sc} = \frac{Q}{\sqrt{E}} \frac{\sigma_z}{\sigma_x^{\frac{3}{2}}} \tag{2.15}$$

The results of the data are further confirmed when the $\sigma_x$ and $\sigma_z$ produced at the end of the ACT gun simulations were used in Eqs.2.9 and Eq.2.10 and the resulting emittance, mapped in $\sigma_z$ and $\sigma_x$ parameter space, was directly compared to K-J Kim's formalism where the total emittance is calculated as $\varepsilon = \sqrt{\varepsilon_{sc}^2 + \varepsilon_{rf}^2}$. The comparison results at 30 and 90 MV/m are presented in Fig.2.7, both at 10 pC and 0 MTE. Analytical method produces similar heatmaps clarifying the nature of the computational results plotted in Figs.2.2-2.6. The main differences between the plots can be attributed to the dynamic change in the bunch dimensions as it travels along the injector. K-J Kim's formalism uses the physical dimensions of the bunch, not the laser parameters, i.e. pulse length and spot size. Therefore, the boundaries of the K-J Kim's plots had to be approximated using typical values of bunch dimensions that were acquired at the exit plane of the injector.

### 2.6 Conclusion

Multivariate optimization of a quarter wave high gradient injector highlights fundamental relationships between the gradient and spatio-temporal bunch profile. Analytical treatment of the problem using classical emittance formulation and two-dimensional space charge model was able to capture the basic link between the bunch form factor and the injector gradient hence granting further insights to predict optimal parameters which can then be used to inform design decisions for injectors and laser systems. Future injector design can thus benefit from the presented parametrization that enables general understanding of the fundamental trade-offs. For instance, high brightness, high charge, and small energy spread cannot conveniently co-exist, but by designing the injector for a preferred application it can help negate interactions between those processes. By choosing the desired application (single shot microscopy with high charge versus spectroscopy with small energy spread) and then utilizing those requirements to influence injector design it can allow for minimizing complexity of the beamline optical element lattice.

### 2.7 Acknowledgments

The work by Benjamin Sims was supported by the U.S. Department of Energy Office of Science, High Energy Physics under Cooperative Agreement Award No. DE-SC0018362. The work by Sergey Baryshev was supported by the U.S. Department of Energy, Office of Science, Office of High Energy Physics under Award No. DE-SC0020429. We are grateful to Dr. John Lewellen for his insightful discussions, helpful advice, and ingenious sequencer.

# CHAPTER 3

# THERMAL EMITTANCE ISOLATION BY CATHODE RETRACTION

This chapter is based on a paper of the author under review: **B. Sims**, J. W. Lewellen, X. Ting, and S. V. Baryshev, "Thermal Emittance Isolation by Cathode Retraction", *arXiv* 2409.03499 (2024), https://arxiv.org/abs/2409.03499

In this chapter, a combination of cathode retraction and two-slit emittance measurement technique is proposed as an advanced means to individually modify emittance growth components, specifically, rf injector fringe fields, to isolate and directly measure the thermal emittance, the fundamental beam emittance metric for an electron beam. A case study of the LCLS-II-HE Low Emittance Injector (LEI), a state-of-the-art superconducting radiofrequency (SRF) gun, designed for LCLS-II HE upgrade is used to showcase the power of the two-slit technique. Particularly, it is demonstrated that generating a high resolution phase-space distribution map, dominated by the intrinsic emittance of the electron bunch, is possible. This result goes beyond the normal single-parameter distribution characterizations (e.g. RMS emittance and Twiss parameters) provided by the solenoid scan.

One key feature making this technique work (and in the end practically useful) is the ability to retract the cathode, because it provides the ability to compensate for radiofrequency (rf) defocusing. It is demonstrated how the cathode retraction can serve as an additional optimisation tool for tailoring the routine performance of the photoinjector. We posit that a variable position cathode may be a useful method for optimizing photoinjector performance across multiple parameters regimes.

## 3.1 Introduction

Superconducting radiofrequency (SRF) injectors are emerging as powerful sources for applications requiring high-average-current and high-brightness electron beams. Use cases include tools of scientific discovery (e.g. as beam sources for ultrafast electron diffraction and microscopy systems, and X-ray free electron laser injectors), as well as medical and industrial applications requiring high duty factors and average beam power [14–17]. While several metrics, such as beam brightness, have been established to characterize the quality of electron beams used for scientific applications, a parameter termed emittance is a central figure of merit for many applications. Roughly analogous to the M-squared figure-of-merit used for laser beams, the transverse emittance of an electron beam provides a characterization of the transverse phase-space density of the beam. An ideal electron beam would have an emittance limited by the Fermi exclusion principle. In practice, the emittance of a beam is determined by a number of factors, including contributions from space charge forces within the beam, nonlinear radiofrequency (rf) and static electromagnetic fields with which the beam interacts, and intrinsic emittance arising from the conditions during the beam's initial emission from a solid-state cathode [40].

Because in legacy systems beam emittance growth has been dominated by the space charge and nonlinear fields, efficient methods have been found to manage and minimize (or compensate) them [41]. Current beam source designs are approaching the point where intrinsic emittance can become a limiting factor in beam quality. Since the intrinsic emittance depends on the cathode material used, it needs to be measured experimentally as a benchmark of the emittance floor, i.e. setting the best attainable case. Techniques and apparatus such as the momentatron [42] have been developed to do this under "laboratory" conditions. However, experimentally measuring the intrinsic emittance in an operational beam source can be difficult due to the contributions from space charge and nonlinear external fields [43]. Given the relatively fragile nature of high-quantum-efficiency photocathodes, the ability to characterize in detail the evolution of cathode performance over time in an operational setting is increasingly essential.

The solenoid scan technique [44–46] has been a workhorse for measuring emittance because solenoid scans are fast, most if not all of the equipment is already present in most high-brightness photoinjector beamlines, and the technique itself is straightforward to implement. However, measuring emittance using solenoids has limitations associated with aberrations inherent to the solenoidal field [47], overlapping between rf and solenoidal fields [48], and fitting the produced data due to lack of symmetry from space charge and intrinsic emittance sources [44]; typically leading to potentially significant emittance overestimation [43]. As usually implemented, solenoid scans provide only a single *cumulative* (or whole-bunch) emittance measurement, i.e. without providing information about the detailed transverse phase-space distribution [49]. To extract RMS (whole-beam) parameters, additional assumptions may be required as the solenoid scan technique alters the impact of space charge during the measurement process, most apparently when the beam is focused to a waist, giving rise to uncertainties when estimating the beam parameters [44]. For very low emittance beams, the resolution of the beam imaging system employed may also prove to be a limiting factor. These limitations do not make solenoid methods invalid but instead indicate a measurement technique prone to overestimation. This may be problematic for measuring low intrinsic emittance and MTE values as is relevant for the application of this case study. Potential overestimation is only one factor when crossing a measurement setup involving a two-slit method, the other more relevant reason is the density phase space map exclusively enabled by two-slit methods.

A density map of the beam's transverse phase space would be a preferable measurement as it could contain important details about individual emittance contributions, as well as cathode emission characteristics, that could lead to better informed injector R&D and performance tuning. Tomographic techniques [50–52] have been used to develop phase-space maps, but these techniques have generally been applied at higher beam energies, such that beam has evolved significantly since its initial formation. While the starting phase-space distribution can be attributed to the cathode properties (e.g. intrinsic emittance and quantum efficiency) convolved with the drive laser, emittance growth over time can be attributed to space charge, acceleration and propagation through nonlinear fields, etc. Tomographic measurements performed at the photoinjector using a solenoid are also still subject to the effects mentioned above.

In this context, an arguably better way to measure the intrinsic emittance immediately after a low energy ($<$10 MeV) high brightness photoinjector is by using the two-slit technique [44, 53]. Given the phase space maps can be directly obtained, it opens up an opportunity to quantify additional lingering effects of space charge and rf emittance components that can be additionally manipulated by an effective and practical means such as cathode retraction with respect to the injector back wall

[54]. As the goal is to measure the intrinsic emittance, ideally to obtain a two-dimensional phase-space density map rather than a single RMS value, a slit method is preferable as long as it can provide the required resolution within a feasible measurement time. Contrary to the rapid solenoid scan, two-slit measurement comes at a cost in terms of time, where the duration of the measurement and errors resulting from drifts and jitter are major, and coupled, liming factors [55]. Indeed, reducing the intrinsic measurement error requires higher resolution scans that, consequently, increase the duration of the scan. Results from such long duration scans could be subject to system drifts or instabilities like a limited lifetime of high quantum efficiency (QE) photocathodes. Nevertheless, the detailed phase-space distribution provides a substantially improved ability to identify unexpected behaviors via direct inspection of the phase-space distribution, in addition to providing the ability to calculate the emittance from the measured distribution. Therefore, finding optimal ways to perform two-slit measurements deserves further efforts.

In the present work, using an example of the low emittance SRF injector being developed for LCLS-II HE upgrade [14], we computationally demonstrate a novel approach to intrinsic emittance measurement that utilizes $i$) cathode retraction to compensate for rf-induced emittance growth, and $ii$) a two-slit emittance measurement system to obtain a phase-space map. Practically speaking, the proposed diagnostic two-slit beamline could serve to characterize high brightness bunches and provide a means to characterize high-brightness photocathodes in an operating photoinjector.

## 3.2 Definitions of Emittance and Error

### 3.2.1 Two Slit Emittance Measurement

A two-slit emittance measurement works by measuring the intensity of "bunchlets," located at position $x$ and angle $x'$ with widths $\delta x$ and $\delta x'$ respectively within the beam bunch; the ensemble of measurements form a current density map of the transverse phase space $\rho(x, x')$. (Strictly, we are measuring a projection of the full 6-d phase space distribution of the bunch $\rho(x, x', y, y', p, t)$, onto a single plane.) The apparatus consists of two plates with transverse slits (simply referred to as "slits" hereafter) located along the axis of beam propagation. A detector is located downstream of the second slit; the detector can be an optical screen, a Faraday cup, etc. The slit plates are made thick enough to absorb beam particles not entering the slit, but thin enough so as not to significantly collimate the beam.

The transverse position of the first, or upstream, slit $X_1$ sets the position of the bunchlet center, that is $x$=$X_1$, and the difference in the center positions of the upstream and downstream slits, $X_1$ and $X_2$ respectively, divided by the distance between the slits, $L$, determines the angle $x'$ as [56, 57]

$$x' = \frac{X_2 - X_1}{L} \tag{3.1}$$

The number of transmitted beam particles at each pair of slit locations $X_1$ and $X_2$ (or the corresponding location in the beam's phase space $x$ and $x'$) describes a data bin. These bins can be combined together into a density map representing the bunch phase space $\rho(x, x')$. The resolution of the phase space map is determined by the slit widths ($W_1$ and $W_2$) and longitudinal separation of the slits $L$ as

$$\Delta x = W_1 \tag{3.2}$$

$$\Delta x' = \frac{W_2}{L} \tag{3.3}$$

This indicates that small slits and large separation $L$ between slits will provide higher resolution, e.g. more bins across a given phase-space distribution. The bin size is analogous to pixel size in a conventional imaging system.

Two-slit measurements of the intrinsic emittance require the management of space charge and rf induced emittance growth, such that the emittance of the beam is dominated by the intrinsic emittance. Space charge-induced growth can be minimized by using low-intensity laser pulses, i.e., by conducting measurements at low bunch charge. Additionally, by sweeping laser parameters, specifically the intensity, we can assess the impact of space charge, effectively characterizing its contribution to the overall emittance.

The intrinsic emittance can be increased by increasing the primary laser spot size, making the intrinsic emittance easier to measure. This, however, is not without a cost as the increase in radius also increases the emittance contribution from nonlinear fields, as well as (all other effects equal) increasing the size of the beam spot at the first slit. This effect can be addressed with the use of cathode retraction. By retracting the cathode, a transverse focusing field near the cathode is introduced by the aperture edges. Such lensing effects help mitigate the rf defocusing of the beam as it exits the rf gun, allowing for the use of a larger laser spot on the cathode. There should exist an optimal location where focusing provided by cathode retraction and rf defocusing effects from the rf field, in the body and at the exit of the gun, effectively cancel each other, providing a net minimization of beam divergence due to rf effects. Hence, rf divergence is minimized. This approach also results in a smaller spot at the first slit, with a smaller far-field divergence angle, which is beneficial for the two-slit method. We note that while a solenoid located immediately downstream of the gun cavity, e.g. in the typical location for emittance compensation, can provide a small beam at the first slit, it cannot provide the same benefits in terms of minimizing nonlinear field contributions as the method of cathode retraction can.

### 3.2.2 Binning Error

*Edge bins*, those located near the edges of the beam in phase-space, represent a source of error similar to that encountered in particle-in-cell space-charge calculations. All particles within a bin are typically assigned to a single $(x, x')$ determined by the slit locations. For reasonable bin sizes, bins with many particles, and beams with relatively slow variations across the phase-space distribution, binning is a reasonable approach for phase-space mapping. However, edge bins near the boundaries of the distribution may collect a relatively small number of particles (or even none in low bunch charge case), and the center of the bin may not correspond well to the actual average position of the particles within the bin. Thus, the error of the two-slit measurement can be directly correlated to the number of edge bins as [58] where the error is proportional to both the resolution and the maximum $x$ and $x'$ measured. The result of the difference between these two values, as seen in Eq.3.6, is the approximate emittance without the error attributable to binning effects.

$$\varepsilon_{er} = \frac{n_{edge} \cdot \Delta x \cdot \Delta x'}{2 \cdot \pi}. \tag{3.4}$$

The emittance measured by any two-slit scan can be approximated by [58]

$$\varepsilon = \frac{n \cdot \Delta x \cdot \Delta x'}{\pi}. \tag{3.5}$$

When combined with additional metric for calculating the error in the measured emittance, it yields

$$\varepsilon_{er} = \frac{2}{\pi} \cdot (x_{max} \cdot \Delta x' - x'_{max} \cdot \Delta x), \tag{3.6}$$

The set of the given equations establishes the basis for the informed design of experimental beamline where slit-based phase space measurements with minimized error.

### 3.2.3 Basic Emittance Concepts

Projected transverse emittance can be calculated using either velocity or momentum phase space. As many of the phase spaces measured are non-elliptical, momentum space was chosen to help account for any irregularities that would be overlooked in the velocity space [37]. The conversion from the measured velocity space to momentum space is done by multiplying the measured $x'$ by the Lorentz $\gamma$-factor of the particle. The statistical root mean square (RMS) and 100% of the particles were used for emittance calculation as

$$S_{11} = \overline{x \cdot x}, \tag{3.7}$$

$$S_{12} = \overline{x \cdot x'}, \tag{3.8}$$

$$S_{22} = \overline{x' \cdot x'}, \tag{3.9}$$

$$\varepsilon = \sqrt{S_{11} \cdot S_{22} - S_{12}^2}. \tag{3.10}$$

The unnormalized emittance (scales with the beam's $\gamma$-factor) versus the normalized emittance (e.g. nominally invariant under acceleration) were used, as it allows for direct comparison between the calculated emittance and that expected given the parameters of the cathode.

### 3.2.4 Intrinsic Emittance and MTE

The intrinsic emittance of a bunch is determined by the initial spot size of the bunch and the mean transverse energy (MTE) of electrons emitted from the cathode. The MTE is determined by several factors including the photocathode material and illumination wavelength, temperature, and surface roughness. In the presented simulations, the cathode MTE is chosen in accordance with the requirements of the LCLS-II-HE low-emittance injector [35]. The intrinsic emittance of the beam can be calculated as:

$$\varepsilon_{int} = \sigma_{xi}\sqrt{\frac{2 \cdot MTE}{m_e c^2}}, \tag{3.11}$$

$$\sigma_{xi} = \frac{R_i}{2}, \tag{3.12}$$

$$\varepsilon_{int} = \frac{R_i}{2}\sqrt{\frac{2 \cdot MTE}{m_e c^2}}, \tag{3.13}$$

$$MTE = \frac{m_e \cdot c^2}{2} \cdot \left(\frac{2 \cdot \varepsilon_{int}}{R_i}\right)^2, \tag{3.14}$$

where, assuming a uniform emission current density, $R_i$ is the emission spot radius. These equations allow for the calculation of the expected intrinsic emittance for a given MTE and emission spot radius, and thus the contribution of the MTE to the total emittance and therefore can be compared against the simulated slit measurement.

## 3.3 Case Study: Low Emittance Injector for LCLS-II-HE upgrade

### 3.3.1 Case study setup

The LCLS-II-HE low emittance injector (LEI) is a state-of-the-art high-gradient SRF injector system operating near 185 MHz [35]. The LEI is intended to enable extending the LCLS-II-HE's useful photon energy to 20 keV without additional cryomodules (e.g. increasing the beam energy past the LCLS-II-HE goal of 8 GeV) [35] by providing a significantly lower-emittance beam at 100 MeV, than the current LCLS-II injector. The LEI begins with a 1.8-MeV SRF photoinjector, being developed by a collaboration between SLAC, MSU/FRIB, Argonne, and HZDR. Low emittance bunch production necessitates this case study focusing on setting a useful and versatile photocathode testing beamline for the LEI. A robust two-slit emittance measurement optimized for the LEI SRF gun was considered. Requirements for any such system under consideration include compatibility and integrability with the current LEI gun-to-linac beamline design, and the ability to measure photocathode MTEs below 200 meV (e.g. suitable for cathodes proposed for the LEI ) [35]. *In situ* measurement of photocathode MTE, and the evolution thereof, would then help attain the best

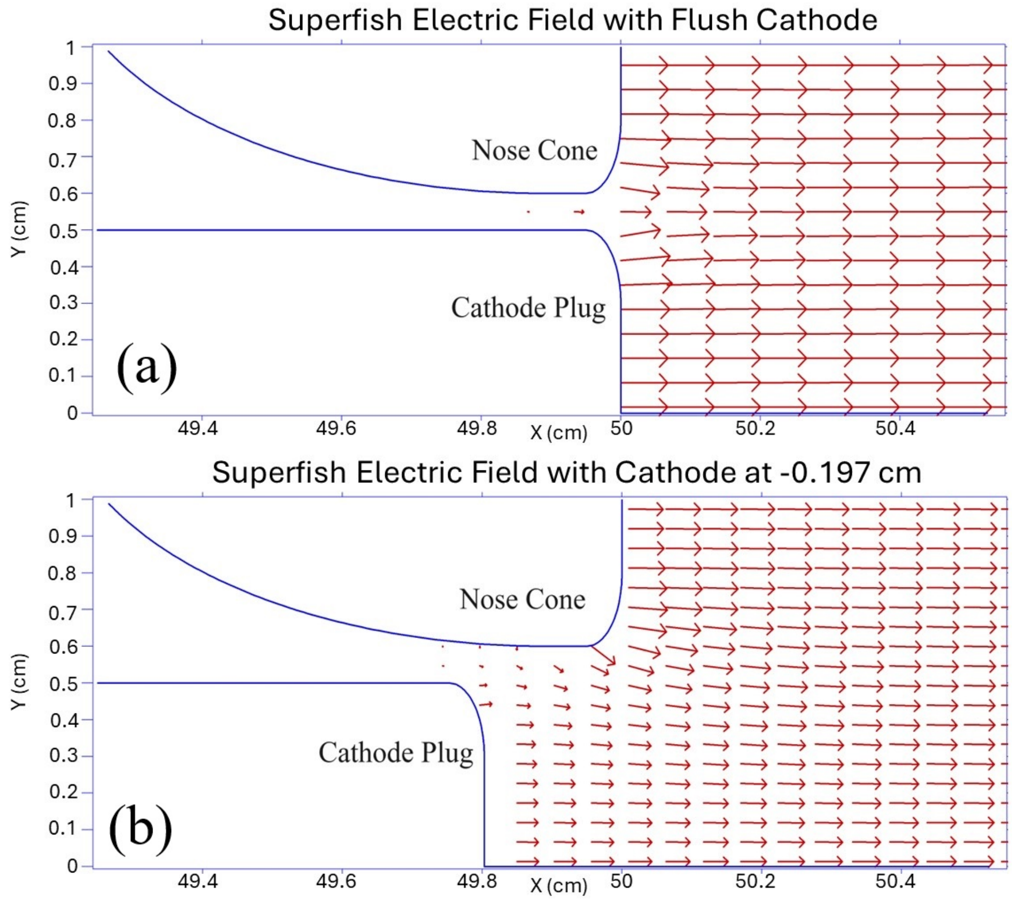


Figure 3.1 Superfish model of the LEI SRF gun with the cathode retracted (a) 0 cm, or flush with the nosecone face (the nominal operating position) and (b) retracted by -0.2 cm.

overall performance of the LEI. The design of the SRF gun allows for manipulation of the cathode stalk, in particular, variation of the longitudinal position of the cathode surface relative to the gun "nosecone" surface [35]. Utilization of this feature is key to the MTE measurement process, as proposed here: the cathode-region fields, as modified by shifting the cathode longitudinal position, enable a low-error measurement.

The work was performed utilizing Superfish [59], General Particle Tracer (GPT) [60], and a proprietary sequencer. Superfish was used to generate rf field maps of the LEI SRF gun with the cathode surface located at different longitudinal positions. Several examples can be seen in Fig.3.1. The field maps were imported into GPT to simulate, visualize and quantify the two slit measurement. The sequencer was used to automate the transition from Superfish to GPT and for quantifiable data collection and post-processing. The solenoid designed for the LEI was not used

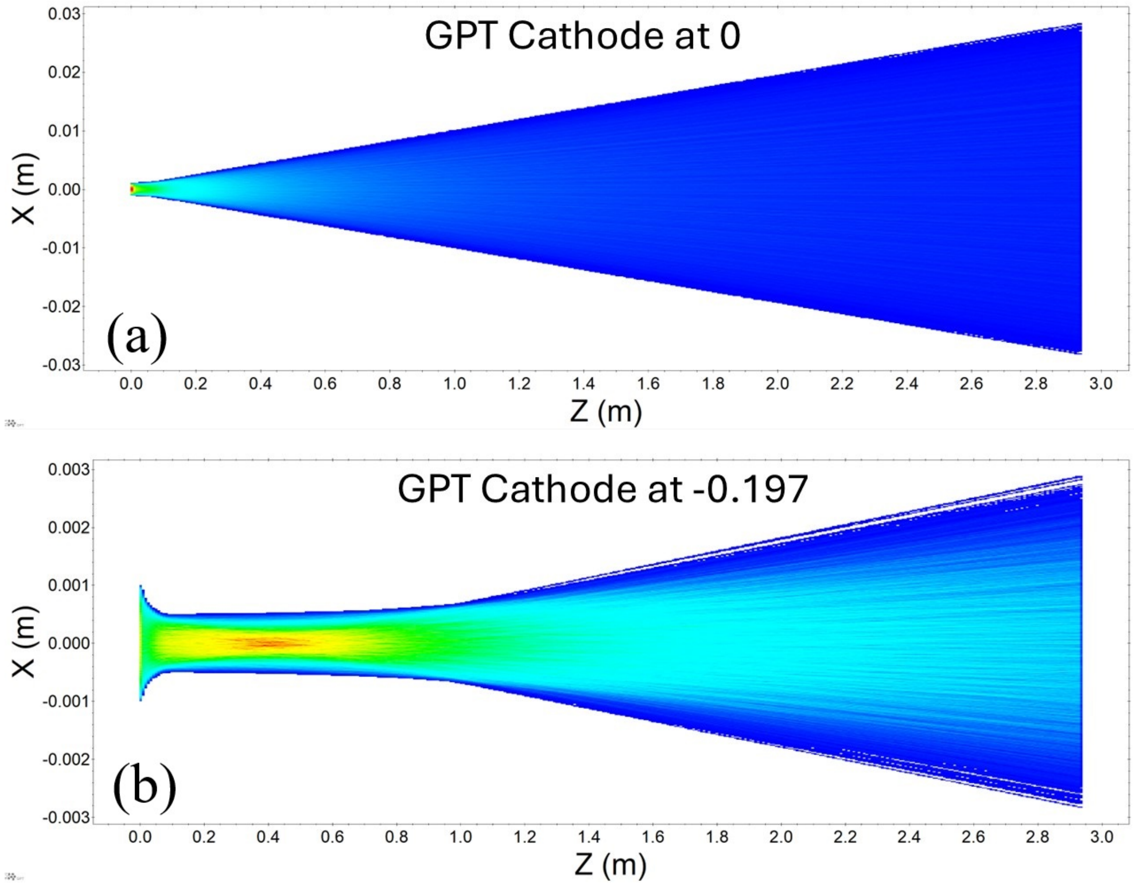


Figure 3.2 (a)GPT simulation with LEI cathode flush at 0 cm producing a large final bunch radius of 30 mm ; (b) GPT simulation with LEI cathode retracted to –0.197 cm producing a much smaller bunch radius of 3 mm, at $z$ = 3m.

for any of the presented simulations and results.

### 3.3.2 Cathode retraction

Under nominal operating conditions for the LEI (e.g. 100-pC bunch charge), the SRF gun cathode is flush with the gun's nosecone surface. This configuration produces a diverging beam, which is compensated by the gun solenoid as part of the traditional emittance-compensation process. However, for the proposed measurement technique to compensate for the divergence of the bunch, cathode retraction is used along with reduced-charge bunches. The unique construction of the LEI injector allows for movement of the cathode in the z-direction via an advanced cathode stalk design [61]. Further manipulations in the x- and y-directions can be performed to limit non ideal fields created via cathode retraction off-center misalignment [35].

The reduction in beam diameter caused by cathode retraction is also relevant to the measurement technique. As seen in, Fig.3.2, there is an approximately 10x difference in the final spot size of the bunch. This is of particular note as it reduces the spot size at each slit, requiring smaller shifts to maintain the desired number of bins. Performing a case study over this range with fixed slit sizes would be problematic due to the low number of bins activated at the smaller bunch diameters. Instead, this case study was conducted with the cathode being retracted from –0.15 cm to –0.22 cm with respect to its flush (0 cm retraction) reference position, Fig. 3.3. In this range, a minima was identified where the smallest bunch transverse size was observed on a screen located 1 m downstream from the injector exit plane; we define the corresponding cathode location as the optimal cathode retraction for intrinsic emittance measurement. The variation in spot size with cathode position is due to the emergence of the radial focusing fields that can be seen in Fig. 3.1. In accord with Eq. 3.6, the minimum spot size, corresponding to retraction of –0.197 mm is a desirable condition for measuring the intrinsic beam emittance because systemic error can be minimized. Fig. 3.4 contrasts two bunch transverse phase spaces corresponding to a cathode retraction of zero and the optimal position for intrinsic emittance measurement. A bunch emitted with the cathode in its nominal (flush) location is strongly diverging, with a "narrow" phase space as shown in Fig.3.4a. Attempting to measure this distribution produces a larger error in accordance with Eqs.3.6 and 3.4 as it has a large $x$ and $x'$ spread in addition to a high number of edge bins.

Alternately when the cathode is retracted the phase space at the screen is quite different, Fig.3.4. Retracting the cathode has two benefits when measuring MTE. First, it is seen that the extent of the phase space with the cathode at –0.197 cm is about an order of magnitude smaller in both $x$ and $x'$ than with the cathode in the nominal position. While the actual phase-space area in both cases is nominally the same, the potential measurement resolution is better and the number of edge bins is smaller, allowing for more accurate measurements. Second, the dominant factor in the bunch's transverse phase space is no longer the radial defocusing term from the gun's rf field. Instead, the divergence is dominated by the MTE with vanishing contribution from the rf fields. Note that, while we describe the beam location as at a "focus," e.g. smallest obtainable spot size, as a matter

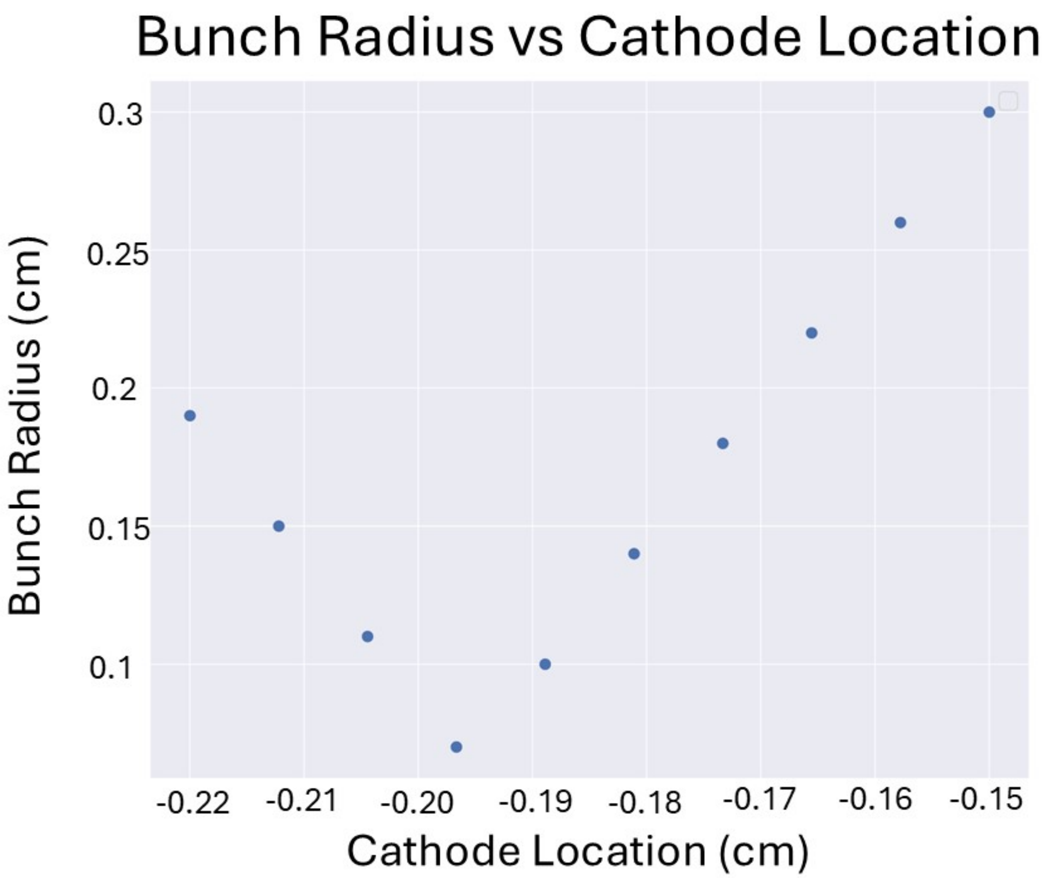


Figure 3.3 Simulated RMS bunch radius at 1 m for various cathode positions from the nominal cathode position (flush with nosecone).

of convenience, the beam is not in fact at a waist but is diverging. Thus, it meets one of the criteria for the two-slit measurement technique, e.g. that the location of the first slit is downstream of a beam waist.

Cathode retraction does have limitations which must be kept in mind, particularly the frequency detune and electric field reduction. The simulated cavity (using SUPERFISH) was able to give specific answers for both of these limitations. It was found that at the maximal retraction shown here (-0.22 cm) the frequency increased by 1.7 kHz, which is well within the tuning range of the LEI (60 kHz). With cathode retraction, the on-axis electric field it was found to decrease by ~40%.This would be a problem when used with 100 pC of charge extracted from the cathode because space charge forces would blow up the bunches. This is however not a limiting factor to the

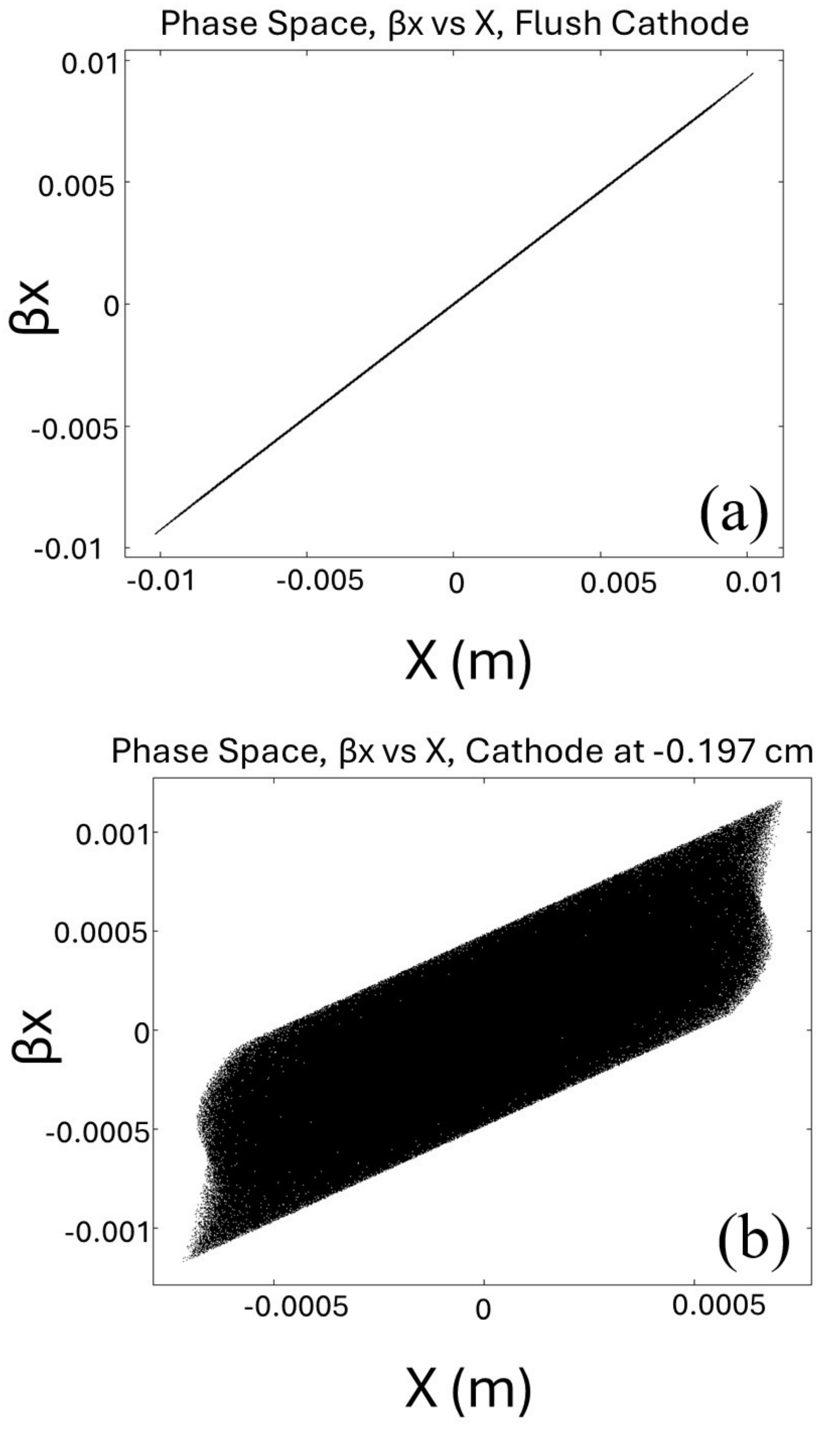


Figure 3.4 Bunch phase space with (a) cathode in the nominal position (e.g. no retraction, flush with nosecone) and (b) cathode retracted to –0.197 cm.

proposed setup utilizing 1 pC charge [40, 62]. Individual field maps were created for each cathode location ensuring that the effect of the diminishing normal rf field component was accounted for in simulations.

### 3.3.3 GPT beamline modeling

GPT simulations were performed with slits located at $z$=1 m and $z$=2 m, for a separation $L$=1 m. This setup (Fig. 3.5) is sufficient to allow the beamlet passed by the first slit, to diverge appropriately. The largest spot size at each screen determined slit widths for all simulations as the parameters were, in analogy to a physical measurement with fixed-width slits, not modified over the course of the simulated measurement. The up- and down-stream slits were sized as $W_1$=99 $\mu$m and $W_2$=198 $\mu$m respectively, to provide 101 bins across the beam spot at both longitudinal locations. This was done to accommodate the spot size produced with the cathode retracted to –0.15cm resulting in a spot size at $z$=1 m of 0.5 cm and the spot size at $z$=2 m of 1 cm. As the bunch is larger at the second screen, a larger slit size is needed to fully map it in the same number of steps as at the first slit location. In an experimental setting, such slits can be readily fabricated. With a nominal beam energy of 1.8 MeV, if made of tungsten the slits would need to be at least 1mm thick to completely stop the beam. The angular acceptance of the first slit would therefore be approximately atan(0.1 mm / 1 mm) = 5.7 deg, and approximately 11.3 deg. for the second slit. The angular resolution provided by the second slit is (0.2 mm / 1 m) = 0.01 deg; and the anticipated divergence of the beam as a whole, when the cathode is in the retracted location, is on the order of 1 deg. Thus, we would not expect the angular resolution of the measurement to be limited by the upstream slit acting as a collimator.

In GPT, the bunch was generated as a uniform spot with a radius of 1 mm and a Gaussian temporal profile with a $\sigma$ of 5.67 ps, clipped at $\pm 3\sigma$. This pulse length is the operating pulse length for the LEI and was used to limit the number of changes necessary to operate the theoretical system. While a shorter pulse length would offer a reduction in the RF emittance due to the reduction in the range of degrees experienced by the bunch, it would also severely limit the ability to increase the charge of the bunch. These simulations were performed assuming no space charge interactions due

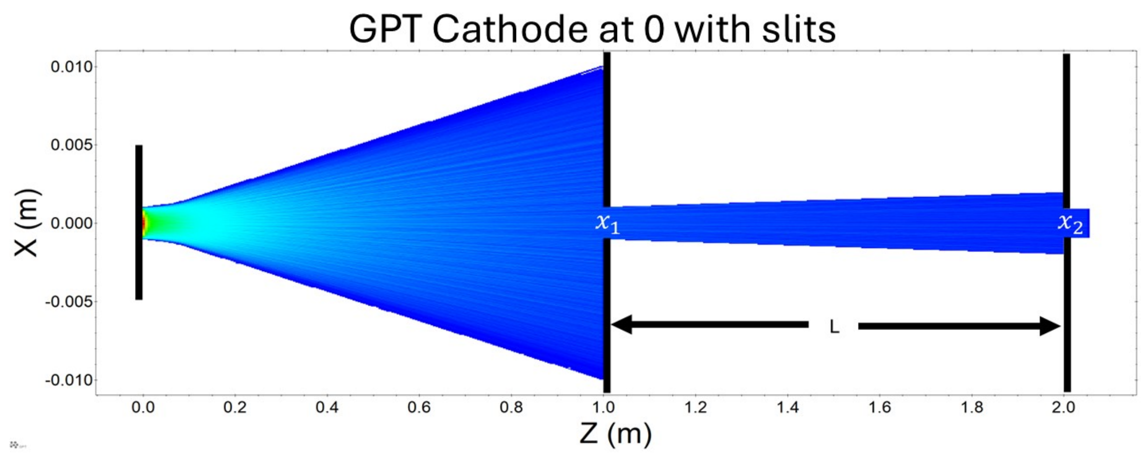


Figure 3.5 GPT simulation illustrating the effect of two exaggerated slits when the standard position is used, i.e. when the cathode is flush with the gun's nosecone.

to low charge. Achieving sufficient charge to be measurable on a Faraday cup would be required in an experimental setup. Thus the operating pulse length was used as it can accommodate charge better than a short pulse (100 fs). The MTE was set to 200 meV. Space-charge calculations were not included in the simulation, as a low-intensity laser pulse yielding a bunch charge at the cathode of 1 pC would have negligible space charge contributions to the emittance, while providing sufficient charge to be captured by a Faraday cup-like device [63, 64], but space-charge calculation would significantly increase the time required to perform the simulations. Particles transmitted through both slits were counted at each pair of slit locations. This process was repeated for 10 different cathode retracted positions, between –0.15 cm to –0.22 cm, as seen in Fig. 3.3.

Both the cathode-region focusing and exit-region defocusing are manifestations of the same phenomenon, e.g. a spatially varying longitudinal field gives rise to radial fields. A longitudinal field increasing in magnitude (as in the case in the near-cathode region when the cathode is retracted) gives rise to a radially focusing field; while a longitudinal field decreasing in magnitude (as is the case along the majority of the axis within the gun) leads to a radially defocusing field [65].

For the same emission radius and launch phase, the retracted cathode produces a much smaller bunch radius of 3 mm, as compared to the un-retracted simulation with a bunch radius of 30 mm, both at $z$= 3 m. The retracted cathode simulation generates a beam waist approximately 0.4 m downstream from the cathode. In contrast, with the cathode at its nominal position, there is a virtual beam waist several cm upstream of the cathode, and the far-field divergence angle is approximately an order of magnitude larger. The somewhat peculiar shape of the bunch's edge in phase space is attributed to nonlinear components in the near-cathode radial rf fields; but the overall divergence is dominated by the intrinsic emittance of the beam, not the rf fields (regardless of linearity). The cathode retraction thus provides a phase space distribution that can be more accurately measured by a two-slit scan to yield an MTE.

The difference in the number of edge bins between distributions from an ideally retracted vs. partly retracted cathode is drastic, as illustrated in Figs.3.6 and 3.7. There is an approximately 3-fold difference in the number of edge bins indicating a similar drop in the measurement error. (We note that when the cathode is flush, the resulting strongly diverging distribution is effectively all contained in the edge bins.) Together these effects – fewer edge bins, and smaller extents in phase space – allow for a measurement of the intrinsic emittance with lower systematic error.

### 3.4 Discussion

The results of the case study show that the minimal *measured* emittance was found with the cathode retracted to –0.197cm, Fig. 3.8. At this location, emittance was calculated as 0.475 $\mu$rad, corresponding to an MTE of 230 meV, 30 meV higher than would be expected solely from the cathode intrinsic emittance as marked by the black line in Fig. 3.8. This suggests the cathode retraction method can provide a reasonable measure of cathode MTE when the cathode is installed in an operational high-brightness photoinjector. However, the measurement error of +15% is still substantial. When the resulting phase space analysis is performed using the resolution-based emittance with consideration of the binning error as discussed above, in Fig. 3.10 there is nearly perfect agreement between the RMS emittance and the resolution based emittance when the binning error is subtracted. The calculation of the binning error also indicates that it is lowest at –0.197 cm due to the size of the bunch in phase space. Comparisons between Fig. 3.4 and Fig. 3.9, particle-based phase space and bin-based phase space respectively, show excellent agreement between the two, while tracking individual particles in GPT provides a more precise map of the phase space but is not feasible in a practical experimental system.

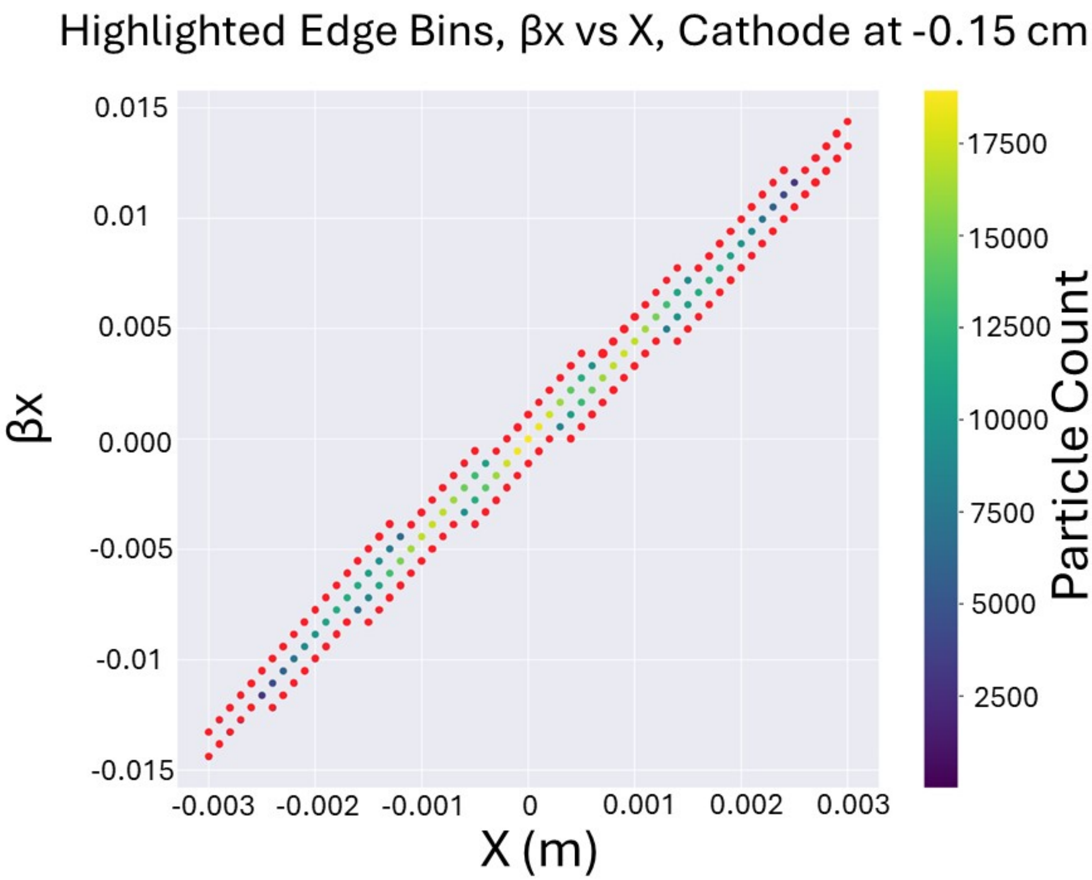


Figure 3.6 Edge bins of two-slit simulation with cathode at –0.15 cm are marked in red. The total is 112 edge bins.

The results highlight two particularly useful intertwined insights for a practical measurement: cathode retraction can be used to generate a beam in which the divergence is dominated by the cathode MTE; this is the same foundation upon which the operation of instruments such as the Momentratron rely. This condition in turn, leads to a lower binning error in the two-slit measurement and, ultimately, to sub-20% measurement errors for measuring the cathode MTE. In terms of practical implementation and experimental setup, the optimal cathode location to make an intrinsic emittance measurement is found simply via minimizing the spot size of the beam at the first slit location. This provides a fast way to identify the optimal cathode position for the measurement. Second, by effectively compensating for rf defocusing within the remainder of the gun, cathode retraction allows the MTE to become the dominant term impacting the measurement process.

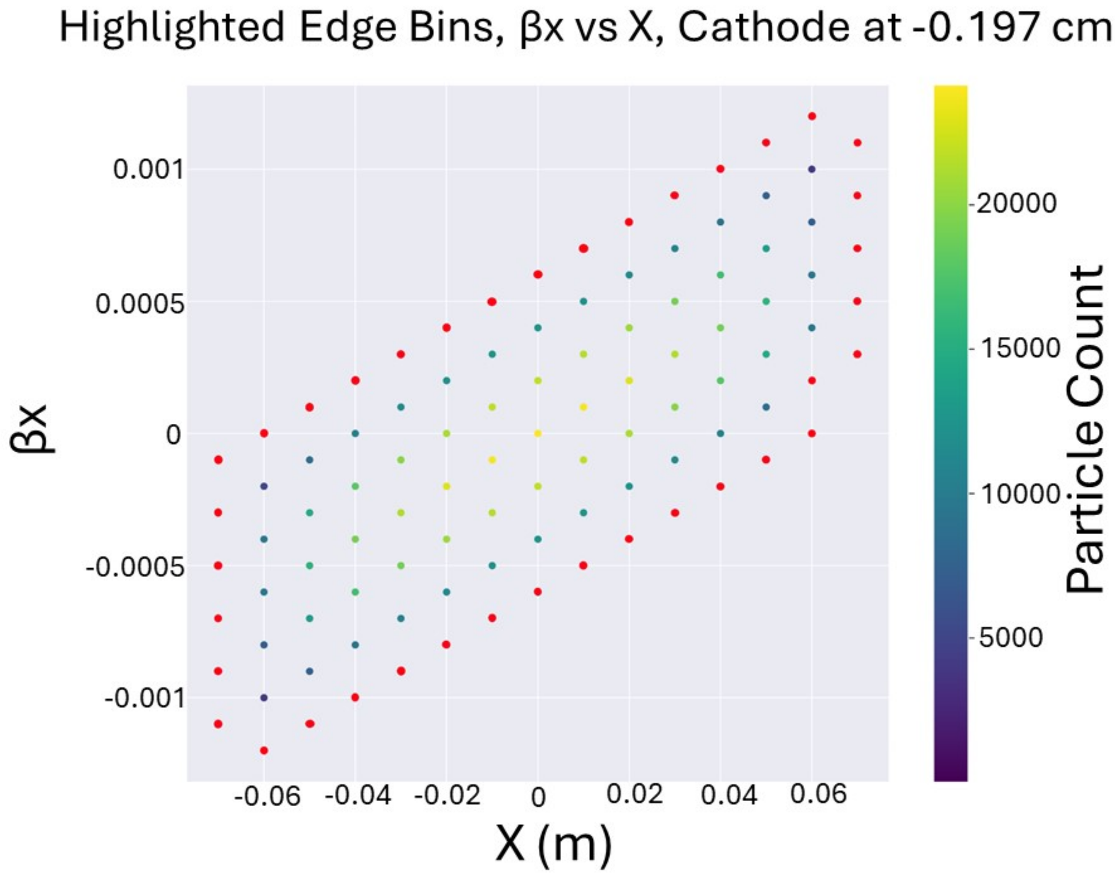


Figure 3.7 Edge bins of two-slit simulation with cathode at –0.197 cm are marked in red. The total count is 38 edge bins.

Together these effects are sufficient for measuring the MTE of the cathode within a reasonably small margin of error. Analysis of the systematic error contributions provides an understanding of why these effects decrease the measurement error. Indeed, calculating the resolution based emittance and binning error provides not only a useful double-check of an RMS emittance measurement but also explains why an emittance measurement will have a lower error with a smaller, more slowly diverging beam than one where the bunch is strongly diverging, e.g. due to rf fields. By analyzing the binning error equation, Eq. (3.6), we observe that bunches with larger extents in phase space, all else equal, will have larger measurement errors than bunches with the same phase-space area, but smaller extents in phase space. Understanding the error contribution that different phase space shapes will contribute provides a critical tool in determining the utility of a two-slit measurement.

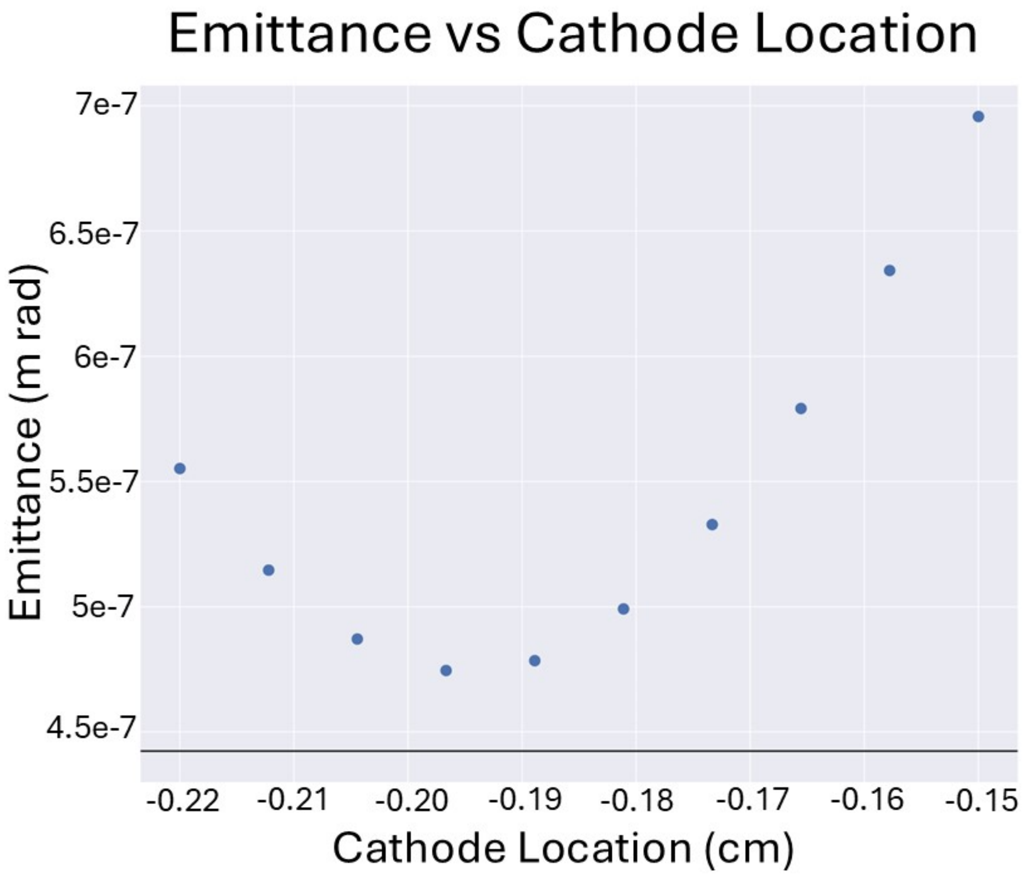


Figure 3.8 The simulated RMS emittance using the two-slit method for different cathode retraction locations.

### 3.5 Conclusion and Outlook

This work introduces an improved two-slit emittance measurement methodology that combines several techniques to measure the intrinsic emittance of a beam, and thus the MTE of the photocathode from which it was emitted. These techniques have been simulated to show their effectiveness at isolating intrinsic emittance. As is often the case the approach to simulating a system is different from using that system in practice. The limitations of a two-slit measurement can be broadly categorized as duration based and error based. The discussed case study provided ways to address both of these limitations so that a practical system can be proposed.

The duration limitation can be addressed in part by utilizing a simple approach to determine the preferred cathode position for an emittance measurement, as only the diameter of the beam needs to be measured to set the cathode position. This eliminates the need to make slit-scan measurements at

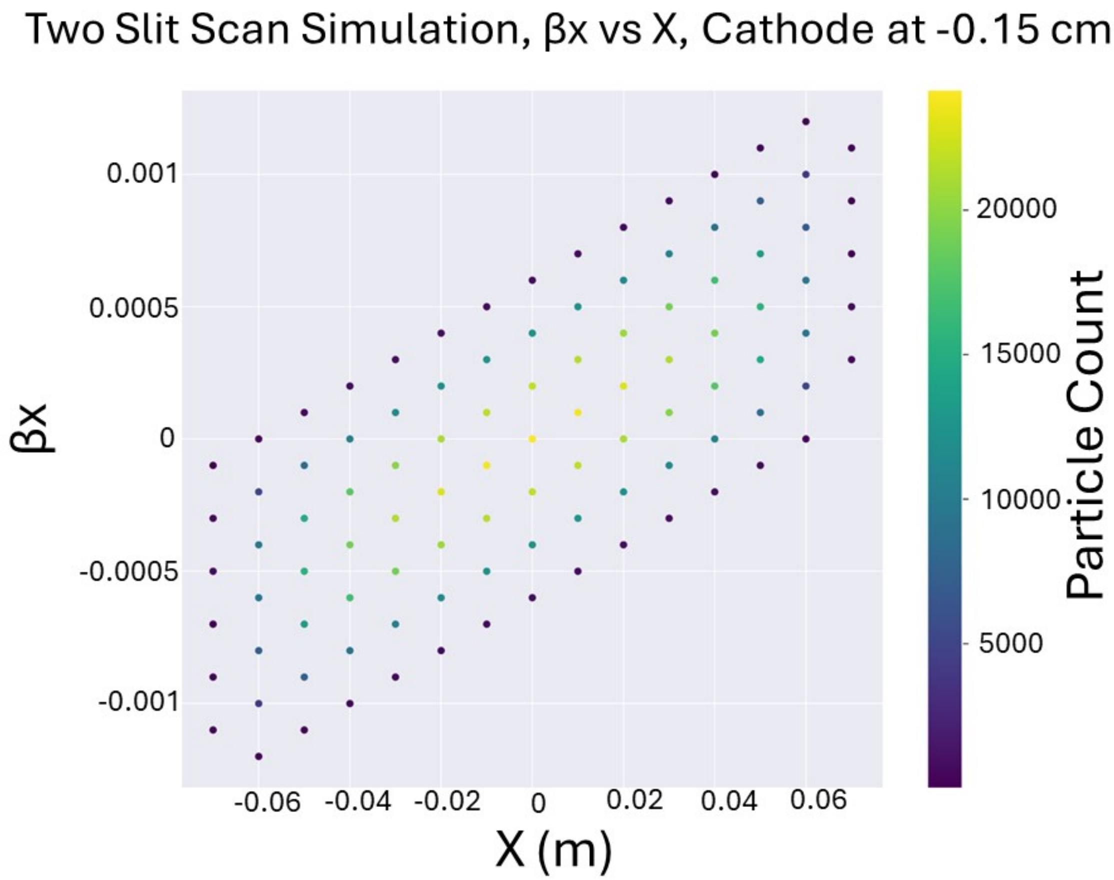


Figure 3.9 The simulated $x$-$x'$ phase space using the two slit method with the cathode positioned at –0.197 cm.

multiple cathode locations. Careful design of the slit system, e.g. determining the optimal number of bins, will help to minimize the time required to make a single scan while maintaining the desired resolution. While a thorough analysis of minimizing measurement time is beyond the scope of this paper, we note several possible directions. Increased bunch charge can decrease measurement time (e.g. accumulating the same statistics, in terms of charge per bin, etc., more quickly) albeit at the expense of increased space-charge contributions to the beam emittance; this can be explored further in simulation. Substituting fast beam steering (via magnetic or electrostatic deflectors) for physical slit motion [41, 57] could potentially significantly decrease the measurement time; the steering fields do not perturb the phase space and thus does not corrupt the measurement. Incorporation of intelligent algorithms into the measurement process, e.g. to identify likely regions of no current density, can reduce the number of total locations to be sampled in phase space.

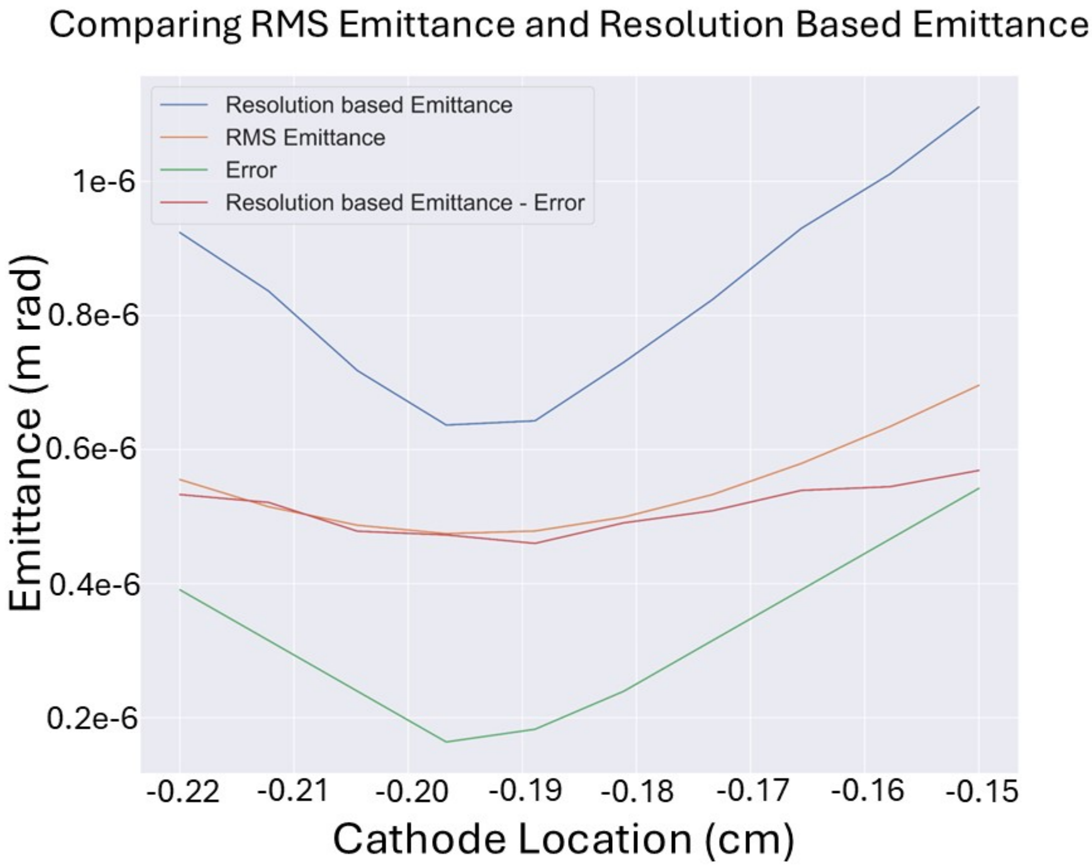


Figure 3.10 A comparison between the resolution based emittance and the simulated RMS emittance from the two-slit method at different cathode location.

The error limitation of two-slit measurements cannot be avoided as binning of the particles will occur based on the size of the slits used. However, as is shown here, it is possible to generate phase space distributions where the binning error is minimized and an RMS measurement of emittance is not strongly affected by the binning error. The phase space effects shown here are attributed to the dynamics at play from cathode retraction and work ideally for measuring the intrinsic emittance. In general, the resolution-based emittance and binning error estimates may provide useful corrections to the RMS emittance calculated from the measured phase-space map.

### 3.6 Acknowledgments


The work by Benjamin Sims was supported by the U.S. Department of Energy Office of Science, High Energy Physics under Cooperative Agreement Award No. DE-SC0018362. The work by

Sergey Baryshev was supported by the U.S. Department of Energy, Office of Science, Office of High Energy Physics under Award No. DE-SC0020429. The work was supported by the U.S. Department of Energy Office of Science, High Energy Physics under Cooperative Agreement Award No. DE-SC0018362, and the US Department of Energy under Contract DE-AC02-76SF00515.

# CHAPTER 4

## DUAL-MODE RF CAVITY: DESIGN, TUNING AND PERFORMANCE

This chapter is based on a paper of the author under review: **B. Sims**, D. Sims, S. V. Baryshev, and J. W. Lewellen "Dual-mode rf cavity: design, tuning and performance", *arXiv* 2410.00130 (2024), http://arxiv.org/abs/2410.00130

This chapter present the design and characterization of a dual-mode radiofrequency (rf) cavity, a novel electromagnetic structure with potential benefits such as compactness, efficiency, cost reduction and multifunctionality. The cavity was designed to balance the dual-mode structure considering several factors, such as mode frequencies, quality factor ($Q$-factor), and minimizing cross talk between couplers. We performed various tests to verify that this cavity performed as expected compared to simulated results. As exampled here, a combination of the fundamental mode $TM_{010}$ and the $TM_{011}$ mode, tuned to a harmonic of the fundamental, was realized to linearize the off-crest electric field, thereby enabling concurrent bunching and acceleration of charged particle (e.g. electrons) beam in high power systems. The reduction in the number of cavities required to bunch and accelerate promises cost and space savings over conventional approaches. This research lays the foundation for further exploration of multi-mode cavity applications and optimization for specific use cases, with potential implications for a wide range of fields including quantum information platforms.

### 4.1 Introduction

When boundary conditions are applied to a wave, electromagnetic wave or a particle, travelling in free space, eigen modes or states form. Selection and manipulation over such modes or states are the "control knobs" in laser and information technologies, microelectronics, gaseous and solid state chemistry and beyond. Cavities and waveguides are universally utilized tools for eigenmode control for information storage and transmission. Inherently, they can host/support many modes at once. This often is viewed negatively such as in a classical rectangular waveguide where 1/2 ratio of sidewall length is used to allow for one propagating $TE_{01}$ mode and avoiding crosstalk.

Multi-mode systems offer potential advantages of interest. In one example, when interacting with electrons in particular spin states, coexistence of many modes are extremely beneficial for information processing. It became a key subject in quantum computing and optics where superconducting radiofrequency (SRF) cavities, operated in the GHz range, are used to create and manipulate long lived quantum states [66–69]. There is also a specific use of copper and niobium (normal and superconducting) rf cavities in fundamental research such as electron-proton colliders (particle physics), X-ray free electron lasers (basic energy sciences) or specialty electron linacs for space exploration [70]. The use of multimode cavities here were proposed to improve compactness/reduce cost or enhance luminosity/brilliance leading to much higher signal to noise ratio when detecting novel particles or exotic processes [71, 72]. At the same time, multimode rf cavities (wherein mode frequencies are at simple integer or fractional ratios, and mode amplitude and phase are actively controlled) have been proposed [73–76] but generally have not been widely adopted.

Here, we present design of a dual-mode cavity that can simultaneously accelerate and shape electrons in linac systems, where amplitude and phase between the modes can be tuned with high precision. The demonstrated experimental feasibility of a dual-mode cavity has immediate translation to three-dimensional circuit QED architectures in which SRF cavities are being widely deployed as practical means for storing quantum states (transmon or photon) as they have millisecond to second scale coherence times [77, 78].

### 4.2 Use of multi-mode Cavities in acceleration systems

One important system to consider is the rf photo-injector (or rf gun) which, e.g., serves to generate high quality electron beams for high brilliance hard X-ray production at FELs and time-resolved microscopy. The brilliance is highest when the greatest charge can be contained in the smallest phase space volume. Ultimately, brilliance would be limited by the Fermi exclusion principle and the Heisenberg's uncertainty principle. In reality, the beam quality from an rf gun is constrained by multiple factors, including those associated with the electron beam itself, i.e. non-linear space charge forces within the beam; and factors associated with the design and performance of the gun's rf cavity, for instance the achievable electric field magnitude within the rf gun, and the sinusoidal time dependence of the fields that can distort the beam's phase space. To address challenges of this sort, specifically concerning improvement of the longitudinal phase space, a compelling idea of a double frequency rf cavity resonator was proposed [73, 74] where two modes, working cooperatively and tuned independently in amplitude and phase, couple to electrons in the beam to, e.g. linearize the longitudinal phase space. More generally multi-mode rf accelerator structures (including rf guns as well as structures intended to accelerate, but not generate, beams) have been explored in modeling and simulation, but very few have proceeded past that stage.

This paper presents the design and testing of a dual-mode $TM_{010}$/$TM_{011}$, S/C-band (2.81/5.62 GHz) cavity. It was designed to leverage recent advances in solid-state GaN amplifier technology, because the range 2-8 GHz is where major interest exists for all-solid-state, for compact accelerator technology. By using the second harmonic to linearize the time-dependence of the field experienced by a particle transiting the cavity, it can serve to both accelerate and chirp a beam for velocity-based bunch compression, while reducing or eliminating the intra-cavity beam energy droop typically associated with the operation of a standard "buncher" cavity.

### 4.2.1 Conventional Bunching

$TM_{010}$ cavities are commonly used for low-energy particle beam longitudinal compression. The phase of the $TM_{010}$ mode within a cavity is set so as to apply an energy chirp to a discrete bunch of particles (such as is generated by a photocathode and drive laser) transiting the cavity [79], or to energy modulate a continuous beam (such as generated by a thermioic cathode). For a discrete bunch, the cavity phase is set such that the beam exits the cavity with no net energy gain or loss, but that the leading particles experience a net deceleration (energy loss) while the trailing particles experience a net acceleration (energy gain); the beam is thus given an energy chirp. In the non- or quasi-relativistic regime, as the beam propagates the tail of the bunch catches up to the head of the bunch, increasing the peak current. The extent of such compression is dependent on the energy chirp provided via the buncher, the beam's average energy, and the distance propagated. The ultimate compression achievable depends on space-charge effects, nonlinearities in the applied chirp, and magnitude of the applied chirp. While the net energy gain of the bunch exiting the cavity is, nominally, zero, as the beam particles transit the cavity they initially experience a net decelerating electric field and consequent reduction in energy. As the particles pass the midpoint of the cavity the magnitude of the electric field reduces to zero and reverses sign, reaccelerating the bunch. However, as space charge forces are enhanced at lower energies, the chirping process can result in beam emittance increases. Further, the incoming energy of the beam limits the chirp that can be applied to the beam; attempting to apply too large of a chirp can physically reverse the beam's direction of motion.

To address this effect, bunchers are sometimes operated "off-zero", such that the beam experiences reduced deceleration through the first portion of the buncher cavity, and exits with a net higher energy than it entered. Given the sinusoidal time dependence of the cavity field, however, the applied chirp becomes increasingly nonlinear the further "off-zero" the buncher cavity is operated.

### 4.2.2 Multi-mode Bunching

A buncher capable of supporting multiple TM mode, in contrast, breaks the tradeoff between deceleration and nonlinear chirping. Instead of synchronizing the particle bunches with the zero crossings of the rf field, the cavity modes are adjusted in phase and amplitude such that the incoming beam is accelerated, yet remains on a highly linear portion of the rf waveform. The result is a reduction (or elimination) of the beam deceleration while transiting the cavity; a net energy gain; and a highly linear chirp. Multi-mode bunching can thus mitigate the potential for emittance degradation due to deceleration; and it also allows for a stronger chirp to be applied to a lower-energy incoming beam, all else being equal, while maintaining a high degree of linearity in the applied chirp. We note that while a net more-linear slope can also be achieved using two separate $TM_{010}$ cavities at two separate frequencies, while the net sum of the energy gain and chirp might be the same, two cavities apply the effects in sequence rather than concurrently. Thus effects such as beam deceleration would still occur.

## 4.3 Dual-mode Cavity Design

The first step in designing the $TM_{010}$/$TM_{011}$ cavity was estimating the optimal length for both modes to coexist in a cylindrical pillbox cavity with a simple integer ratio between their mode frequencies, using the following equation [75] where $L_{cav}$ and $R_{cav}$ are the cavity length and radius respectively, $x_{p,m}$ is the relevant Jn Bessel function root:

$$f(L_{cav}, R_{cav}, p, m, n) = \frac{c}{2\pi}\sqrt{\left(\frac{x_{p,m}}{R_{cav}}\right)^2 + \left(\frac{n\pi}{L_{cav}}\right)^2} \tag{4.1}$$

The fundamental axial mode corresponds to the $TM_{010}$ mode with longitudinal and radial electric fields and a transverse (azimuthal) magnetic field. A similar field arrangement holds for the $TM_{011}$, except that this mode's on-axis electric field reverses direction at the midpoint of the cavity.

The simple cylindrical cavity was then modeled in Superfish [59] where an optimizer and sequencer were used to make fast and accurate changes to the cavity design to achieve both modes in the same geometry [80]. Since the frequency of the fundamental mode depends only on the cavity radius (e.g. $n$=0), while the $TM_{011}$ mode depends on both the cavity radius and length (e.g. $n$=1), in principle a cavity can be designed to support both modes at specific frequencies. The cavity was designed to resonate at 2.81 GHz ($TM_{010}$) and 5.62 GHz ($TM_{011}$), i.e. an integer ratio of 2 between the fundamental and harmonic frequencies. The frequency choice was driven by two factors. First is the desire to build and demonstrate the new device in the technologically important S/C-band regime, where research on compact and high gradient cavities is presently very active [81, 82]. Second is to benefit from the rapid advancements of high power solid state GaN amplifier technology to demonstrate beyond-klystron operation. Both then serve as a novel baseline for designing and building low cost, compact and high efficiency linac systems for industry, medicine and space exploration.

The cavity shape was then modified from that of a simple cylindrical pillbox into a re-entrant design with the intent of increasing the cavity shunt impedance (for more effiicient rf power use), and to be consistent with current practice in high gradient, high efficiency cavity design [83], again using an optimizer and sequencer. A study of the geometry was also performed where the cavity profile was analyzed for the frequency response to wall displacements, to help inform frequency tuner placement; this topic is discussed further below.

The reentrant cavity geometry was imported to COMSOL, a multiphyiscs code capable of performing 3D electromagnetic simulations (mode field distributions are shown in Figs.4.1, 4.2).

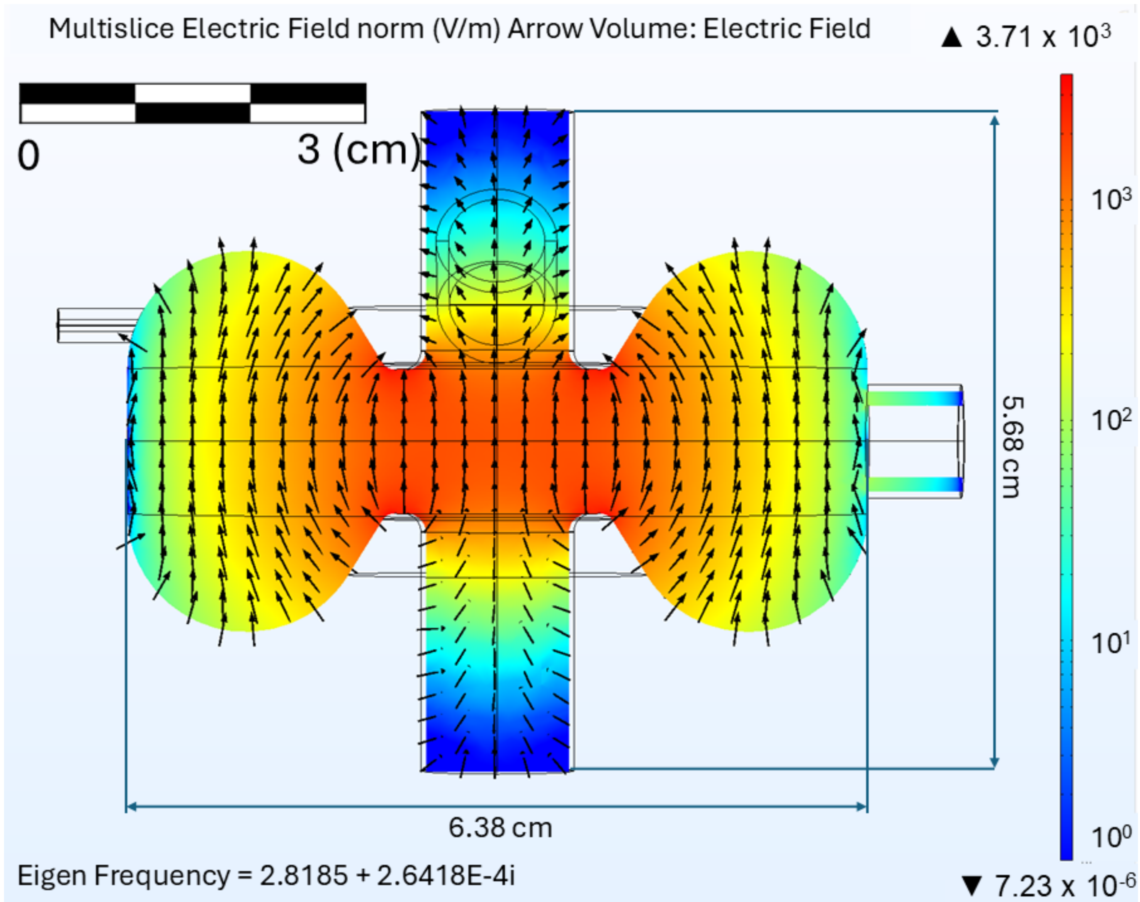


Figure 4.1 COMSOL model of fundamental mode electric field.

All COMSOL simulations were performed using an extremely fine triangular physics control mesh via COMSOL's built-in meshing module along with impedance boundary conditions related to copper material included in COMSOL. Eigenfrequency and frequency domain studies were performed to assess the cavity's performance. For Superfish a fine triangular mesh with the spacing of mesh points at 0.005 cm apart, was used. The model was retuned following the addition of tuner and RF power coupler ports. The design was such that each mode had its own independent coupler (Figs.4.4). The tuner placements identified in the 2D Superfish simulations required very little modification, and finalized port arrangements are shown in Fig.4.5. Once tuner response, coupler cross talk, and eigenfrequency mode simulations proved satisfactory, the COMSOL 3D models were converted into full CAD drawings used for fabrication and brazing. The final assembled cavity can be seen in Fig.4.3.

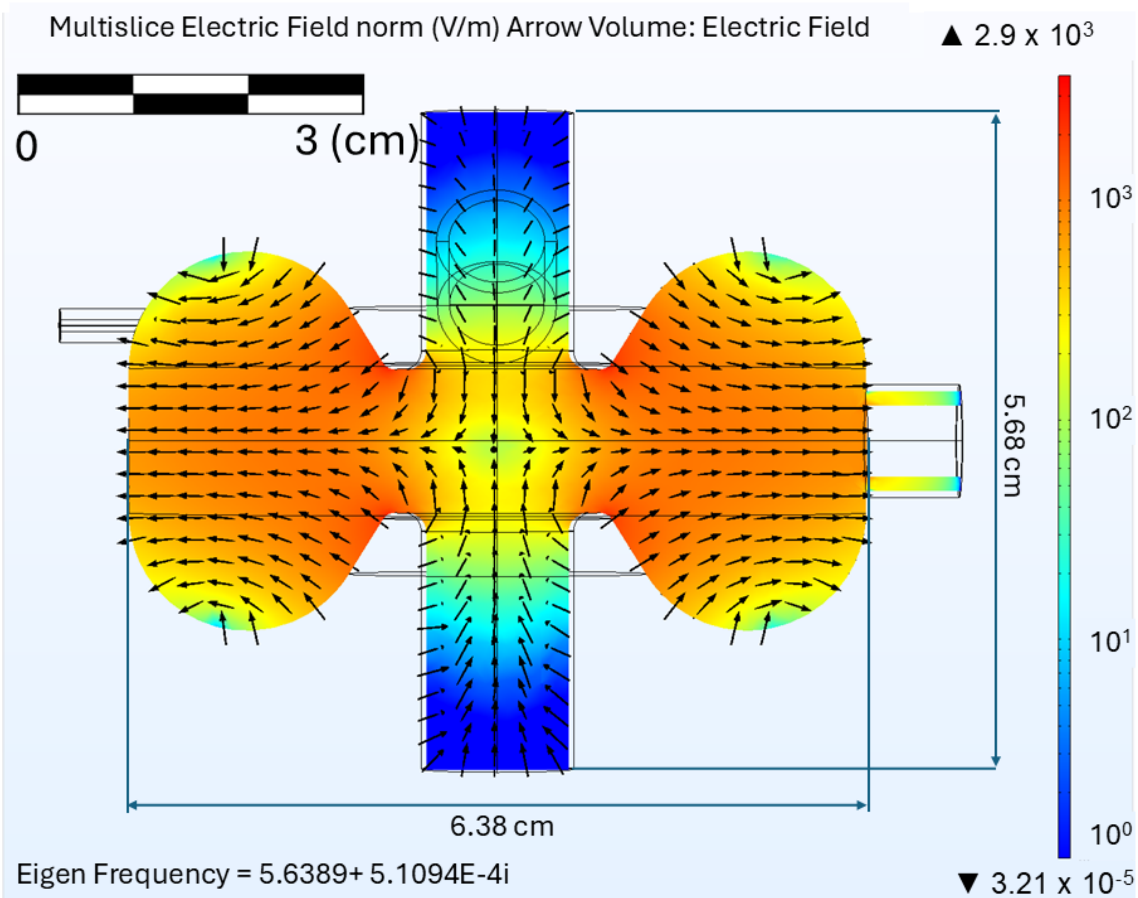


Figure 4.2 COMSOL model of $TM_{011}$ mode electric field.

### 4.3.1 Couplers

The cavity was designed with the idea of using separate couplers and RF drivers for each mode individually, which facilitates independent control of each mode's phase and amplitude, given virtually no cross-talk between the modes was found. Each coupler was placed so that it primarily interacted with only one mode. The fundamental mode was excited via a loop [83, 84] situated to couple strongly to the fundamental mode's magnetic field. Its location and orientation was optimized to exhibit minimal net coupling to the $TM_{011}$ mode.

Placement of the $TM_{011}$ mode coupler was somewhat more straightforward to downselect. As the mode's (radial) electric field exhibits a relatively high amplitude at the cavity outer radius near the cavity equator, where the $TM_{010}$ mode field has a vanishing electric field along all directions in that region (see Fig. 4.2) an electric field probe [83, 84] was an effective method to couple

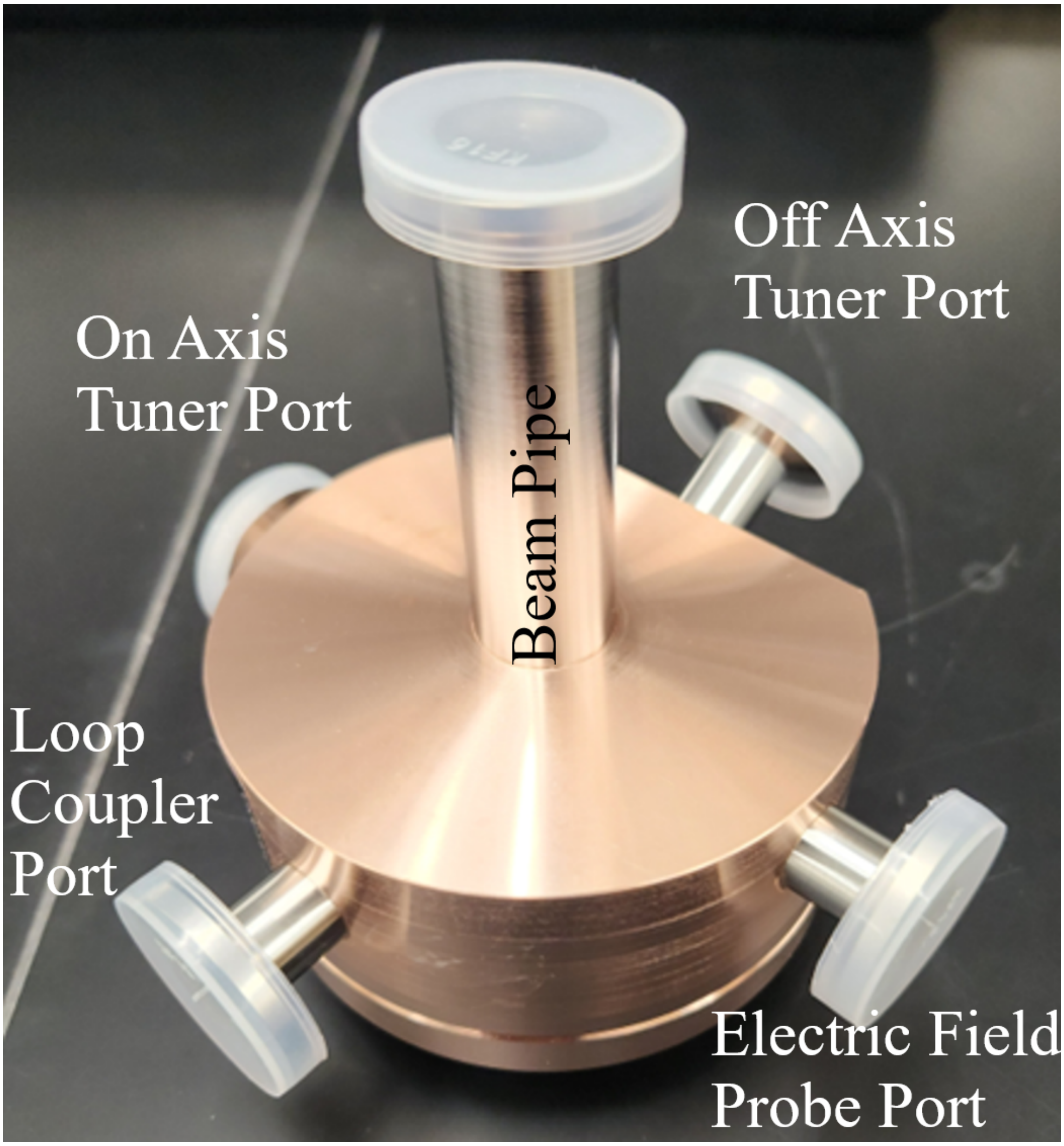


Figure 4.3 The assembled and brazed cavity.

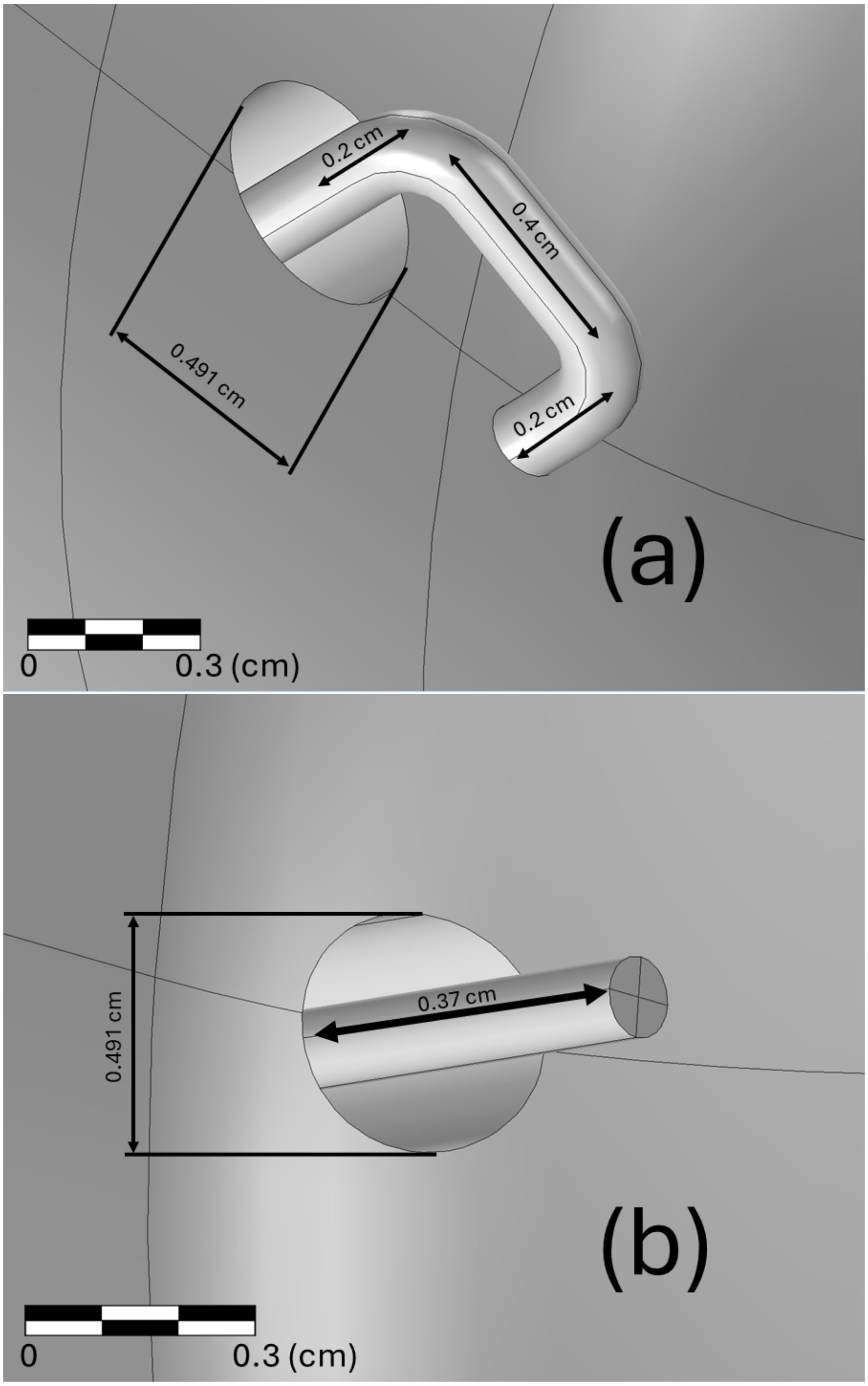


Figure 4.4 COMSOL models of coupling probes: (a) loop coupler and (b) electric field probe.

exclusively to the $TM_{011}$ mode. Its location was also optimized to account for the specifics of the cavity modes' field distributions, versus the ideal pillbox geometry. The specific method of multi-mode coupler design and placement is currently patent pending [85].

Avoiding locations of maximum field produced by each mode, and instead balancing all field at a given location, helped minimize cross-talk between the couplers. This is important in a two coupler system as strong cross talk can be detrimental to system performance. Couplers with significant crosstalk would both lower the overall cavity efficiency (e.g. in terms of rf power required to obtain a given accelerating gradient) due to undesired power out coupling, but also necessitate the rf network having a highly robust and effective, harmonic rf isolation system between the cavity and rf power sources.

### 4.3.2 Tuners

Maintaining synchronization between the modes (e.g. integer or simple-fraction frequency ratios) is critical for maintaining coherence between them and beams transiting the cavity. Any deviation from the integer ratio of 2 between the modes' resonant frequencies would cause a phase shift increasing over time which would, in turn, change the desired superposition field in the cavity. Such phase drift could be compensated by re-phasing the modes in the inputs. The larger the deviation from the ratio of 2 the stronger the drift. Hence, frequency ratios as near 2 as possible are strongly preferred for stable performance. For our cavity, ideally, the modes should be integer multiples of one another, specifically the frequency of the $TM_{010}$ should be exactly 1/2 of the frequency of the $TM_{011}$ mode. (Small differences in frequency ratios can in principle be addressed by, for instance, increasing the input power and operating slightly off the natural resonance; but such approaches depend on the magnitude of the ratio error and the cavity bandwidths. It is thus generally preferred to have the frequency ratio as close to ideal as possible from the start.) To further optimize the performance of the cavity, tuners have been implemented: an on-equator tuner and an off-equator tuner. The tuners are plungers [86, 87] and together enable independent adjustments to the resonant frequencies of the two modes within the cavity. Inserting or retracting the tuners alters the cavity volume [87] and thus the frequencies of the modes. The on-equator tuner, when inserted, effects a positive change in frequency of $TM_{011}$ with a concurrent negative change in frequency of $TM_{010}$. The off-equator tuner, on the other hand, increases the resonant frequency of both modes when inserted. The relative insertion depth of the two tuners can, within limits, be set to attain the desired integer ratio of 2 between the $TM_{010}$ and $TM_{011}$ resonant frequencies, as well as set an absolute frequency for one of the modes.

## 4.4 Characterization of a Dual-mode cavity

### 4.4.1 Bead Pulls of the On-Axis Electric Field

Perturbing the electromagnetic fields in a cavity in a small volume, using for instance a small metal bead pulled through the cavity, will change the resonant frequency of a mode based upon the magnitude of the perturbation [88, 89]. This allows the mode's spatial field pattern to be mapped, in the limit of small perturbations [90–95]. When mapping the on-axis fields of the mode, where the magnitude of the magnetic field is negligible, the relative magnitude of the unperturbed electric field $E_p$ within the perturbed volume is related to the mode frequency change simply by [90]

$$E_p \propto \sqrt{\frac{\omega - \omega_0}{\omega_0}} \tag{4.2}$$

This method allows for mapping the on-axis fields of both modes to verify the field pattern predicted by COMSOL, and also to verify the mode identification performed via network analyzer. A bead consisting of a 16 gauge (1.3 mm diameter) 3 mm long section of copper wire attached to a dielectric string was pulled through the cavity in 1 mm increments along the longitudinal axis, and the cavity mode frequency measured as a function of the bead's position, the experimental setup of which can be seen in Fig.4.6. These measurements were performed for both modes. A simulated bead pull was also performed using COMSOL where a similarly sized cylinder was used as a stand-in for the wire section. This allows for a direct comparison between the experimental bead pull and a simulated bead pull. Comparing the results, it is seen that there are certain features of the field that are not captured by simple 2D simulations, nor by simply comparing the on-axis field from an eigenmode solver to the beadpull measurement. For instance, the differences in field magnitudes

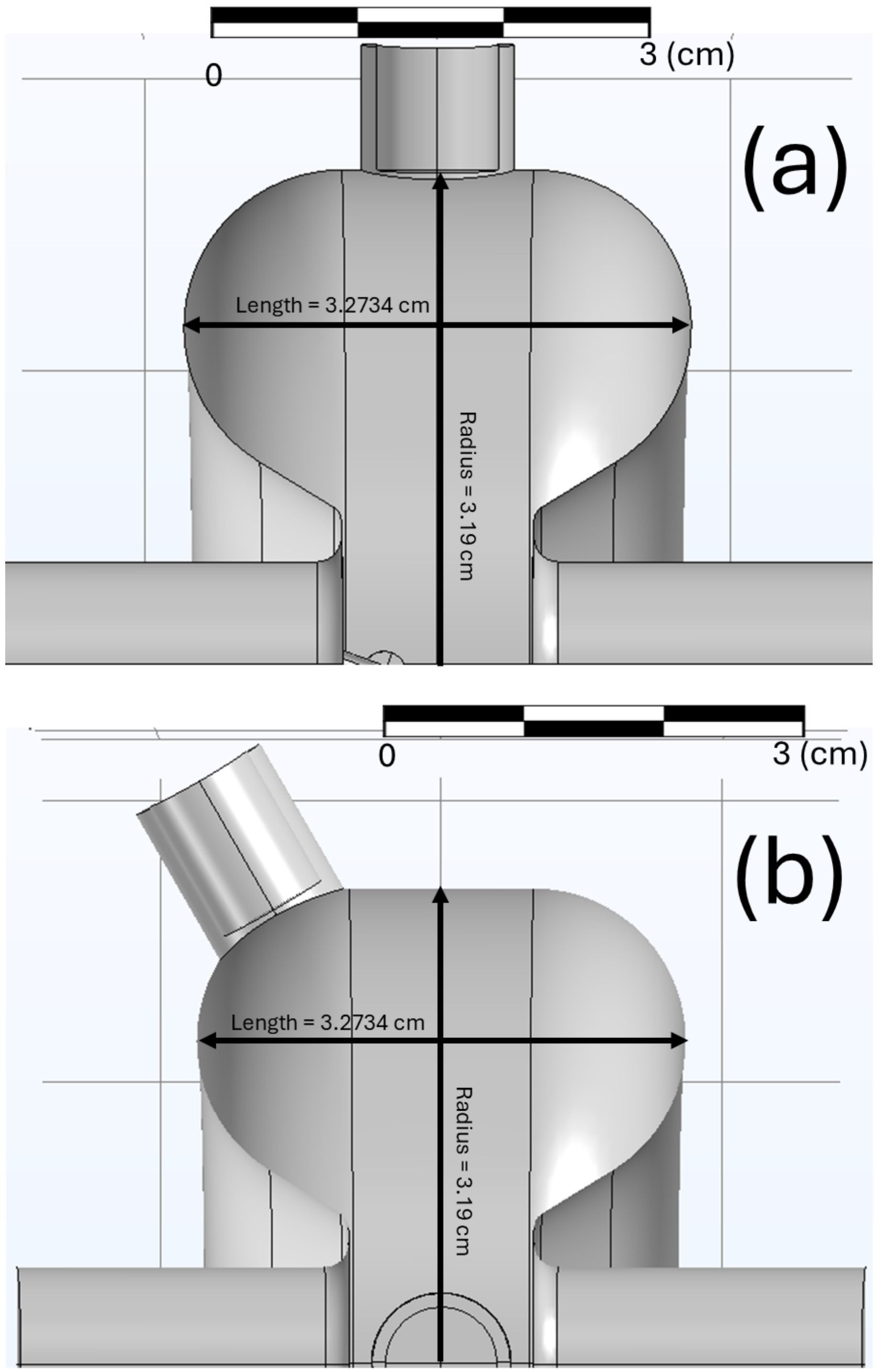


Figure 4.5 COMSOL models of tuners: (a) on-equator tuner and (b) off-equator tuner.

at the cavity/beamtube boundary is likely due to asymmetries introduced from adding the tuners and rf power couplers. The harmonic bead pull data are also noisy near the zero crossing; this is expected from the nature of the perturbation-based measurement. The extinguishing/quenching fields, such as near the cavity boundaries or field zero-crossing, are particularly difficult to measure due to its low amplitude; this can be seen from superimposing the simulation and the experimental data revealing bead-mediated noise. Overall, there is an excellent agreement between the simulated and experimental $E_p$ results as shown in Fig. 4.7 and Fig. 4.8 with exact numerical comparison shown in Table 4.1. A variation on this method was used previously with a larger bead and multiple tests which also saw similar results [96].

### 4.4.2 Measured Q-factor and Mode Frequencies

The quality factor was measured using a vector network analyzer (VNA) within the standard $S_{21}$ approach [84, 92, 97, 98], where $Q_L$ (loaded quality factor) was determined by measuring the resonant frequency $\omega_0$ and determining the bandwidth $\Delta\omega$ (using two –3 dB points off of the $S_{21}$ peak):

$$Q_L = \frac{\omega_0}{\Delta\omega} \tag{4.3}$$

An electric field probe placed in the beam port along the beam axis was used as the pickup probe for all $Q$-factor measurement. Once the desired probe was inserted into its respective port and coupled strongly to the cavity, the $Q$-factor was measured based on the $S_{21}$ response. The pickup probe was shortened and the $Q$-factor was again measured. This was repeated until a minimal coupling, $\beta \approx 0$, was attained for the pickup probe. At the same time, the coupler, feeding the input power into the cavity, was critically coupled, $\beta = 1$, meaning reflected power is 0, resulting in a total cavity coupling coefficient of 1. Multiple measurements, including removing and replacing the couplers, yielded $Q_0$=8–9k, where $Q_0 = Q_L \cdot (1 + \beta)$ [13]. These results were reasonably close to the computed values of ~11k from COMSOL and speak to the high fabrication quality of the cavity. The resonant frequencies for both modes were within 10 MHz from their design values.

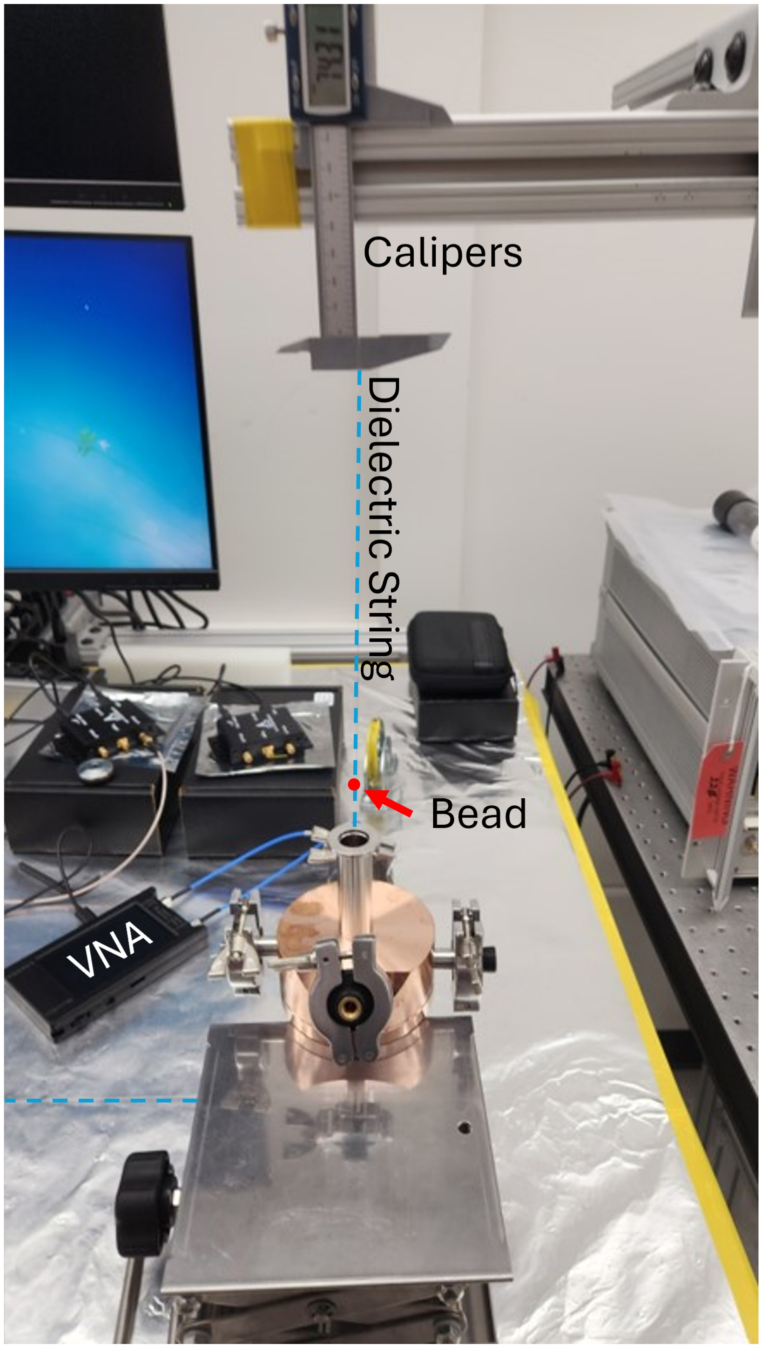


Figure 4.6 Experimental bead pull setup.

Table 4.1 Simulation (sim) and experimental (exp) $Q$-factors and resonant frequencies (with tuners removed).

| Parameter | $TM_{010}$ | | $TM_{011}$ | |
|---|---|---|---|---|
| | exp | sim | exp | sim |
| $Q$-factor | 8407 | 10661 | 9362 | 11299 |
| $f_0$ (GHz) | 2.8166 | 2.8186 | 5.6267 | 5.6388 |

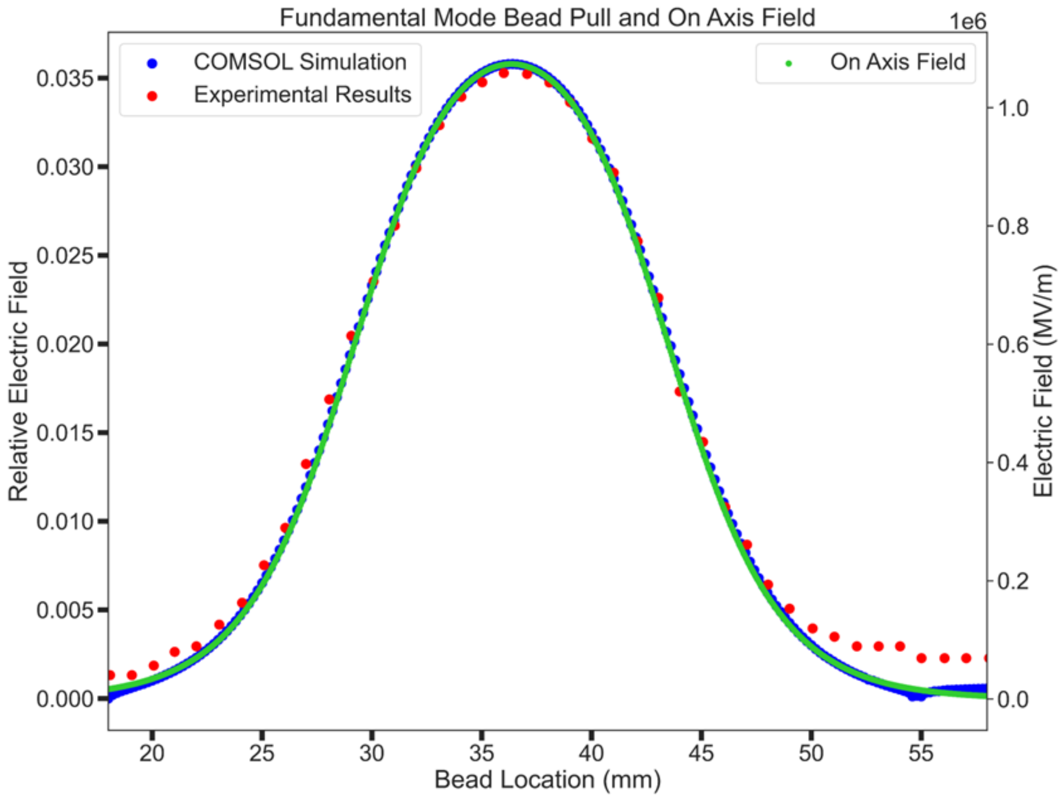


Figure 4.7 Fundamental mode bead pull and COMSOL simulated bead pull results (left axis) compared to on-axis field taken from Superfish (right axis). Bead pull results were obtained by normalizing the raw data to energy stored in the cavity.

### 4.4.3 Mode Cross Talk Testing

As noted previously, in our design for operating two independent couplers in a single cavity, each is intended to have $\beta = 1$ coupling to the desired mode and $\beta \approx 0$ for the other driven mode. To make a practically usable device it must be ensured that there is minimal power transmitted between the couplers. Power couplers which are strongly interacting with both their own and other powered modes (cross talk in other words) would result in potentially significant fractions of power being uselessly transmitted between the couplers with net diminished power coupled to the cavity volume. As this was an anticipated issue, coupler locations and geometries were modelled and optimized so as to minimize the cross talk. The fabricated multimode cavity, was used to characterize the crosstalk. The results shown in Figs. 4.11 and 4.12 highlight the low transmitted power between

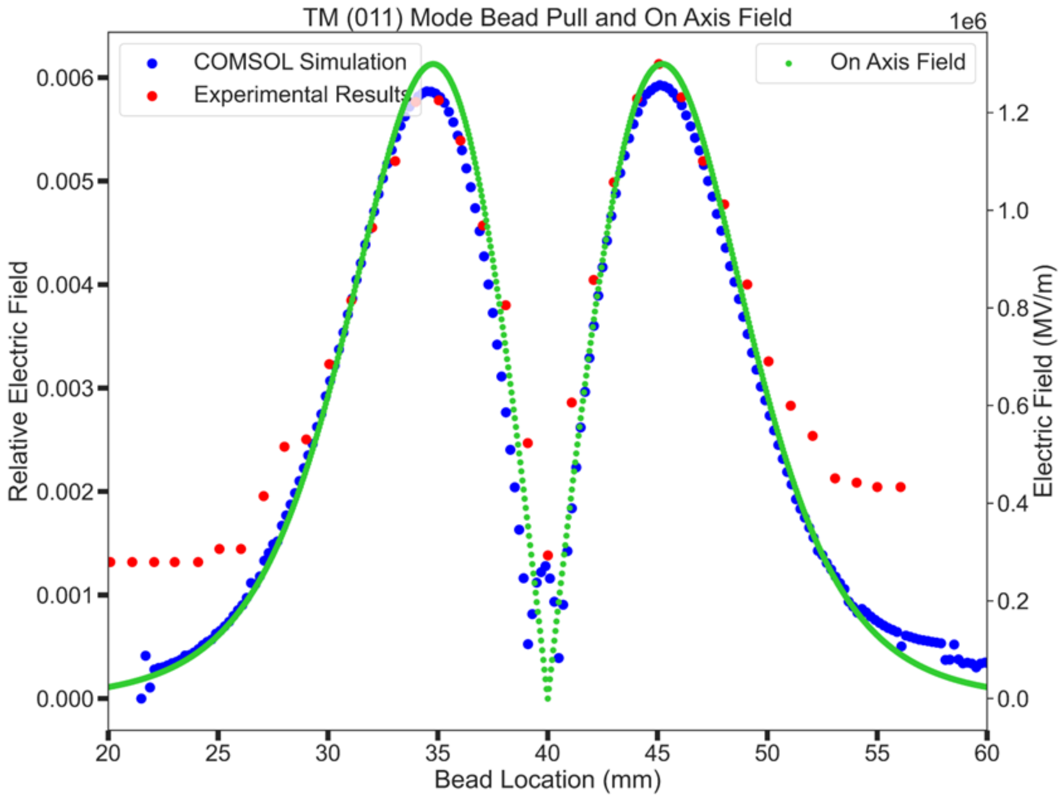


Figure 4.8 $TM_{011}$ mode bead pull and COMSOL simulated bead pull results (left axis) compared to on-axis field taken from Superfish (right axis). Bead pull results were obtained by normalizing the raw data to energy stored in the cavity.

the couplers. When calculated from the log-scale, approximately 2% of power at f=2.81652 GHz was transmitted from the loop coupler to the electric field probe and 0.3% of power at f=5.62667 GHz was transmitted from the electric field probe to the loop coupler. The crosstalk could likely be reduced further with additional optimization, however, the attained crosstalk levels were very low and practically adequate to the use of the demonstrate cavity for high power testing. In practice, the adjustment process is somewhat tedious, and future studies should incorporate efforts to simplify the design and streamline the tuning process. When the loop coupler's coupling to the $TM_{011}$ mode was explored, as opposed to the designed-for fundamental mode, it was found, as expected, that the coupling was dependent upon the orientation of the loop coupler. The electric field probe, intended to couple to the $TM_{011}$ mode exhibited almost no coupling to the $TM_{010}$ mode, due to the

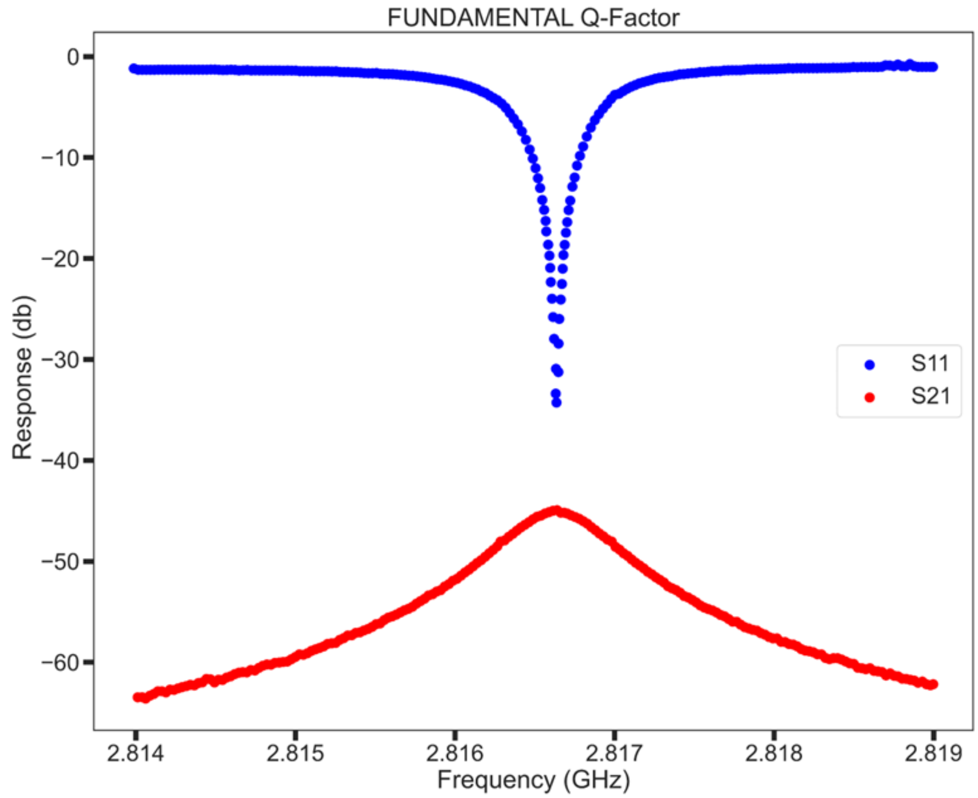


Figure 4.9 Experimental $S_{11}$ and $S_{21}$ used to measure fundamental mode $Q$-factor.

minimal electric field magnitude that mode exhibits at the cavity equator, also as expected. These observations are consistent with the crosstalk measurements.

### 4.4.4 Tuner Response

The resonant frequencies of the $TM_{010}$ and $TM_{011}$ cavity modes were recorded as the tuners were moved in/out in ~0.3 mm steps, equivalent to quarter turns of the rods seen in Fig. 4.13. The Resonant frequencies were measured as 2.817483 GHz for the $TM_{010}$ mode and 5.626673 GHz for the $TM_{011}$ mode, with a frequency ratio of 1.9971. The tuner plugs were mounted and zeroed at the flange connection for each port prior to moving them. These tests were intended to determine the tuning range accessible by these tuners: with either $(i)$ the tuner being pulled out of the cavity so far it no longer had any effect on the resonant frequency, or $(ii)$ the tuner inserted far enough into the cavity to detune a mode to the point of significantly altering the field pattern and/or impacting its

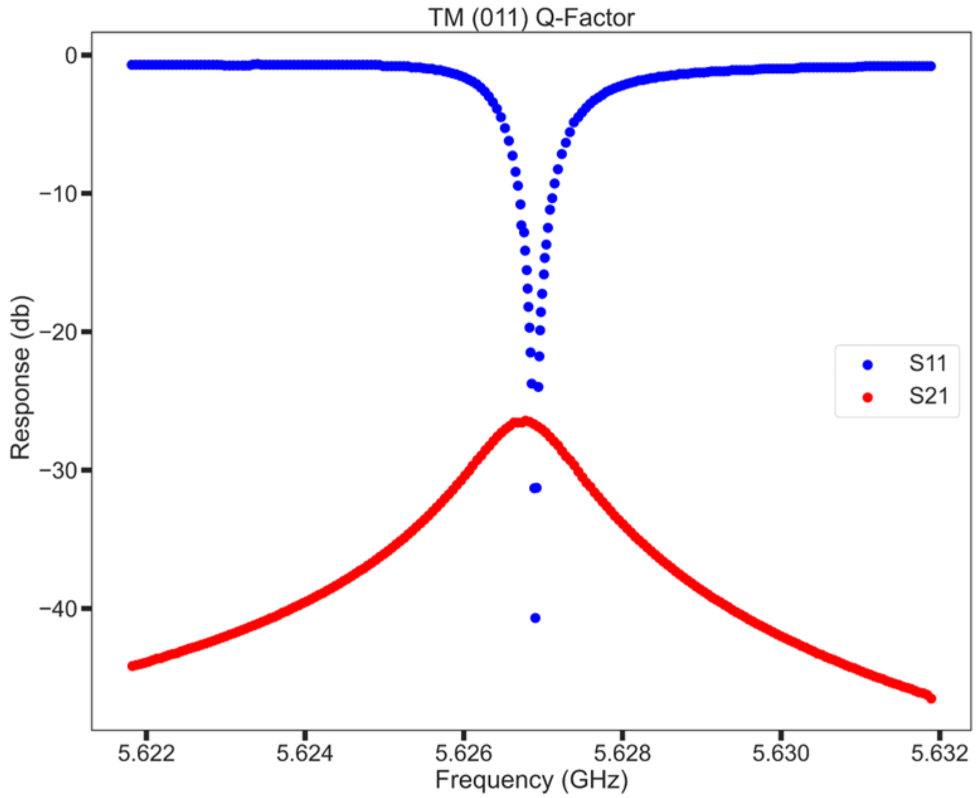


Figure 4.10 Experimental $S_{11}$ and $S_{21}$ used to measure $TM_{011}$ mode $Q$-factor.

coupling. The results of the tuner tests are summarized in Figs. 4.14 and 4.15, along with simulated runs from COMSOL. The as-designed and actual operating results are in excellent agreement.

Using this data, we can better visualize tuner performance by creating heat maps which illustrate the individual tuners' effects as well as their combined effects. Starting with the $TM_{010}$ frequency response in Fig.4.16, the black vertical and horizontal lines identify the tuner "zero position" – approximately where the tuner is level with the cavity wall, and further insertion begins to significantly perturb the mode volumes. These lines let us logically divide the heat map into four quadrants. Quadrant #4 is where both tuners are retracted past the cavity wall, and there is negligible frequency change from either tuner's motion. Quadrant #1 captures the effect of inserting the off-equator tuner only which mirrors the expected frequency change seen in Fig. 4.14: the frequency increases as the tuner insertion depth increases. Quadrant #3 captures the effect of inserting only

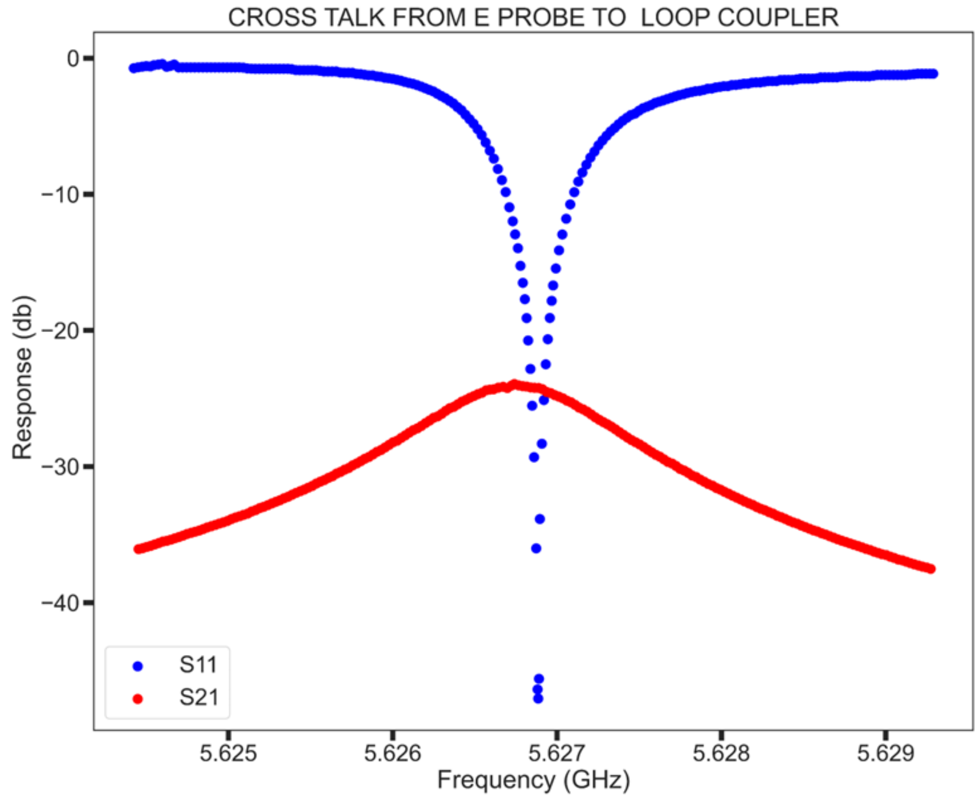


Figure 4.11 Experimental $S_{11}$ and $S_{21}$ used to measure cross talk from electric field probe to loop coupler.

the on-equator tuner and the result mirrors the effect seen in Fig. 4.15 where the frequency increases as the tuner is inserted into the cavity. Finally, quadrant #2 captures the effect of both tuners being inserted concurrently. This performance is as expected given the tuners' independent responses.

The same mapping and visualization approach was used for characterizing the $TM_{011}$ mode frequency response. The black horizontal and vertical lines label zero tuner locations in Fig. 4.17, however there is greater frequency response within quadrant #4 as compared to that seen in the fundamental mode, see Fig. 4.16. This is expected due to the higher frequency mode's evanescent field penetrating deeper into the tuner ports than the fundamental's. As the frequency response for $TM_{011}$ mode is not in the same direction, quadrant #1 and quadrant #3 now show opposite frequency changes, as compared to the results in Figs. 4.15 and 4.14. Quadrant #2 captures the

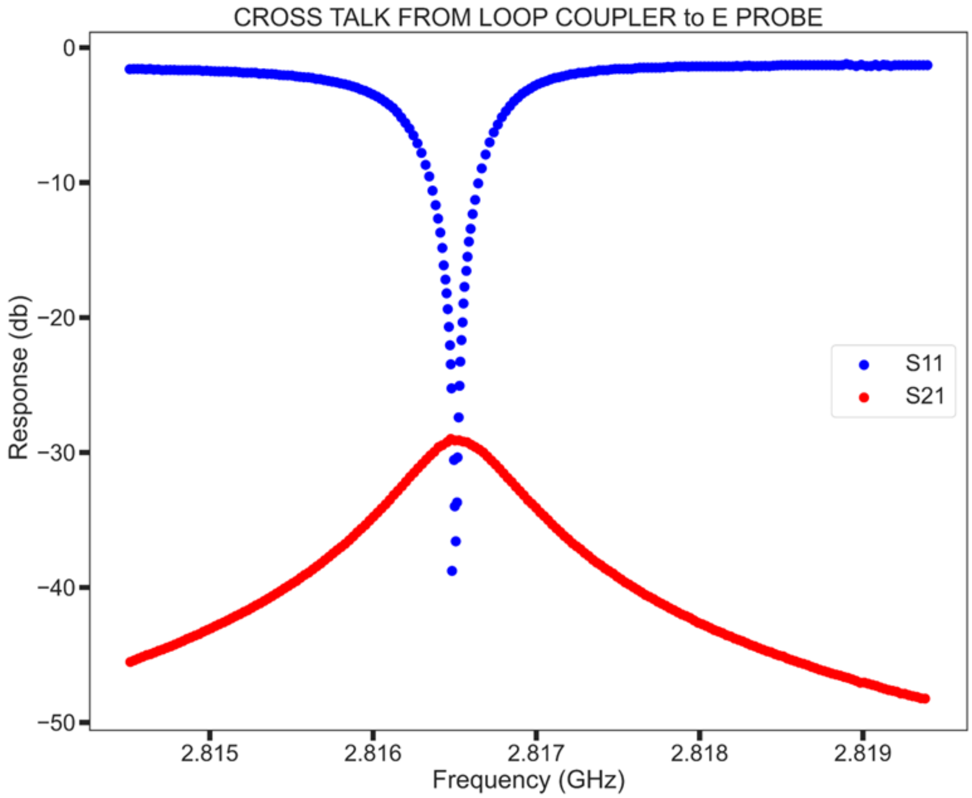


Figure 4.12 Experimental $S_{11}$ and $S_{21}$ used to measure cross talk from loop coupler to electric field probe.

combined effects of two tuners being inserted into the cavity.

Tuners can only modify the frequency in limited amounts before their effects are detrimental to the cavity performance, e.g. excessive losses on the tuner, coupling perturbation, etc. Thus designing a multi mode cavity to have integer multiple mode frequencies from the start is critical to the final performance; ideally following fabrication, the cavity would have both a fundamental mode frequency and mode frequency ratios exactly at the design values with the tuners flush with the cavity walls. In practice, some manufacturing deviations are to be expected, and therefore the ability to perform frequency adjustment is necessary.

Taking the ratio of the harmonic map and the fundamental map, a new map of the frequency

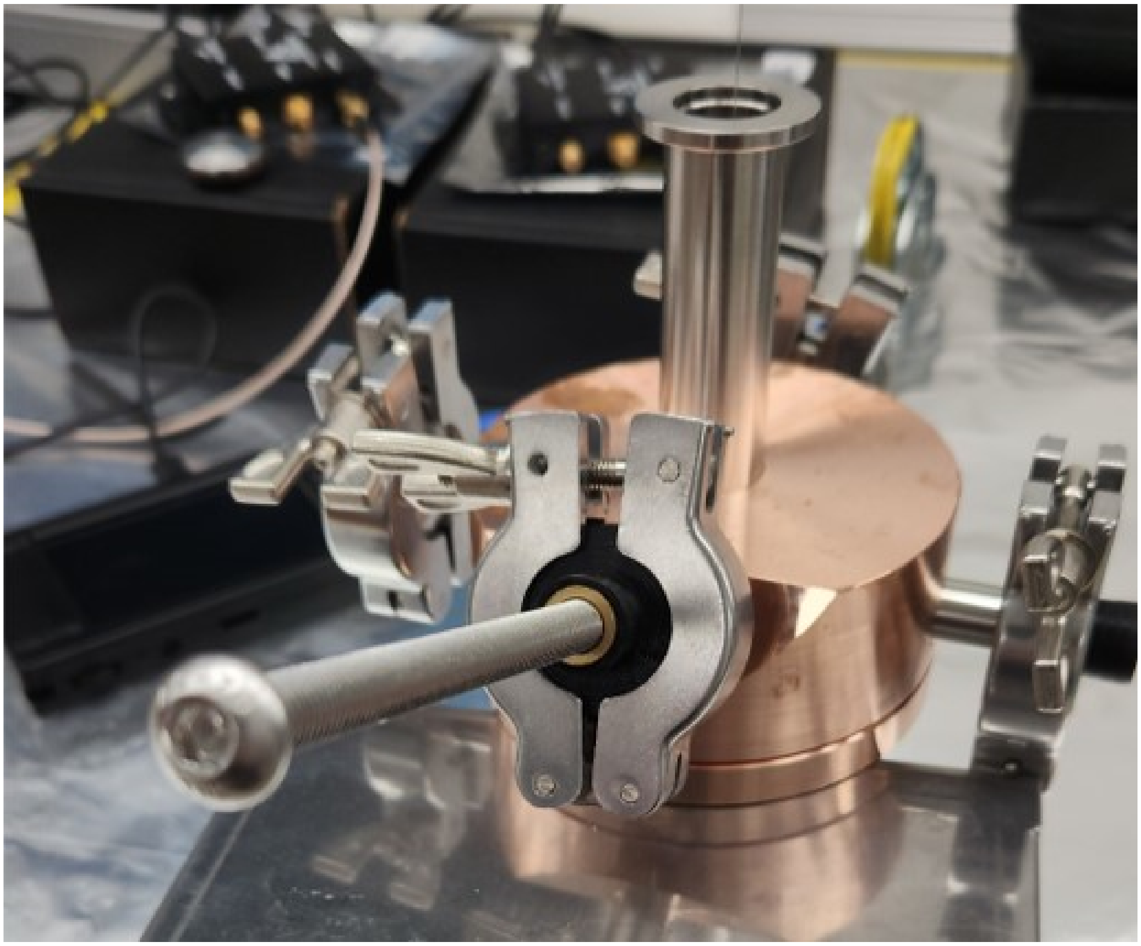

Figure 4.13 Experimental tuner setup.

ratio can be created, as seen in Fig.4.18.

$$FrequencyRatio = \frac{TM_{011}}{TM_{010}} \tag{4.4}$$

The frequency ratio is dependent on the operating modes $TM_{010}$ and $TM_{011}$, which can fluctuate based on a variety of factors such as temperature of the cavity(near 20 °C), coupler insertion and tuner depth. The frequency ratio map shows the frequency ratio given a fixed coupler length and constant cavity temperature. It therefore provides the locations of the tuners and the subsequent frequency ratio which can then be used to tune this cavity to the desired $n = 2$ integer. For the demonstrated system the desired $n = 2$ integer was not achieved. This is due to the initial frequency ratio measured and the ways that the tuners are able to manipulate the frequency ratio. As observed from the tuner response results, the designed and fabricated system can increase the

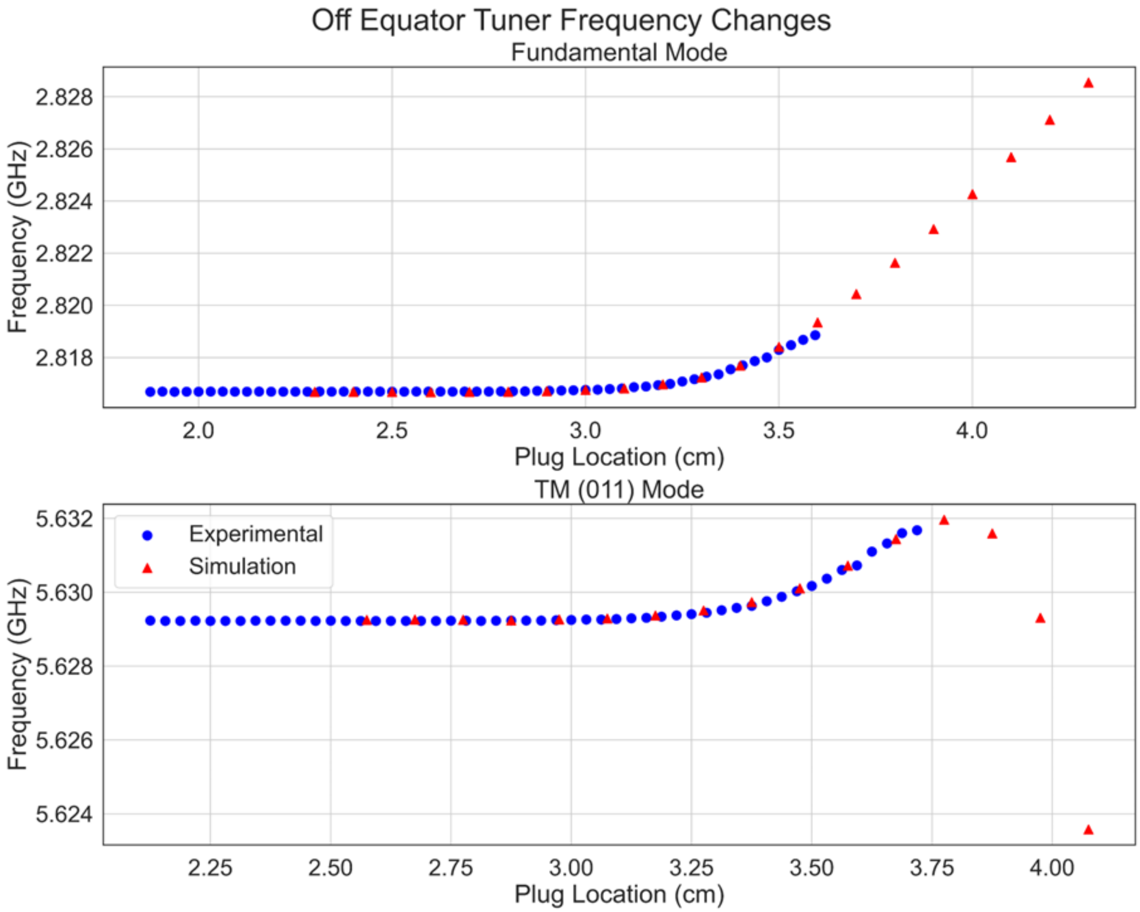


Figure 4.14 Frequency response from the off-equator tuner.

fundamental mode's frequency significantly. Ignoring, for the moment the change to $TM_{011}$, the $TM_{010}$ frequency can be increased to the point when it is at an integer multiple of a fixed $TM_{011}$ frequency. Thus, a decrease in the frequency ratio of the system is easily achievable, i.e. $n = 2.1$ being lowered to $n = 2$ . This is not true for the $TM_{011}$ frequency. If now change of $TM_{010}$ is ignored, it can be seen that due to the opposing response for each tuner it is easiest to maintain the frequency of $TM_{011}$ instead of making it strongly increased or decreased. These observations lead to the conclusion that deviation from the target $TM_{011}$ frequency is much harder to compensate for, than deviation of $TM_{010}$ frequency. Combining the responses at both frequencies together, it can be found that this system has the ability to decrease the frequency ratio between the modes by maintaining the $TM_{011}$ frequency and increasing the $TM_{010}$ frequency. To summarize, the cavity can be more easily tuned if $f_{011}/f_{010} > 2$ than if $f_{011}/f_{010} < 2$. Figure 4.19 shows a modified $TM_{010}$

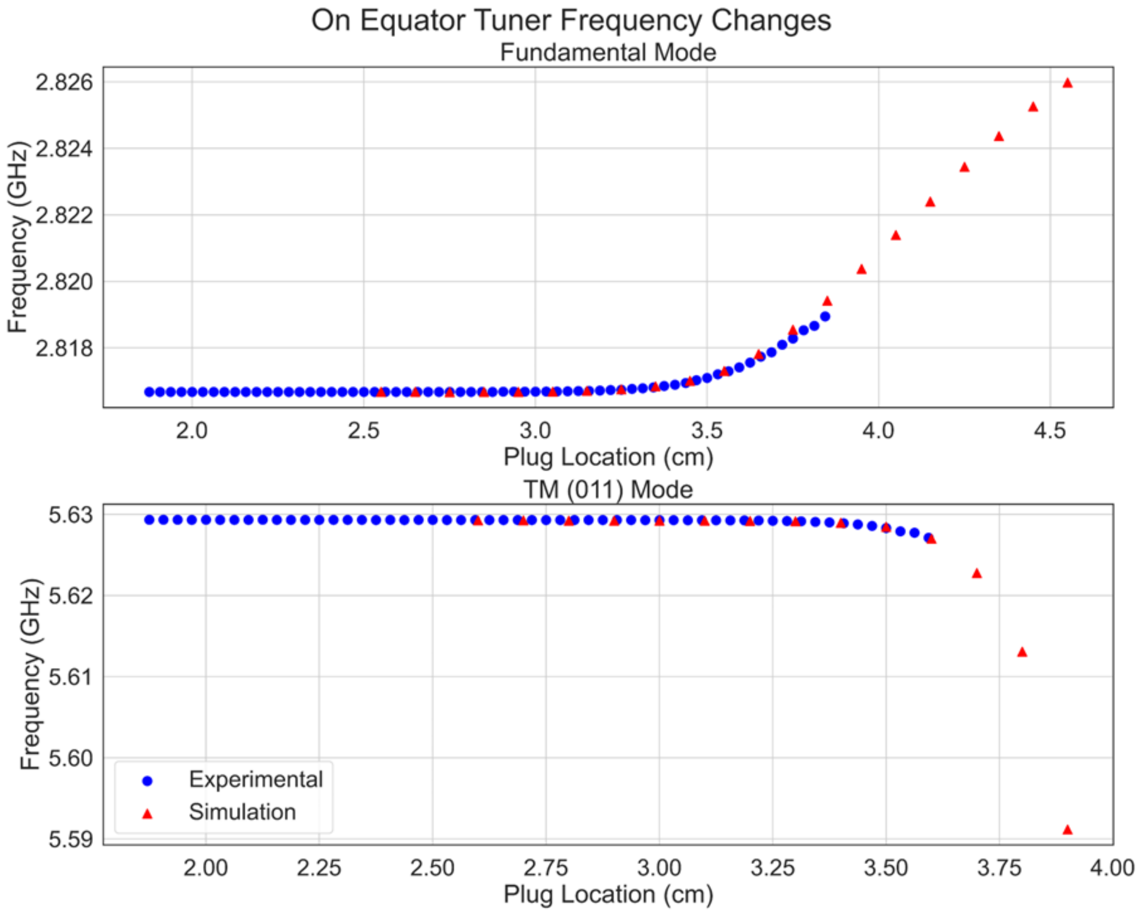


Figure 4.15 Frequency response from the on-equator tuner.

decreased by 0.005 GHz with an initial frequency ratio of 2.0006. In this theoretical case where n > 2 the tuning system is more capable to approaching a n = 2 integer multiple. The simulated design resonant frequencies seen in Table 4.1 have a frequency ratio > 2 however the fabricated cavity resulted in a frequency ratio < 2, limiting the tunability of the system. While an analysis of cavity response and potential fabrication errors is normally a part of any cavity fabrication process, the above discussion illustrates additional considerations that should be taken into account when designing multi-frequency multi-mode structures.

### 4.5 Conclusions and Outlook

A dual-mode cavity was successfully designed, fabricated and tested. The measured Q-factor was in good agreement with simulation results indicating that additional ports were chosen and implemented properly, such that they did not substantially increase the loss due to the increased

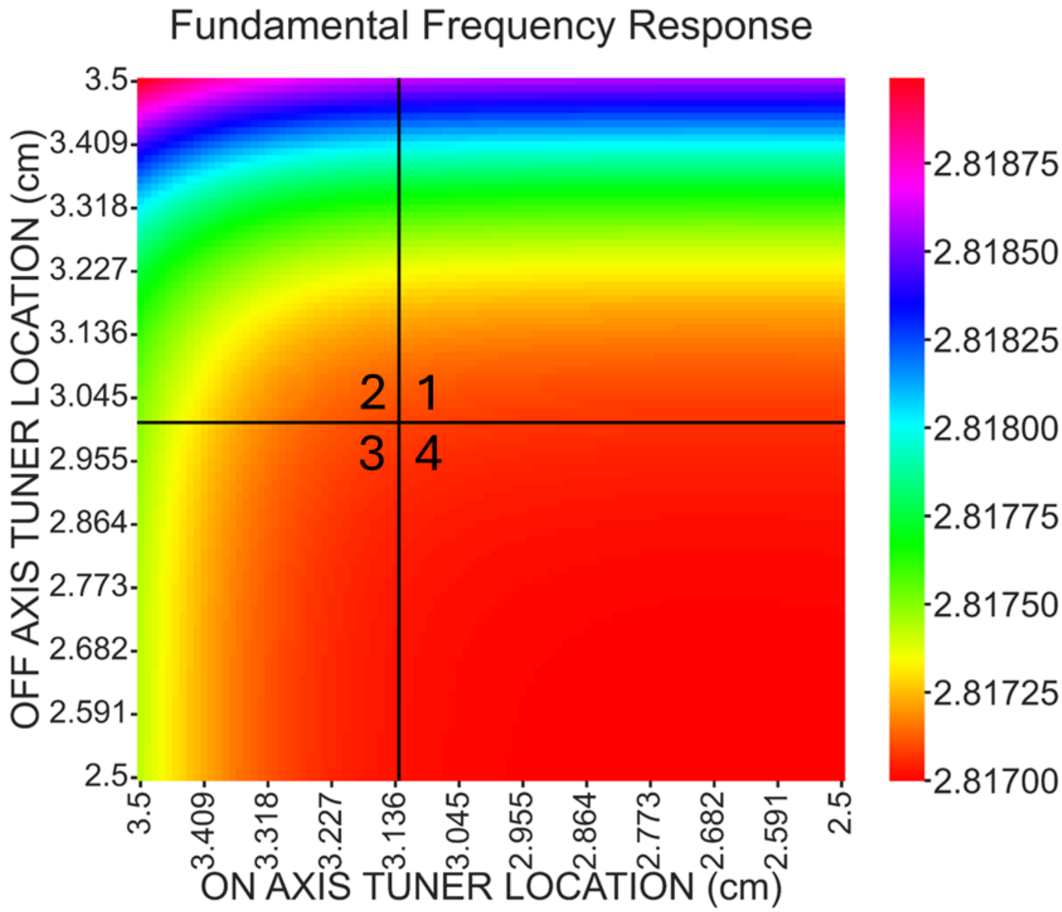


Figure 4.16 Heat map of the fundamental frequency based off of tuner locations.

amount of boundaries inside the cavity as compared to the canonical single TM mode cavity design. The success of the dual-coupler design, specifically the low cross-talk between the modes, provided design principles that could be implemented for a whole new variety of dual-mode cavities. The simultaneous manipulation of each frequency independently, while maintaining their ratio, if necessary, is huge. This allows one to attain and maintain particular electric field profiles/shapes (through superposition) while fine-tuning frequencies to best match within the input RF source bandwidth for best power coupling (another aspect of the overall energy system budget via minimizing reflected power). In the experiments, the tuning system was limited by the initial frequency ratio of the cavity but did demonstrate the exact expected behavior. Future work could be envisioned for minor design modifications to attain the frequency ratio of > 2 thereby enabling even better cavity tunability.

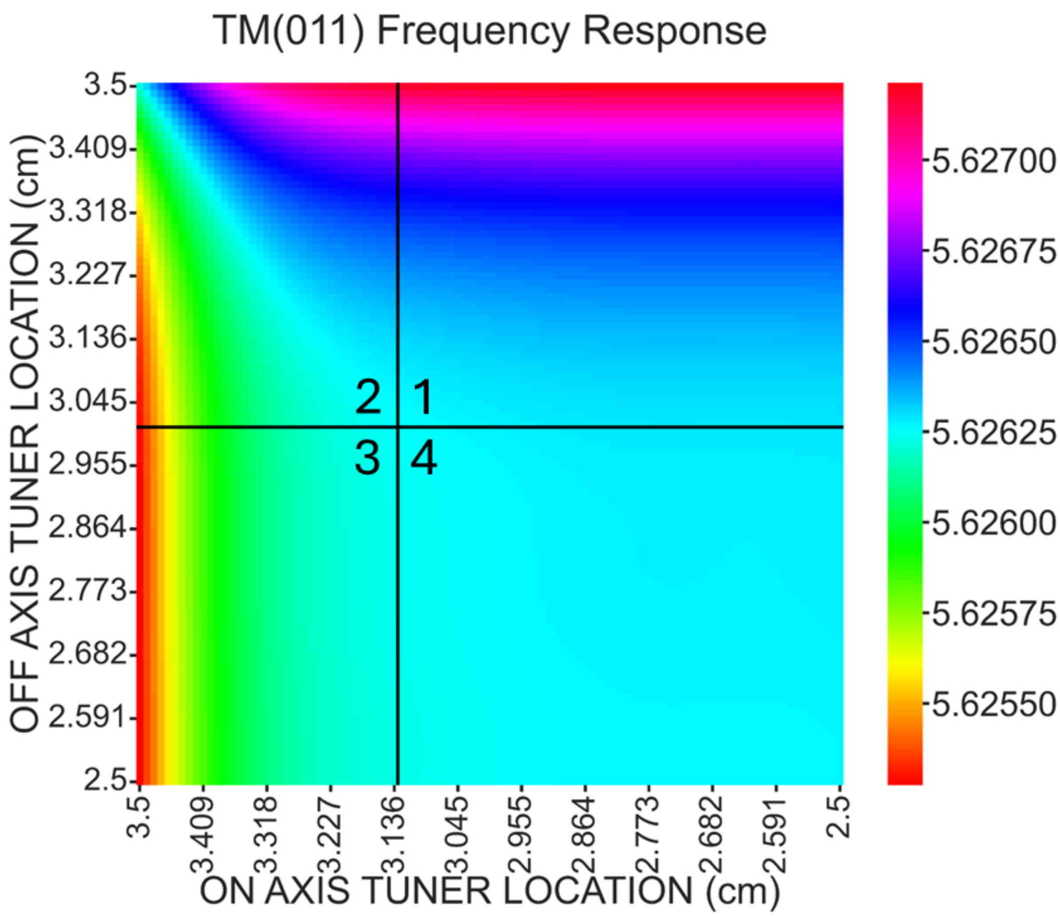


Figure 4.17 Heat map of the harmonic frequency based off of tuner locations.

This cavity amalgamates functionality typically distributed across several cavities (acceleration, bunching/chirping and linearization) into a single resonant structure, conserving valuable space in a beamline and providing potential performance improvements. Its relative simplicity in implementation and inherent ability to host other, even higher-order, modes with small deviations in design broadens applicability of the presented cavity across various applications. For example, higher-order modes can be used to decrease energy spread induced on a pre-bunched beam following bunch compression, or storing or reading out information in quantum information SRF platforms.

The design approach offers the benefits of compactness, cost and improved performance/efficiency within a minimal footprint, These are important considerations for applications where space and mass are at a premium, such as accelerators intended for spaceflight; but also can be important

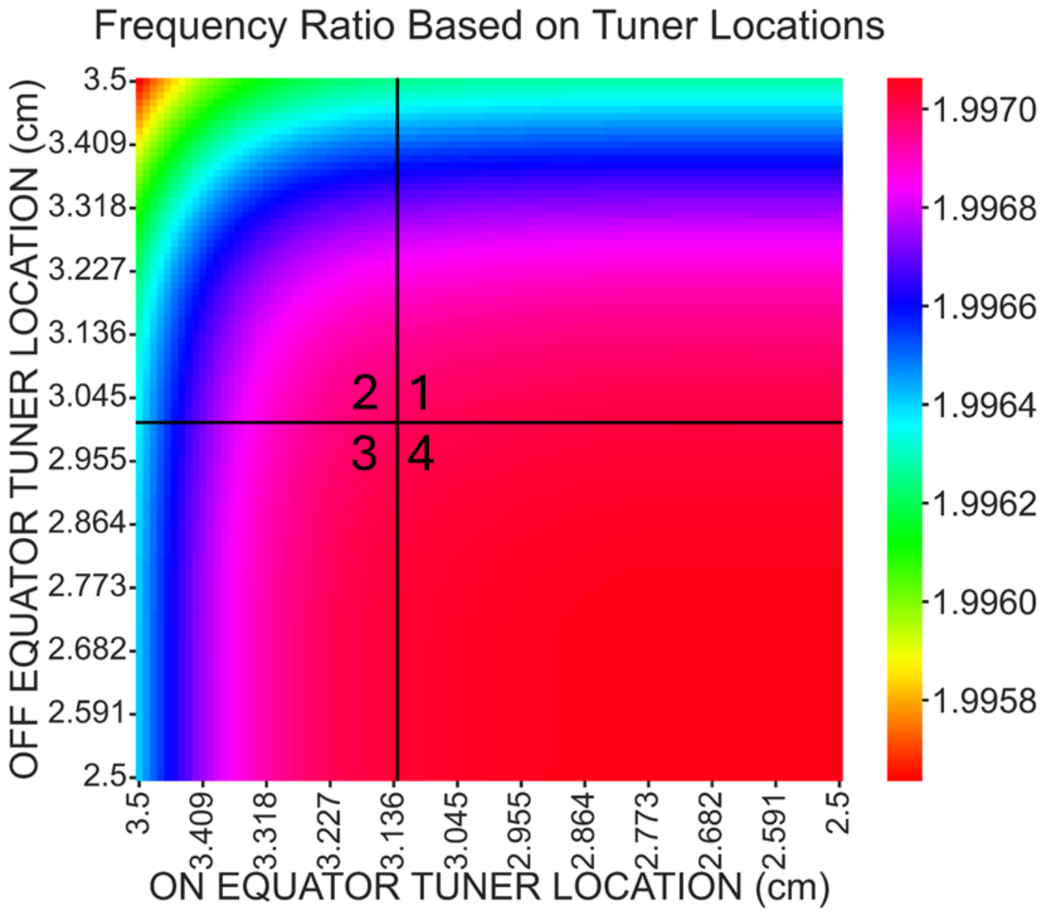


Figure 4.18 Experimental Frequency ratio between $TM_{011}$ and $TM_{010}$ modes based off of tuner locations with initial resonant frequencies at 2.817483 GHz for the $TM_{010}$ mode and 5.626673 GHz for the $TM_{011}$ mode. Frequency ratio of 1.9971.

in laboratory settings, medical devices, or industrial environments. A compact beamline not only facilitates easier integration into existing infrastructure but also enhances portability, if needed, providing greater flexibility in deployment.

### 4.6 Acknowledgments

The work by Benjamin Sims was supported by the U.S. Department of Energy Office of Science, High Energy Physics under Cooperative Agreement Award No. DE-SC0018362. The work by Sergey Baryshev was supported by the U.S. Department of Energy, Office of Science, Office of High Energy Physics under Award No. DE-SC0020429.

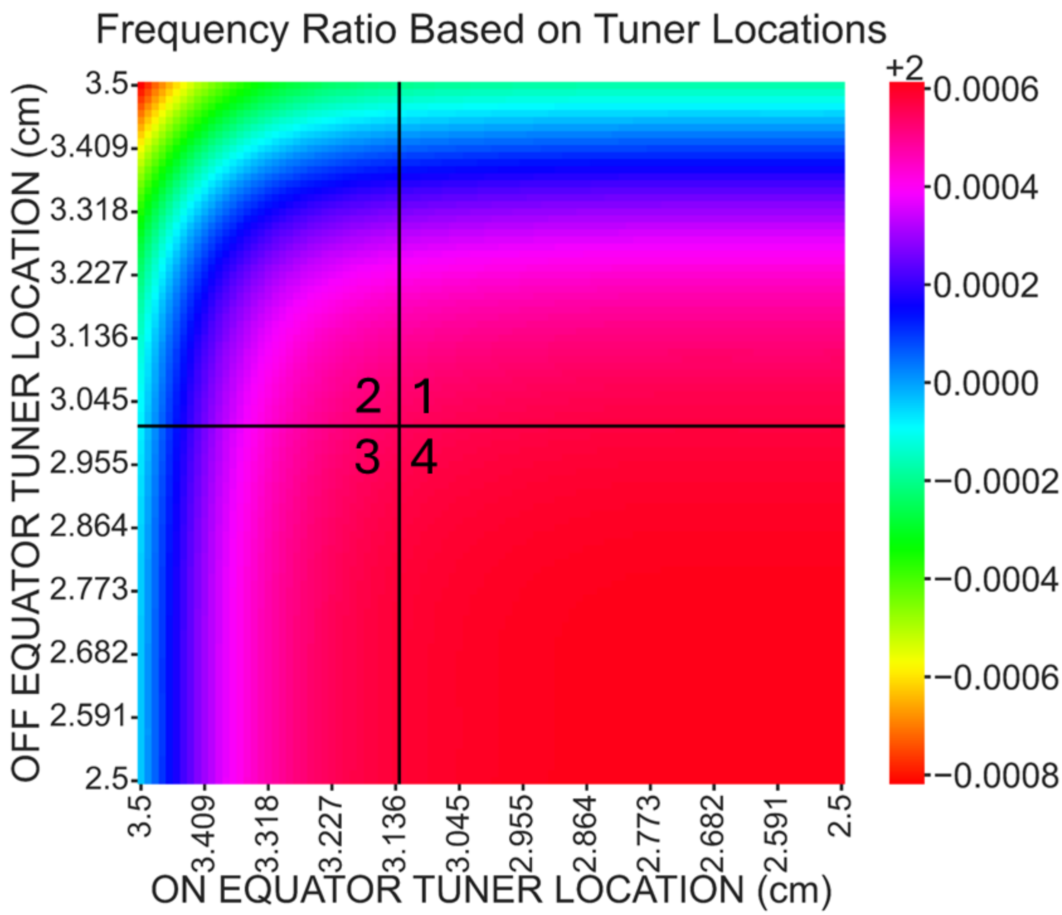


Figure 4.19 Simulated frequency ratio between $TM_{011}$ and $TM_{010}$ modes with initial resonant frequencies at 2.812483 GHz for the $TM_{010}$ mode and 5.626673 GHz for the $TM_{011}$ mode. Frequency ratio = 2.0006.

# CHAPTER 5

# CONCLUSION

This thesis has focused on understanding and managing emittance as well as utilizing novel approaches to improve brightness. Chapter 2 illustrated the importance of optimizing basic injector parameters and the resulting impact on the brightness produced. The approach to emittance optimization presented is universal and applicable to any injector, where the goal is to maximize brightness. By decomposing the emittances and understanding individual emittance components at play, while making even small changes to bunch, the emittance can be lowered considerably, thereby enhancing brightness in a meaningful way.

Chapter 3 focused on the utility of an in-situ emittance measurement that is based on the usefulness of cathode retraction or, in other words, Pierce lensing. As injector design continues to improve, the intrinsic emittance contribution has become more important because it represents the ultimate limit to attainable brightness. As discussed in Chapter 2, space charge emittance and rf emittance are actively being minimized wherever possible which has spurred the design of specialized cathodes to minimize the remaining, intrinsic emittance, component. Such new cathodes (based on novel chemistry formulations) are being actively developed or investigated and, at this moment, are not as robust as previous generations (mostly metals). Therefore, ensuring the new generation photocathodes perform as desired over time is necessary to the continual operation of many user facilities, and simply for the sake of being able to characterize them well. Thus, having a fast, robust, and accurate way to characterize such new cathodes in terms of QE and MTE, is critical. In Chapter 3, a two-slit emittance measurement approach was proposed that focused on measuring the MTE of the cathode in situ. The approach ensures that the cathode is performing as expected without having to sacrifice large amounts of operational time. Cathode retraction proved incredibly useful to the goal of measuring the MTE and also identified a possible operational range where the defocusing of the injector is minimized at the cost of accelerating gradient on the cathode.

The emittance optimization proposed in Chapter 2 focused primarily on space charge and rf emittance contributions, Chapter 3 of this thesis focused on the remaining primary emittance source, intrinsic emittance. Together these chapters provide a comprehensive analysis of the primary emittance components and how to manage them in novel ways to advance the photoinjector technology further. Chapter 4 presented and demonstrated a novel multi-mode cavity design with a wide variety of possible applications. The specific design showcased how positive net energy bunching could be applied to an electron beam. Bunching the beam improves the brightness of a bunch by compressing the bunch longitudinally thus increasing the current and brightness. This is a well-known and commonly used technique in many accelerators. Hower, the proposed cavity improves this technique by accelerating the bunch at the same time. This minimizes the energy lost by the bunch in the zero-crossing of the field where the bunch is decelerated for half of the time it spends in the cavity. By linearizing the leading edge of the rf field inside the cavity, the bunch is able to be compressed closer to the crest of the field while still having a linear energy chirp applied across it. However, this was only one specific use case for the multi-mode cavity. The design and verification presented in Chapter 4 can be applied to create multimode cavities with a variety of functions and modalities in many microwave technologies. In conclusion, this thesis has presented a detailed analysis of emittance control and measurement techniques, including a novel multi-mode cavity which can be used to further improve brightness.

## 5.1 Future Work

As for future work, the simulation work presented in Chapter 2 could be verified on single cell guns (including Argonne Cathode Teststand) as further verification and validation of our work. The two slit emittance measurement system proposed in Chapter 3 could be implemented on the Low Emittance Injector gun in the future. This would allow for verification of the presented simulation results and for implementing a practical means for in situ emittance measurements.

The multimode cavity presented in Chapter 4 has a few different options for future work. First, a test beam line system where the efficiency of a multimode system is compared against a system using two separate cavities has been proposed and the necessary cavities for comparison have been fabricated. An injector capable of producing 15 keV initial electron beam would be needed to make these measurements possible. This would also create the opportunity for running GPT simulations and comparing them to experiments done using multimode and single mode cavities.

# BIBLIOGRAPHY


[1] Thomas Lucas, Paolo Craievich, and Sven Reiche. “A Discussion of Key Concepts for the Next Generation of High Brightness Injectors”. In: *Proceedings of the 31st International Linear Accelerator Conference* LINAC2022 (2022). In collab. with McIntosh Peter (Ed.) et al. Artwork Size: 6 pages, 0.902 MB ISBN: 9783954502158 Medium: PDF Publisher: JACoW Publishing, Geneva, Switzerland, 6 pages, 0.902 MB. URL: https://jacow.org/linac2022/doi/JACoW-LINAC2022-TU1PA01.html (visited on 09/26/2024).

[2] J.D. Lawson. *The Physics of Charged-particle Beams*. International series of monographs on physics. Clarendon Press, 1988.

[3] Kwang-Je Kim. “Rf and space-charge effects in laser-driven rf electron guns”. In: *Nuclear Instruments and Methods in Physics Research Section A: Accelerators, Spectrometers, Detectors and Associated Equipment* 275.2 (1989), pp. 201–218. URL: https://www.sciencedirect.com/science/article/pii/0168900289906888.

[4] M. J. Rhee. “Refined definition of the beam brightness”. In: *Physics of Fluids B: Plasma Physics* 4.6 (June 1, 1992), pp. 1674–1676. URL: https://pubs.aip.org/pfb/article/4/6/1674/941549/Refined-definition-of-the-beam-brightnessBrief (visited on 09/26/2024).

[5] Claudio Pellegrini and Joachim Stöhr. “X-ray free-electron lasers—principles, properties and applications”. In: *Nuclear Instruments and Methods in Physics Research Section A: Accelerators, Spectrometers, Detectors and Associated Equipment* 500.1 (Mar. 2003), pp. 33–40. URL: https://linkinghub.elsevier.com/retrieve/pii/S0168900203007393 (visited on 08/12/2024).

[6] Patrick G. O’Shea and Henry P. Freund. “Free-Electron Lasers: Status and Applications”. In: *Science* 292.5523 (June 8, 2001), pp. 1853–1858. URL: https://www.science.org/doi/10.1126/science.1055718 (visited on 08/12/2024).

[7] Sébastien Boutet, Petra Fromme, and Mark S. Hunter, eds. *X-ray Free Electron Lasers: A Revolution in Structural Biology*. Cham: Springer International Publishing, 2018. URL: http://link.springer.com/10.1007/978-3-030-00551-1 (visited on 08/12/2024).

[8] Dalong Qi et al. “Compressed Ultrafast Electron Diffraction Imaging Through Electronic Encoding”. In: *Physical Review Applied* 10.5 (Nov. 28, 2018), p. 054061. URL: https://link.aps.org/doi/10.1103/PhysRevApplied.10.054061 (visited on 08/12/2024).

[9] D. Filippetto et al. “Ultrafast electron diffraction: Visualizing dynamic states of matter”. In: *Reviews of Modern Physics* 94.4 (Dec. 6, 2022), p. 045004. URL: https://link.aps.org/doi/10.1103/RevModPhys.94.045004 (visited on 08/12/2024).

[10] Kyu-Ha Jang et al. “Ultrafast Electron Diffraction Technology for Exploring Dynamics of Molecules”. In: *Journal of the Korean Physical Society* 73.4 (Aug. 2018), pp. 466–478.

URL: http://link.springer.com/10.3938/jkps.73.466 (visited on 08/12/2024).

[11] F. Albert et al. “Characterization and applications of a tunable, laser-based, MeV-class Compton-scattering Gamma -ray source”. In: *Physical Review Special Topics - Accelerators and Beams* 13.7 (July 27, 2010), p. 070704. URL: https://link.aps.org/doi/10.1103/PhysRevSTAB.13.070704 (visited on 08/12/2024).

[12] Guang-Peng An et al. “High energy and high brightness laser compton backscattering gamma-ray source at IHEP”. in: *Matter and Radiation at Extremes* 3.4 (2018), pp. 219–226. URL: https://doi.org/10.1016/j.mre.2018.01.005.

[13] A P Gregory. *Q-factor measurement by using a Vector Network Analyser*. National Physical Laboratory, Jan. 4, 2022. URL: http://eprintspublications.npl.co.uk/id/eprint/9304 (visited on 04/11/2024).

[14] Y.M. Nosochkov et al. “Electron Transport for the LCLS-II-HE Low Emittance Injector”. In: *Proc. IPAC’22* (Bangkok, Thailand). International Particle Accelerator Conference 13. JACoW Publishing, Geneva, Switzerland, July 2022, TUPOPT046, pp. 1103–1106. URL: https://jacow.org/ipac2022/papers/tupopt046.pdf.

[15] J. B. Rosenzweig et al. “Next generation high brightness electron beams from ultrahigh field cryogenic rf photocathode sources”. In: *Phys. Rev. Accel. Beams* 22 (2 2019), p. 023403. URL: https://link.aps.org/doi/10.1103/PhysRevAccelBeams.22.023403.

[16] Eduard Prat et al. “Emittance measurements and minimization at the SwissFEL Injector Test Facility”. In: *Phys. Rev. ST Accel. Beams* 17 (10 2014), p. 104401. URL: https://link.aps.org/doi/10.1103/PhysRevSTAB.17.104401.

[17] Feng Zhou et al. “Impact of the spatial laser distribution on photocathode gun operation”. In: *Phys. Rev. ST Accel. Beams* 15 (9 2012), p. 090701. URL: https://link.aps.org/doi/10.1103/PhysRevSTAB.15.090701.

[18] H.J. Qian, D. Filippetto, and F. Sannibale. “S-Band Photoinjector Investigations by Multi-objective Genetic Optimizer”. In: *Proc. of International Particle Accelerator Conference (IPAC’16), Busan, Korea, May 8-13, 2016* (Busan, Korea). International Particle Accelerator Conference 7. doi:10.18429/JACoW-IPAC2016-THPOW020. Geneva, Switzerland: JACoW, 2016, pp. 3979–3982. URL: http://jacow.org/ipac2016/papers/thpow020.pdf.

[19] Colwyn Gulliford et al. “Demonstration of low emittance in the Cornell energy recovery linac injector prototype”. In: *Phys. Rev. ST Accel. Beams* 16 (7 2013), p. 073401. URL: https://link.aps.org/doi/10.1103/PhysRevSTAB.16.073401.

[20] C. F. Papadopoulos et al. “RF Injector Beam Dynamics Optimization for LCLS-II”. in: *Proc. 5th International Particle Accelerator Conference (IPAC’14), Dresden, Germany, June 15-20, 2014* (Dresden, Germany). International Particle Accelerator Conference 5.

https://doi.org/10.18429/JACoW-IPAC2014-WEPRO015. Geneva, Switzerland: JACoW, 2014, pp. 1974–1976. URL: http://jacow.org/ipac2014/papers/wepro015.pdf.

[21] N. Neveu et al. "Parallel general purpose multiobjective optimization framework with application to electron beam dynamics". In: *Phys. Rev. Accel. Beams* 22 (5 2019), p. 054602. URL: https://link.aps.org/doi/10.1103/PhysRevAccelBeams.22.054602.

[22] Nicole Neveu et al. "Comparison of multiobjective optimization methods for the LCLS-II photoinjector". In: *Computer Physics Communications* 283 (2023), p. 108566. URL: https://www.sciencedirect.com/science/article/pii/S0010465522002855.

[23] M. Krasilnikov et al. "Experimentally minimized beam emittance from an $L$-band photoinjector". In: *Phys. Rev. ST Accel. Beams* 15 (10 2012), p. 100701. URL: https://link.aps.org/doi/10.1103/PhysRevSTAB.15.100701.

[24] Colwyn Gulliford et al. "Demonstration of cathode emittance dominated high bunch charge beams in a DC gun-based photoinjector". In: *Applied Physics Letters* 106.9 (2015), p. 094101. URL: https://doi.org/10.1063/1.4913678.

[25] D. Filippetto et al. "Maximum current density and beam brightness achievable by laser-driven electron sources". In: *Phys. Rev. ST Accel. Beams* 17 (2 2014), p. 024201. URL: https://link.aps.org/doi/10.1103/PhysRevSTAB.17.024201.

[26] Soichiro Tsujino. "On the brightness, transverse emittance, and transverse coherence of field emission beam". In: *Journal of Vacuum Science and Technology B* 40.3 (2022), p. 030801. URL: https://doi.org/10.1116/6.0001776.

[27] Ivan V. Bazarov, Bruce M. Dunham, and Charles K. Sinclair. "Maximum Achievable Beam Brightness from Photoinjectors". In: *Phys. Rev. Lett.* 102 (10 2009), p. 104801. URL: https://link.aps.org/doi/10.1103/PhysRevLett.102.104801.

[28] J. Wu et al. "Emittance Preservation for LCLS-II-HE Project". In: *Proc. 10th International Particle Accelerator Conference (IPAC'19)* (Melbourne, Australia). International Particle Accelerator Conference 10. https://doi.org/10.18429/JACoW-IPAC2019-WEPTS093. Geneva, Switzerland: JACoW Publishing, 2019, pp. 3333–3336. URL: http://jacow.org/ipac2019/papers/wepts093.pdf.

[29] Christopher M. Pierce et al. "Low intrinsic emittance in modern photoinjector brightness". In: *Phys. Rev. Accel. Beams* 23 (7 2020), p. 070101. URL: https://link.aps.org/doi/10.1103/PhysRevAccelBeams.23.070101.

[30] Ivan V. Bazarov and Charles K. Sinclair. "Multivariate optimization of a high brightness dc gun photoinjector". In: *Phys. Rev. ST Accel. Beams* 8 (3 2005), p. 034202. URL: https://link.aps.org/doi/10.1103/PhysRevSTAB.8.034202.

[31] Alicia Hofler et al. “Innovative applications of genetic algorithms to problems in accelerator physics”. In: *Phys. Rev. ST Accel. Beams* 16 (1 2013), p. 010101. URL: https://link.aps.org/doi/10.1103/PhysRevSTAB.16.010101.

[32] Jiahang Shao et al. “High power conditioning and benchmarking of planar nitrogen incorporated ultrananocrystalline diamond field emission electron source”. In: *Phys. Rev. Accel. Beams* 22 (12 2019), p. 123402. URL: https://link.aps.org/doi/10.1103/PhysRevAccelBeams.22.123402.

[33] CH Ho et al. *SRRC/ANL high current L-band single cell photocathode rf gun*. Tech. rep. SRRC, ANL, 1998. URL: https://www.osti.gov/biblio/10884.

[34] Mitchell E. Schneider et al. “Ampere-class bright field emission cathode operated at 100 MV/m”. In: *Phys. Rev. Accel. Beams* 24 (12 2021), p. 123401. URL: https://link.aps.org/doi/10.1103/PhysRevAccelBeams.24.123401.

[35] J Stohr. *Linac Coherent Light Source II (LCLS-II) Conceptual Design Report*. Tech. rep. SLAC-R-978 ,TRN: US1200028. SLAC, Nov. 2011. URL: https://www.osti.gov/biblio/1029479.

[36] A. D. Cahill et al. “High gradient experiments with $X$-band cryogenic copper accelerating cavities”. In: *Phys. Rev. Accel. Beams* 21 (10 2018), p. 102002. URL: https://link.aps.org/doi/10.1103/PhysRevAccelBeams.21.102002.

[37] S.B. van der Geer and M.J. de Loos. *General Particle Tracer*. Pulsar Physics. URL: https://wiki.jlab.org/ciswiki/images/4/42/UserManual.pdf.

[38] Siddharth Karkare et al. “Ultracold Electrons via Near-Threshold Photoemission from Single-Crystal Cu(100)”. In: *Phys. Rev. Lett.* 125 (5 2020), p. 054801. URL: https://link.aps.org/doi/10.1103/PhysRevLett.125.054801.

[39] Luca Cultrera et al. “Thermal emittance and response time of a cesium antimonide photocathode”. In: *Applied Physics Letters* 99.15 (2011), p. 152110. URL: https://doi.org/10.1063/1.3652758.

[40] Benjamin Sims and Sergey V. Baryshev. “Emittance mapping in rf guns”. In: (Nov. 13, 2023). URL: https://link.aps.org/doi/10.1103/PhysRevAccelBeams.26.113402 (visited on 06/18/2024).

[41] Ivan V. Bazarov et al. “Benchmarking of 3D space charge codes using direct phase space measurements from photoemission high voltage dc gun”. In: *Physical Review Special Topics - Accelerators and Beams* (Oct. 30, 2008). URL: https://link.aps.org/doi/10.1103/PhysRevSTAB.11.100703 (visited on 01/29/2024).

[42] Lei Yu et al. “Systematic analysis of a compact setup to measure the photoemitted electron

beam transverse momentum and emittance". In: *Review of Scientific Instruments* (). URL: https://doi.org/10.1063/5.0013122.

[43] Shuai Ma. "Transverse Emittance Measurements and Optimization for a Superconducting RF Photo Injector". PhD thesis. U. Hamburg, Dept. Phys., 2022.

[44] S. G. Anderson et al. "Space-charge effects in high brightness electron beam emittance measurements". In: *Physical Review Special Topics - Accelerators and Beams* (Jan. 10, 2002). URL: https://link.aps.org/doi/10.1103/PhysRevSTAB.5.014201 (visited on 04/09/2024).

[45] Max Hachmann. "Transverse emittance measurement at REGAE via a solenoid scan". PhD thesis. Hamburg: Universität Hamburg, 2012. 110 pp. URL: https://pure.mpg.de/pubman/faces/ViewItemFullPage.jsp?itemId=item_2627923_1.

[46] Igor Pinayev et al. "Solenoid: universal tool for measuring beam parameters". In: *arXiv e-prints* (2019).

[47] Lianmin Zheng et al. "Overestimation of thermal emittance in solenoid scans due to coupled transverse motion". In: *Physical Review Accelerators and Beams* (Dec. 26, 2018). (Visited on 02/29/2024).

[48] Lianmin Zheng, Yingchao Du, and Pengwei Huang. "Eliminating uncertainty of thermal emittance measurement in solenoid scans due to rf and solenoid fields overlap". In: *Nuclear Instruments and Methods in Physics Research Section A: Accelerators, Spectrometers, Detectors and Associated Equipment* (Feb. 2022). URL: https://linkinghub.elsevier.com/retrieve/pii/S0168900221010378 (visited on 03/04/2024).

[49] P. Lu et al. "Transverse emittance measurement by slit-scan method for an SRF photo injector". In: *Proceedings of FEL2013* (2013), pp. 322–324. URL: https://accelconf.web.cern.ch/fel2013/papers/tupso44.pdf.

[50] V. Yakimenko et al. "Electron beam phase-space measurement using a high-precision tomography technique". In: *Physical Review Special Topics - Accelerators and Beams* (Dec. 30, 2003). URL: https://link.aps.org/doi/10.1103/PhysRevSTAB.6.122801 (visited on 07/29/2024).

[51] D. Stratakis et al. "Tomographic phase-space mapping of intense particle beams using solenoids". In: *Physics of Plasmas* 12 (Dec. 1, 2007). URL: https://pubs.aip.org/pop/article/14/12/120703/901960/Tomographic-phase-space-mapping-of-intense.

[52] Dao Xiang et al. "Transverse phase space tomography using a solenoid applied to a thermal emittance measurement". In: *Physical Review Special Topics - Accelerators and Beams* 2 (Feb. 18, 2009). URL: https://link.aps.org/doi/10.1103/PhysRevSTAB.12.022801 (visited on 09/03/2024).

[53] S. Ma et al. "The application of encoder–decoder neural networks in high accuracy and efficiency slit-scan emittance measurements". In: *Nuclear Instruments and Methods in Physics Research Section A: Accelerators, Spectrometers, Detectors and Associated Equipment* (May 2023). URL: https://linkinghub.elsevier.com/retrieve/pii/S0168900223001158 (visited on 04/09/2024).

[54] W. B. Herrmannsfeldt. "Low emittance thermionic electron guns". In: *AIP Conf. Proc.* 184 (1989). Ed. by M. Month and M. Dienes, pp. 1532–1542.

[55] Minwen Wang et al. "Design and Test Results of a Double-Slit Emittance Meter at XiPAF". in: *Proceedings of the 7\textsuperscript{th} Int. Beam Instrumentation Conf.* IBIC2018 (2019). In collab. with Schaa RW (Ed.) Volker. URL: http://jacow.org/ibic2018/doi/JACoW-IBIC2018-WEPC09.html (visited on 01/29/2024).

[56] Min Zhang. "Emittance formula for slits and pepper pot measurement". In: *FNAL* (). URL: https://www.osti.gov/biblio/395453.

[57] John Lewellen et al. "An Electrostatic Fixed-Slit Emittance Measurement System". In: *Proceedings of the 9th Int. Particle Accelerator Conf.* IPAC2018 (2018). In collab. with Satogata Todd (Ed.) and Schaa RW (Ed.) Volker. URL: http://jacow.org/ipac2018/doi/JACoW-IPAC2018-WEPAL045.html (visited on 04/07/2023).

[58] T. Ludwig et al. "Quantization error of slit-grid emittance measurement devices". In: *Review of Scientific Instruments* 65.4 (1994), pp. 1462–1464. URL: https://doi.org/10.1063/1.1144946.

[59] J.H. Billen and L.M. Young. *Poisson Superfish*. Version 7.17. LA-UR-96-1834. Jan. 13, 2006.

[60] Dr. S.B. van der Geer. *GPT*. version 3.43. 2020. URL: https://www.pulsar.nl/gpt/.

[61] Taro Konomi et al. "Design and Tests of a Cathode Stalk for the LCLS-II-HE Low Emittance Injector SRF Gun". In: (2023). In collab. with Saito Kenji (Ed.) et al. Artwork Size: 4 pages, 1.023 MB ISBN: 9783954502349 Medium: application/pdf Publisher: JACoW Publishing, Geneva, Switzerland, 4 pages, 1.023 MB. URL: https://jacow.org/srf2023/doi/JACoW-SRF2023-TUPTB069.html (visited on 01/13/2025).

[62] Gongxiaohui Chen et al. "Demonstration of nitrogen-incorporated ultrananocrystalline diamond photocathodes in a RF gun environment". In: *Applied Physics Letters* 117.17 (Oct. 26, 2020), p. 171903. URL: https://pubs.aip.org/apl/article/117/17/171903/39101/Demonstration-of-nitrogen-incorporated (visited on 01/15/2025).

[63] Sergey V. Baryshev et al. "Cryogenic operation of planar ultrananocrystalline diamond field emission source in SRF injector". In: *Applied Physics Letters* 118.5 (2021), p. 053505. URL: https://doi.org/10.1063/5.0013172.

[64] Jiaqi Qiu et al. “Nanodiamond Thin Film Field Emitter Cartridge for Miniature High-Gradient Radio Frequency $X$ -Band Electron Injector”. In: *IEEE Transactions on Electron Devices* (2018).

[65] David J Griffiths. *Introduction to electrodynamics*. Pearson, 2013.

[66] Srivatsan Chakram et al. “Seamless High-$Q$ Microwave Cavities for Multimode Circuit Quantum Electrodynamics”. In: *Phys. Rev. Lett.* (2021). URL: https://link.aps.org/doi/10.1103/PhysRevLett.127.107701.

[67] Alicia J Kollár et al. “An adjustable-length cavity and Bose–Einstein condensate apparatus for multimode cavity QED”. in: *New Journal of Physics* 4 (2015). URL: https://dx.doi.org/10.1088/1367-2630/17/4/043012.

[68] Neereja M. Sundaresan et al. “Beyond Strong Coupling in a Multimode Cavity”. In: *Physical Review X* 5.2 (June 29, 2015). Publisher: American Physical Society, p. 021035. URL: https://link.aps.org/doi/10.1103/PhysRevX.5.021035 (visited on 12/12/2024).

[69] Samuel Stein et al. *Multi-mode Cavity Centric Architectures for Quantum Simulation*. Sept. 27, 2023. URL: http://arxiv.org/abs/2309.15994 (visited on 12/12/2024).

[70] Geoffrey D. Reeves et al. “The Beam Plasma Interactions Experiment: An Active Experiment Using Pulsed Electron Beams”. In: *Frontiers in Astronomy and Space Sciences* 7 (2020). URL: https://www.frontiersin.org/journals/astronomy-and-space-sciences/articles/10.3389/fspas.2020.00023.

[71] Eva Sicking. “Updated Baseline for a staged Compact Linear Collider”. In: *CERN Yellow Reports* (Aug. 29, 2016). URL: https://e-publishing.cern.ch/index.php/CYR/article/view/335 (visited on 09/27/2024).

[72] P. Abbamonte et al. “New Science Opportunities Enabled by LCLS-II X-Ray Lasers”. In: (June 2015). URL: https://www.osti.gov/biblio/1630267.

[73] D. H. Dowell et al. “A two-Frequency RF Photocathode Gun”. In: *Nuclear Instruments and Methods in Physics Research Section A: Accelerators, Spectrometers, Detectors and Associated Equipment* 1 (2004). URL: https://www.sciencedirect.com/science/article/pii/S0168900204007338.

[74] L. Serafini, R. Rivolta, and C. Pagani. “Neutralization of the emittance blowup induced by RF time dependent forces in RF guns”. In: *Nucl. Instrum. Meth. A* 318 (1992), pp. 301–307.

[75] John W. Lewellen. “Higher-order mode rf guns”. In: *Physical Review Special Topics - Accelerators and Beams* 4 (Apr. 30, 2001). URL: https://link.aps.org/doi/10.1103/PhysRevSTAB.4.040101 (visited on 02/05/2024).

[76] H. Gong et al. "Design of a dual-mode transverse deflecting structure using neural network and multiobjective algorithms". In: *Physical Review Accelerators and Beams* (Apr. 15, 2024). URL: https://link.aps.org/doi/10.1103/PhysRevAccelBeams.27.042001 (visited on 09/27/2024).

[77] A. Romanenko et al. "Three-Dimensional Superconducting Resonators at T < 20 mK with Photon Lifetimes up to tau = 2s". In: *Phys. Rev. Appl.* (3 2020). URL: https://link.aps.org/doi/10.1103/PhysRevApplied.13.034032.

[78] Changqing Wang et al. "High-efficiency microwave-optical quantum transduction based on a cavity electro-optic superconducting system with long coherence time". In: *npj Quantum Information* (Dec. 21, 2022). URL: https://www.nature.com/articles/s41534-022-00664-7 (visited on 09/16/2024).

[79] R. Akre et al. "Commissioning the Linac Coherent Light Source injector". In: *Physical Review Special Topics - Accelerators and Beams* 3 (Mar. 12, 2008). URL: https://link.aps.org/doi/10.1103/PhysRevSTAB.11.030703 (visited on 09/24/2024).

[80] Mamdouh Nasr and Sami Tantawi. "The Design and Construction of a Novel Dual-Mode Dual-Frequency Linac Design". In: *Proceedings of the 9th Int. Particle Accelerator Conf.* IPAC2018 (2018). In collab. with Satogata Todd (Ed.) and Schaa RW (Ed.) Volker. URL: http://jacow.org/ipac2018/doi/JACoW-IPAC2018-THPMK048.html (visited on 01/30/2024).

[81] Evgenya Simakov et al. "Update on the Status of C-Band Research and Facilities at LANL". in: *Proceedings of the 5th North American Particle Accelerator Conference* NAPAC2022 (2022). In collab. with Biedron Sandra (Ed.) et al. URL: https://jacow.org/napac2022/doi/JACoW-NAPAC2022-THYD3.html (visited on 09/27/2024).

[82] Mitchell Schneider et al. "High gradient off-axis coupled C-band Cu and CuAg accelerating structures". In: *Applied Physics Letters* 121.25 (2022), p. 254101. URL: https://doi.org/10.1063/5.0132706.

[83] M Puglisi. *CONVENTIONAL RF CAVITY DESIGN*. URL: https://cds.cern.ch/record/1702625/files/p156.pdf.

[84] E Haebel. *COUPLERS FOR CAVITIES*. URL: https://cds.cern.ch/record/308016/files/p231.pdf.

[85] Benjamin Sims and Sergey V. Baryshev. *Multi-Mode Radiofrequency Cavity*. Patent pending. 2024.

[86] D. Longuevergne et al. "An innovative tuning system for superconducting accelerating cavities". In: *Nuclear Instruments and Methods in Physics Research Section A: Accelerators, Spectrometers, Detectors and Associated Equipment* (June 2014). URL: https://linkinghub.

elsevier.com/retrieve/pii/S0168900214002277 (visited on 01/29/2024).

[87] V. Veshcherevich et al. “RF measurements and control of higher order modes in accelerating cavities”. In: *Proceedings Particle Accelerator Conference*. Dallas, TX, USA: IEEE, 1995. URL: http://ieeexplore.ieee.org/document/505325/ (visited on 01/29/2024).

[88] J. C. Slater. “Microwave Electronics”. In: *Rev. Mod. Phys.* (1946). URL: https://link.aps.org/doi/10.1103/RevModPhys.18.441.

[89] Dennis Thomas Palmer. “The Next Generation Photoinjector”. PhD thesis. Stanford University, Sept. 12, 2005, SLAC–R–500, 878424. URL: https://www.slac.stanford.edu/pubs/slacreports/reports16/slac-r-500.pdf (visited on 09/30/2024).

[90] Cederik Meekes and Ferdi van de Wetering. “Characterizing a Microwave Cavity using the Bead-Pull Method”. Eindhoven University of technology, 2017.

[91] Rolf Wegner et al. “Bead-Pull Measurement Method and Tuning of a Prototype CLIC Crab Cavity”. In: *27th Linear Accelerator Conference* (2014), MOPP035. URL: https://cds.cern.ch/record/2025951.

[92] Triveni Rao and David H. Dowell. *An Engineering Guide To Photoinjectors*. 2014. URL: https://arxiv.org/abs/1403.7539.

[93] D.K. Callebaut and M.C. Vanwormhoudt. “Field measurements in resonant cavities”. In: *Physica* 4 (Apr. 1960). URL: https://linkinghub.elsevier.com/retrieve/pii/0031891460900197 (visited on 01/29/2024).

[94] David M. Pozar. *Microwave engineering*. Fourth Edition. Hoboken, NJ: John Wiley and Sons, Inc, 2012. 732 pp.

[95] J.N. Corlett and J.M. Byrd. “Measurement and computation of the higher order modes of the ALS 500 MHz accelerating cavities”. In: *Proceedings of International Conference on Particle Accelerators*. Washington, DC, USA: IEEE, 1993. URL: http://ieeexplore.ieee.org/document/309666/ (visited on 01/29/2024).

[96] B. Sims et al. “Multi-mode cavity design and characterization”. English. In: *Proc. 15th International Particle Accelerator Conference* (Nashville, TN). IPAC’24 - 15th International Particle Accelerator Conference 15. JACoW Publishing, Geneva, Switzerland, 2024. URL: https://indico.jacow.org/event/63/contributions/3226.

[97] D. Kajfez. “Reflection-type Q factor measurement of transmission-type cavities”. In: *2000 Asia-Pacific Microwave Conference. Proceedings (Cat. No.00TH8522)*. 2000 Asia-Pacific Microwave Conference. Sydney, NSW, Australia: IEEE, 2000. URL: http://ieeexplore.ieee.org/document/925855/ (visited on 04/11/2024).

[98] E. L. Ginzton. *Microwave measurements*. New York: McGraw-Hill, 1957.